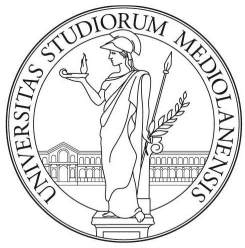

UNIVERSITÀ DEGLI STUDI DI MILANO
FACOLTÀ DI SCIENZE MATEMATICHE, FISICHE E NATURALI
DOTTORATO DI RICERCA IN
FISICA, ASTROFISICA E FISICA APPLICATA

A NOVEL SOURCE OF ENTANGLED STATES FOR QUANTUM INFORMATION APPLICATIONS

Settore Scientifico disciplinare FIS/03

Coordinatore: Prof. Marco Bersanelli

Tutore: Dr. Simone Cialdi

Tesi di Dottorato di:

Davide Brivio

Ciclo XXIV

Anno Accademico 2010 - 2011

a Giada

Rebecca e Michela

Abstract

Photonic entanglement sources are nowadays of central interest in the scientific landscape for their demonstrated applications in quantum information, computation and communication. Required features for a real implementation are obviously high brigthness and purity, but also a precise control of decoherence processes during propagation and the use of many degrees of freedom to enhance the amount of information carried.

We developed a new photonic entangled source based on parametric down-conversion within two type-I crystals in a non collinear configuration. A first peculiarity of such source is the very broad angular and spectral distribution exploited. In this way we obtained high brightness even using low pump power. A second peculiarity is the coupling of the source with a Spatial Light Modulator (SLM) allowing the compensation of intrinsic phase term which naturally reduces the state purity till about 0.5. Coupling 10 mrad on both channel, we obtained a purity of about 0.97 with a spectrum of 10 nm, and a purity around 0.90 with more than 60 nm.

Starting from such purified source we also realized multi-qubit cluster states exploiting the angular degree of freedom (d.o.f.) of the photons. Here the SLM acts as a C-phase gate entangling polarization and momentum qubits. Furthermore we exploited signal-idler angular correlation to demonstrate the ghost imaging of a pure phase object and we realized a new cryptographic protocol based on non-local phase objects superposition.

Our source has also paved the way in simulating system-environment interaction since the SLM allows precise decoherence control. We observed different dynamics of the system entanglement (polarization d.o.f.) modulating the environment spectrum (angular distribution). Then studying the trace distance evolution we demonstrated initial system-environment correlation.

Contents

Introduction

The behavior of nature is amazing and often the deep understanding of a phenomenon is a real challenge for human brain. That's the case of two particles or photons, correlated by an interaction happened somewhere in space and time and then spatially separated; they surprisingly remain linked each other, in a way that operating on one of them one instantly influences the twin. In other words we are dealing with particles or photons that the physicist call *entangled*.

In the last century quantum entanglement has been one of the leading actor on the stage of worldwide scientific research. It was initially introduced in 1935 by Einstein, Podolsky and Rosen (EPR) [1] to show the paradox that a theory as quantum mechanics would allow and then named "entanglement"by E. Schrödinger [2]. About thirty years later J. S. Bell found a way to test the EPR paradox [3], but only in 1972 S. J. Freedman et al. gave the first experimental measure of Bell's inequality [4]. A. Aspect's experiments confirmed the result in favor of quantum mechanics [5].

Besides these fundamental studies it has been found that entanglement is a key resource for quantum information and communication processes [6]. From here the interest in developing efficient sources. Freedman and Aspect's works used two-photon cascades in atoms as entanglement source. Starting from the last decades more efficient photonic sources based on spontaneous parametric down conversion (SPDC) in non-linear crystals started to be intensively used [7, 8], and, after the original experimental realization of energy-time entanglement [9], polarization entanglement in a single type-II crystal [10] and in two type-I crystals [11] has been realized. Nowadays many sources of multiqubit entanglement have been developed too, both using multiphoton [12] or exploiting many degrees of freedom of the two photons, such as spatial momentum [13] and orbital angular momentum [14]. For these reasons SPDC recently became the objective of many studies, *e.g.* about spectral and angular properties [15], spatiotemporal structure [16] or polarization [17]. Also some quantum information applications have been realized such as cluster states for quantum computation [18], dense coding [19], entanglement swapping, quantum teleportation [20] and the possibility of information transferring from one degree to an other has been demonstrated [21]. On the other hand the research about entanglement dynamics

in open system is the object of intense studies in the scientific community. Many theoretical models are actually present in the literature but very few experimental verification has been realized [22]. Recently the exploration of different degrees of freedom of the photons opens the possibility of simulating system-environment interactions [23, 24].

During my PhD I have realized a photonic entanglement source based on Spontaneous Parametric Down Conversion (SPDC) within two thin crystals. The novelty of my source is twofold. On the one hand the use of large angular and spectral distribution of the SPDC cone. This allows to obtain high brightness using low pump power and introduces intrinsic decoherence effects [25] one must compensate. On the other hand the coupling of the photon source with a Spatial Light Modulator allows to modulate at will the phase profile of the entangled beams. The use and the control of the angular phase distributions allow new studies about the SPDC process and pave the way for several application in quantum information.

In this manuscript I will describe our entanglement source theoretically and experimentally and finally I will describe some quantum information applications we have realized by using the SLM. In the first part we will study theoretically and experimentally the features of our source; the SLM is used both to compensate the intrinsic phase terms which reduce the purity of the state [26], both to enlight some properties of the source. In the second part we will present some quantum information applications we have realized. First of all I will describe the realizations of multiqubit entanglement exploiting the polarization and the linear momentum degrees of freedom of the photons and the SLM which acts as a phase gate [27]. Then I will describe the realization of ghost imaging and the superposition of different phase objects acting non-locally on the two channels. Phase objects are introduced arbitrarily by using the SLM. We demonstrate a proof of principle of a new cryptographic protocol based on the switch from entanglement to mixture by using proper pairs of phase objects [28]. Then we exploit the linear momentum degrees of freedom such as an environment bath in which the system (polarization degree of freedom) live, I will present the realization of the dynamics of an open-system in the presence of different environment [29]. With a similar setup we study initial system-environment correlation by means of the trace distance following the proposal of A. Smirne [30]. In these two works the SLM is used to impose linear phase shift in order to simulate different type of dynamics.

Part I

Entanglement source

Chapter 1

Quantum Information elements

In this first chapter we will give some few elements of quantum information useful in the reading of the manuscript. In the first section we will describe briefly what is a qubit and we introduce the concept of entanglement. Then in sec. 1.2 we will explain how to do quantum information using quantum optics. Subsequently in sec. 1.3 we will see how to measure the amount of polarization entanglement in our experimental situation and in sec. 1.4 we will treat the quantum tomographic reconstruction of the density matrix of two-qubit state in polarization in a general case. Finally in sec. 1.5 we will explain the CHSH form for the Bell's parameter measurement. This parameter has historically played a crucial role, in favor of the quantum mechanics, in the choise of the correct theoretical description of reality.

1.1 Qubit and Entanglement

The *Bit* (a contraction of Binary Digit) is the basic unit of information in classical telecommunication and computing. The logical bit values are 0 and 1 and could be encoded in a physical quantity such as two distinct voltage or current levels, two distinct levels of light intensity or directions of magnetization or polarization, etc. A string of n bits represents, in binary, a single number between 0 and 2^{n-1}.

In quantum information the basic element is the *Qubit* (quantum bit) which is the quantum superposition of the two bit $|0\rangle$ and $|1\rangle$ [6]; *i.e.*

$$a\,|0\rangle + b\,|1\rangle,$$

where a and b are probability amplitudes and can in general be complex numbers. Measuring this qubit in the standard basis $\{|0\rangle, |1\rangle\}$, the probability of outcome $|0\rangle$ is $|a|^2$ and the probability of outcome $|1\rangle$ is $|b|^2$. For

the normalization it holds $|a|^2 + |b|^2 = 1$. If we write a string of two equal qubits with $a = b = \frac{1}{\sqrt{2}}$, as follow:

$$\frac{1}{\sqrt{2}}(|0\rangle + |1\rangle) \otimes \frac{1}{\sqrt{2}}(|0\rangle + |1\rangle) = \frac{1}{2}(|00\rangle + |01\rangle + |10\rangle + |11\rangle), \tag{1.1}$$

we notice that it represents a linear superposition in binary units of all the numbers between 0 and 3 (in decimal notation). Furthermore we observe that in such string the two qubit are independent (or separable), *i.e.* a measure performed on the first qubit does not influence the second one. For example, if we obtain $|0\rangle$ from the measure of the first qubit, then the second remain in the superposition $\frac{1}{\sqrt{2}}(|0\rangle + |1\rangle)$ and a measure performed on it in the standard basis gives half probability for the two outcomes $|0\rangle$ or $|1\rangle$.

Nevertheless the most important feature of quantum information is the existence of a particular superposition of two (or more) qubit which are not separable. It is the case of entangled states, *e.g.*

$$|\varphi\rangle = \frac{1}{\sqrt{2}}(|00\rangle + |11\rangle). \tag{1.2}$$

Such a state could not be written like in eq. (1.1) as the tensor product of two one-qubit states in any basis. This means that the two qubits are correlated since a measure performed on one of them (giving for example the outcome $|0\rangle$ with half probability) instantly influence the second qubit which collapse in the state $|0\rangle$. Quantum entanglement occurs when particles such as photons, electrons or molecules interact physically and then become separated; the type of interaction is such that each resulting member of a pair is properly described only by the same quantum mechanical description of the total system. If entangled, one object cannot be fully described without considering the other(s). They remain in a quantum superposition and share a single quantum state until a measurement is made. Entanglement is the special resource of quantum information; it allows the realization of many quantum protocols such as teleportation, dense coding and quantum cryptography [6]. The powerful of such protocols has been demonstrated and in the last decades a great effort has been done toward many physical implementations [18, 19, 20].

A tool for the representation of a quantum state is the density matrix. It is an Hermitian, positive-semidefinite matrix of trace one useful for describing and performing calculations with a mixed state, which is a statistical ensemble of several quantum states. If we consider a statistical ensamble with 50% the two-qubit state $|00\rangle$ and 50% the state $|11\rangle$, we cannot use the superposition representation but a density matrix of the form

$$\rho_{mix} = \frac{1}{2}|00\rangle\langle 00| + \frac{1}{2}|11\rangle\langle 11| = \frac{1}{2}\begin{pmatrix} 1 & 0 & 0 & 0 \\ 0 & 0 & 0 & 0 \\ 0 & 0 & 0 & 0 \\ 0 & 0 & 0 & 1 \end{pmatrix}, \tag{1.3}$$

in the base $\{|00\rangle, |01\rangle, |10\rangle, |11\rangle\}$. This is in contrast to a pure state, which is a quantum system that could be completely described by a single state vector like the two-qubit maximally entangled state $|\varphi\rangle$ in eq. (1.2). The density matrix representation of the pure state $|\varphi\rangle$ is

$$\rho_{ent} = |\varphi\rangle\langle\varphi| = \frac{1}{2}\begin{pmatrix} 1 & 0 & 0 & 1 \\ 0 & 0 & 0 & 0 \\ 0 & 0 & 0 & 0 \\ 1 & 0 & 0 & 1 \end{pmatrix}. \tag{1.4}$$

1.2 How to do quantum information with quantum optics

In classical communication with optical fibers light is the physical system used to transport an information, and a proper amplitude modulation is used to encode the bit 0 or 1.

In quantum optics a photon is a quantum system on which one can encode an information exploiting many different degrees of freedom. First of all, the polarization, *i.e.* the direction of oscillation of the electric field, is a two level system often used to encode the logical qubits $|0\rangle$ and $|1\rangle$ with the following correspondence:

$$|0\rangle \rightarrow |H\rangle, \quad and$$

$$|1\rangle \rightarrow |V\rangle;$$

where $|H\rangle$ and $|V\rangle$ represent horizontal and vertical polarization. In this notation we can define the superposition states $|\pm 45°\rangle = \frac{1}{\sqrt{2}}(|H\rangle \pm |V\rangle)$ and $|R/L\rangle = \frac{1}{\sqrt{2}}(|H\rangle \pm i|V\rangle)$.

Nonetheless the photons has many other degrees of freedom such as, for example, the linear momentum and the orbital angular momentum. In both these cases one can define an higher dimension alphabet (not binary) exploiting different propagation directions or different helical shapes of the wavefront [13, 14].

In the following we deal with polarization and linear momentum. The latter is often indicated with the propagation direction of the photon in the horizontal plane at a certain angle θ, (θ') from a reference direction. We will deal with entangled states of the following type:

$$|\psi\rangle = \int d\theta d\theta' k(\theta, \theta') \left[|H, \theta\rangle|H, \theta'\rangle + e^{i\Phi}|V, \theta\rangle|V, \theta'\rangle\right], \tag{1.5}$$

where $|P, \theta\rangle|P', \theta'\rangle$ indicates a photon pair of polarization P and P' propagating at angles θ and θ', $k(\theta, \theta')$ indicates the amplitude probability for the photon pairs. The integrals indicate the superposition of photonic states

with different linear momentum θ and θ' while the sum indicates the superposition of two polarization states of the pair. The relative phase Φ is usually a function of the interested parameters (here the angles). Often we will integrate also over the frequencies of the photons with a similar notation.

1.3 Quantification of polarization entanglement

We consider the density matrix of a state $\rho = |\psi\rangle\langle\psi|$ (with $|\psi\rangle$ defined in eq. (1.5). We obtain

$$\rho = \frac{1}{2}\begin{pmatrix} 1 & 0 & 0 & \varepsilon \\ 0 & 0 & 0 & 0 \\ 0 & 0 & 0 & 0 \\ \varepsilon^* & 0 & 0 & 1 \end{pmatrix}, \tag{1.6}$$

with

$$\varepsilon = \int d\theta d\theta' |k(\theta,\theta')|^2 e^{\imath\Phi(\theta,\theta')}, \tag{1.7}$$

and

$$\int d\theta d\theta' |k(\theta,\theta')|^2 = 1. \tag{1.8}$$

The maximally entangled state $\frac{1}{\sqrt{2}}(|HH\rangle + |VV\rangle)$ and the corresponding mixture have density matrices expressed in equations (1.4) and (1.3) in the polarization base $\{|HH\rangle, |HV\rangle, |VH\rangle, |VV\rangle\}$. For a general state ρ (obtained for example from the state in eq. (1.5)) we have

$$\rho = p \cdot \rho_{ent} + (1-p) \cdot \rho_{mix}, \tag{1.9}$$

and we define p as the state purity. It is a real number and $0 \leq p \leq 1$. This purity is thus the amount of entanglement actually hold in the total state ρ.

A quantity universally recognized as a good entanglement measure is the concurrence [31]. It is defined as

$$\mathcal{C}(\rho) = max\{0, \lambda_1 - \lambda_2 - \lambda_3 - \lambda_4\}, \tag{1.10}$$

where λ_i are the eigenvalues, in decreasing order, of the Hermitian matrix $R = \sqrt{\sqrt{\rho}\widetilde{\rho}\sqrt{\rho}}$, with $\widetilde{\rho} = (\sigma_y \otimes \sigma_y)\rho^*(\sigma_y \otimes \sigma_y)$, $\sigma_y = \begin{pmatrix} 0 & -\imath \\ \imath & 0 \end{pmatrix}$ and ρ^* is the complex conjugate of ρ. For the state defined in eq. (1.6) one can show that $\mathcal{C}(\rho) = |\varepsilon|$.

Consider $\langle\alpha,\beta|\rho|\alpha,\beta\rangle$ the projection of the total state on the polarization at angle α for the signal and β for the idler; then we can define the quantities $Max = \langle 45°, 45°|\rho|45°, 45°\rangle$ and $min = \langle 45°, 135°|\rho|45°, 135°\rangle$. It is possible to show that the relation between interferometric visibility and the coherences ε reads

$$Vis = \frac{Max - min}{Max + min} = \mathcal{R}[\varepsilon]. \tag{1.11}$$

When ε is real the visibility is a good measure of entanglement since $Vis = \mathcal{C}$ and furthermore it equals the purity p.

1.4 Two-qubit tomography

In order to obtain full information on a quantum system we need to estimate its density matrix. The tool we used for complete state characterization is the quantum state tomography [32, 33].

A density matrix must has the properties of normalization, Hermiticity, and positivity to represent a real physical state. Calling ρ a density matrix of a physical state the three properties reads respectively:

$$Tr[\rho] = 1; \quad \rho = \rho^{\dagger}; \quad \langle\psi|\rho|\psi\rangle \geq 0, \, \forall|\psi\rangle; \tag{1.12}$$

A density matrix for a two-qubit state is a 4×4 matrix. The first two properties limits to 15 the number of independent parameters. The normalization of the state requires an other parameter. Totally we need to estimate 16 parameters in order to reconstruct the density matrix of a two-qubit state. The quantum tomography of the state consists in brief in the measure of

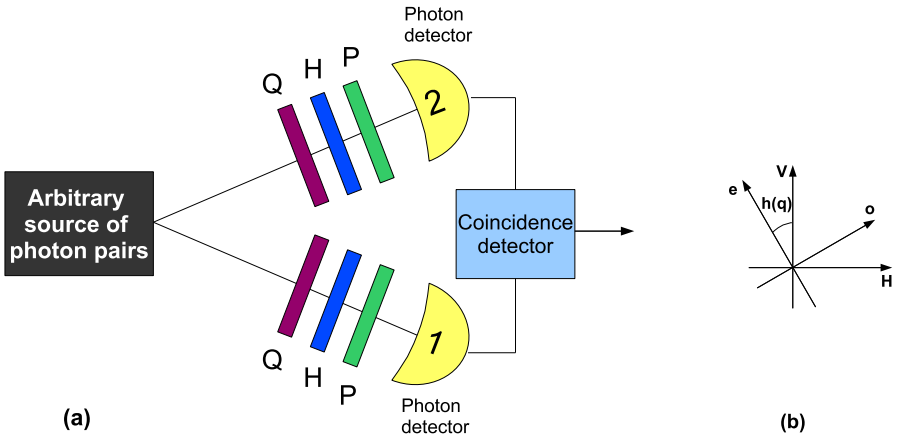

Figure 1.1: *(a) Experimental setup for the tomographic reconstruction of the total polarization density matrix of a two-qubit state. A pair of photon are generated by a source in an unknown polarization. A generic polarization projector is realized using a quarter-wave plate (Q), an half-wave plate (H) and a polarizer (P) on both channels. (b) Wave plate axes orientation, H and V are the horitzontal and vertical in the laboratory reference frame; o and e are the ordinary and extraordinary axes of the wave plates.*

sixteen two-qubit projectors from which we obtain the sixteen elements of

ν	*mode* 1	*mode* 2	h_1	q_1	h_2	q_2
1	$\|H\rangle$	$\|H\rangle$	45°	0	45°	0
2	$\|H\rangle$	$\|V\rangle$	45°	0	0	0
3	$\|V\rangle$	$\|V\rangle$	0	0	0	0
4	$\|V\rangle$	$\|H\rangle$	0	0	45°	0
5	$\|R\rangle$	$\|H\rangle$	22.5°	0	45°	0
6	$\|R\rangle$	$\|V\rangle$	22.5°	0	0	0
7	$\|D\rangle$	$\|V\rangle$	−22.5°	45°	0	0
8	$\|D\rangle$	$\|H\rangle$	−22.5°	45°	45°	0
9	$\|D\rangle$	$\|R\rangle$	−22.5°	45°	22.5°	0
10	$\|D\rangle$	$\|D\rangle$	−22.5°	45°	−22.5°	45°
11	$\|R\rangle$	$\|D\rangle$	22.5°	0	−22.5°	45°
12	$\|H\rangle$	$\|D\rangle$	45°	0	−22.5°	45°
13	$\|V\rangle$	$\|D\rangle$	0	0	−22.5°	45°
14	$\|V\rangle$	$\|L\rangle$	0	0	22.5°	90°
15	$\|H\rangle$	$\|L\rangle$	45°	0	22.5°	90°
16	$\|R\rangle$	$\|L\rangle$	22.5°	0	22.5°	90°

Table 1.1: *The sixteen two qutbit-projectors for the Tomographic reconstruction of the density matrix. The columns mode* $1, 2$ *report the projectors in the polarization basis, while the columns* $h_{1,2}$ *and* $q_{1,2}$ *report the angles of the wave plates required to obtain such projectors.*

the density matrix from the inversion. This is followed by a maximum likelihood reconstruction to obtain a density matrix ρ which is physical (*i*.e., which fulfill also the positivity properties expressed in eq. (1.12)). For a complete treatment see [33].

1.4.1 Two-qubit projectors

We consider two-qubit in polarization and we want to estimate the density matrix in the basis $\{|HH\rangle, |HV\rangle, |VH\rangle, |VV\rangle\}$. Defining $|D\rangle = \frac{1}{\sqrt{2}}(|H\rangle + |V\rangle)$, $|R\rangle = \frac{1}{\sqrt{2}}(|H\rangle - \imath|V\rangle)$ and $|L\rangle = \frac{1}{\sqrt{2}}(|H\rangle + \imath|V\rangle)$, the sixteen projectors are expressed in table (1.1). In the laboratory we implement these projectors by means of half-wave plates (H), quarter-wave plates (Q) and polarizers (P) (see fig. (1.1(a))). Considering h(q) the angle between the fast axis of the plates and the vertical of the laboratory (see figure (1.1(b))) and calling $|H\rangle = \begin{pmatrix} 1 \\ 0 \end{pmatrix}$ and $|V\rangle = \begin{pmatrix} 0 \\ 1 \end{pmatrix}$, the plates introduces the following trasformations on the polarizations:

$$U_{HWP}(h) = \begin{pmatrix} cos(2h) & sin(2h) \\ sin(2h) & -cos(2h) \end{pmatrix}, \text{ and} \tag{1.13}$$

$$U_{QWP}(q) = \frac{1}{\sqrt{2}} \begin{pmatrix} \imath + cos(2q) & sin(2q) \\ sin(2q) & \imath - cos(2q) \end{pmatrix}. \tag{1.14}$$

Thus the projection state for the measurement in one of the beams is given by

$$\begin{aligned} |\psi^{(1)}(h,q)\rangle &= U_{QWP}(q) \cdot U_{HWP}(h) \cdot \begin{pmatrix} 0 \\ 1 \end{pmatrix} = \\ &= a(h,q)|H\rangle + b(h,q)|V\rangle, \end{aligned} \tag{1.15}$$

with

$$a(h,q) = \frac{\imath}{\sqrt{2}}\{sin(2h) - \imath\, sin[2(h-q)]\} \tag{1.16}$$

$$b(h,q) = -\frac{\imath}{\sqrt{2}}\{cos(2h) + \imath\, cos[2(h-q)]\}. \tag{1.17}$$

The projection state for the two beams is given by

$$\begin{aligned} |\psi^{(2)}(h_1,q_1,h_2,q_2)\rangle &= |\psi^{(1)}(h_1,q_1)\rangle \otimes |\psi^{(1)}(h_2,q_2)\rangle = \\ &= a(h_1,q_1)\, a(h_2,q_2)\, |HH\rangle + \\ &+ a(h_1,q_1)\, b(h_2,q_2)\, |HV\rangle + \\ &+ b(h_1,q_1)\, a(h_2,q_2)\, |VH\rangle + \\ &+ b(h_1,q_1)\, b(h_2,q_2)\, |VV\rangle. \end{aligned} \tag{1.18}$$

Changing the angles $\nu = \{h_{1\nu}, q_{1\nu}, h_{2\nu}, q_{2\nu}\}$ one can project the two qubit state ρ on a generic polarization state $|\psi_\nu\rangle = |\psi^{(2)}(h_{1\nu}, q_{1\nu}, h_{2\nu}, q_{2\nu})\rangle$. Such projector is $|\psi_\nu\rangle\langle\psi_\nu|$ and the expected number of photons detected is

$$n_\nu = \mathcal{N}\langle\psi_\nu|\rho|\psi_\nu\rangle, \tag{1.19}$$

with $\mathcal{N}$ a parameter depending on photon flux and detection efficiency. As explained above we choose a set of 16 projectors (see table (1.1)) and we obtain the set $\{n_\nu\}$, with $\nu = 1, 2, ..., 16$ which uniquely determine the density matrix of the state from the inversion

$$\rho = \frac{1}{\mathcal{N}} \sum_{\nu=1}^{16} M_\nu n_\nu, \tag{1.20}$$

where M_ν are 16 matrices 4×4 allowing a compact form for the tomographic reconstruction. The complete list can be found in the appendix B of ref. [33]. Furthermore

$$\begin{aligned} \mathcal{N} &= \mathcal{N}\,[\,\langle HH|\rho|HH\rangle + \langle HV|\rho|HV\rangle + \\ &\quad + \langle VH|\rho|VH\rangle + \langle VV|\rho|VV\rangle\,] = \\ &= \sum_{\nu=1}^{4} n_\nu, \end{aligned} \tag{1.21}$$

thus

$$\rho = \frac{\sum_{\nu=1}^{16} M_\nu n_\nu}{\sum_{\nu=1}^{4} n_\nu}. \tag{1.22}$$

1.4.2 Maximum likelihood estimation

As mentioned above the reconstruction of density matrices by inversion can produce results that violate important basic properties such as positivity. To avoid this problem, the maximum likelihood estimation of density matrices may be employed. The procedure goes as follow:

- Define a general formula for a physical density matrix with 16 parameters $\rho_p(\{t_\nu\})$, with $\nu = 1, 2, ..., 16$;
- Introduce a "likelihood function" which quantifies how good the density matrix $\rho_p(\{t_\nu\})$ is in relation to the experimental data $\{n_\nu\}$. We will denote this function as $\mathcal{L}(\{t_\nu\}; \{n_\nu\})$, with $\nu = 1, 2, ..., 16$;
- Using standard numerical optimization techniques, find the optimum set of variables $\{t_{\nu,opt}\}$ for which the function $\mathcal{L}(\{t_\nu\}; \{n_\nu\})$ has its maximum value. The best estimate for the density matrix is then $\rho_p(\{t_{\nu,opt}\})$.

Physical density matrices

Any matrix in the form $T^\dagger T$ must be positive and Hermitian. In fact positivity reads

$$\langle\psi|T^\dagger T|\psi\rangle = \langle\psi'||\psi'\rangle \geq 0;\ \forall|\psi\rangle, \tag{1.23}$$

with $|\psi'\rangle = T|\psi\rangle$; while hermiticity come from definition

$$(T^\dagger T)^\dagger = T^\dagger (T^\dagger)^\dagger = T^\dagger T. \tag{1.24}$$

To ensure normalization we divide by the trace and we obtain

$$\frac{T^\dagger T}{Tr[T^\dagger T]}. \tag{1.25}$$

It is convenient to choose a tridiagonal form for T:

$$T(\{t_\nu\}) = \begin{pmatrix} t_1 & 0 & 0 & 0 \\ t_5 + \imath t_6 & t_2 & 0 & 0 \\ t_{11} + \imath t_{12} & t_7 + \imath t_8 & t_3 & 0 \\ t_{15} + \imath t_{16} & t_{13} + \imath t_{14} & t_9 + \imath t_{10} & t_4 \end{pmatrix}. \tag{1.26}$$

Thus the general physical density matrix is given by the formula

$$\rho_p(\{t_\nu\}) = \frac{T^\dagger(\{t_\nu\})T(\{t_\nu\})}{Tr[T^\dagger(\{t_\nu\})T(\{t_\nu\})]}. \tag{1.27}$$

Likelihood function

The measurement data consist of a set of 16 coincidence counts $\{n_\nu\}$ whose expected values are $\overline{n_\nu} = \mathcal{N}\langle\psi_\nu|\rho|\psi_\nu\rangle$. Let us assume that the noise on these coincidence measurements has a Gaussian probability distribution. Thus the probability of obtaining a set of 16 counts $\{n_1, n_2, ..., n_{16}\}$ is

$$P(n_1, n_1, ..., n_{16}) = \frac{1}{N_{norm}} \prod_{\nu=1}^{16} exp\left\{-\frac{(n_\nu - \overline{n_\nu})^2}{2\sigma_\nu^2}\right\} \tag{1.28}$$

where σ_ν is the standard deviation for the νth coincidence measurement (given approximately by $\sqrt{\overline{n_\nu}}$ for Poissonian statistics) and N_{norm} is the normalization constant. For our physical density matrix ρ_p the number of counts expected for the νth measurement is

$$\overline{n_\nu}(t_1, t_2, ..., t_{16}) = \mathcal{N}\langle\psi_\nu|\rho_p(t_1, t_2, ..., t_{16})|\psi_\nu\rangle. \tag{1.29}$$

Thus the likelihood that the matrix $\rho_p(t_1, t_2, ..., t_{16}$ could produce the measured data $n_1, n_2, ..., n_{16}$ is

$$P(n_1, n_1, ..., n_{16}) = \frac{1}{N_{norm}} \prod_{\nu=1}^{16} exp\left\{-\frac{(n_\nu - \mathcal{N}\langle\psi_\nu|\rho_p(t_1, t_2, ..., t_{16})|\psi_\nu\rangle)^2}{2\mathcal{N}\langle\psi_\nu|\rho_p(t_1, t_2, ..., t_{16})|\psi_\nu\rangle}\right\}. \tag{1.30}$$

The likelihood function $\mathcal{L}$ is defined as the natural logaritm of the previous formula with inverted sign. Thus finding the maximum for P correspond to finding the minimum for $\mathcal{L}$. The formula for the likelihood function is

$$\mathcal{L}(\{t_\nu\}; \{n_\nu\}) = \sum_{\nu=1}^{16} \frac{(n_\nu - \mathcal{N}\langle\psi_\nu|\rho_p(t_1, t_2, ..., t_{16})|\psi_\nu\rangle)^2}{2\mathcal{N}\langle\psi_\nu|\rho_p(t_1, t_2, ..., t_{16})|\psi_\nu\rangle} \tag{1.31}$$

Numerical optimization

We used the MATHEMATICA 7.0 routine "NMinimize" which minimizes of the function $\mathcal{L}(\{t_\nu\}; \{n_\nu\})$ respect to the 16 parameters $\{t_1, t_2, ..., t_{16}\}$ given the 16 measured value $\{n_1, n_2, ..., n_{16}\}$. We used the sixteen projector defined in table (1.1), the definition of ρ_p from eq. (1.27) and $\mathcal{N} = \sum_{\nu=1}^{4} n_\nu$. From the output of this routine (the parameters $\{t_{1,opt}, t_{2,opt}, ..., t_{16,opt}\}$) we reconstruct the physical density matrix using eq. (1.27).

1.5 The Bell's parameter

The purpose is to compare quantum mechanics with a general local and real hidden variable theory. We follow the lines suggested by Clauser, Horne, Shimony and Holt (CHSH) paper [34].

First of all we want to define the probability of coincidence counting $P(\theta_s, \theta_i)$, with $\theta_{s,i}$ the signal and idler polarization angles, using a real and local hidden variable theory. Consider photon pairs as characterized by an hidden variable λ unknown to the observer. This variable completely determines the results of the measurements and has a distribution function $\rho(\lambda)$ ($\int d\lambda\, \rho(\lambda) = 1$). In such a case λ is an hidden polarization of the photons. Calling α the signal polarizer angle we define the function $A(\lambda, \alpha)$ which is equal to 1 when we see the photon throught signal polarizer at angle α, and to -1 when the photon is detected with the polarizer at angle $\alpha_\perp = \alpha + \pi/2$. We do the same for the idler with angle β and function $B(\lambda, \beta)$. The probabilities of coincidence counting with signal and idler polarizer at angle $\alpha\,(\alpha_\perp)$ and $\beta\,(\beta_\perp)$ are thus

$$\begin{aligned}
P(\alpha, \beta) &= \int d\lambda\, \rho(\lambda) \left(\frac{1 + A(\lambda, \alpha)}{2}\right)\left(\frac{1 + B(\lambda, \beta)}{2}\right) \\
P(\alpha, \beta_\perp) &= \int d\lambda\, \rho(\lambda) \left(\frac{1 + A(\lambda, \alpha)}{2}\right)\left(\frac{1 - B(\lambda, \beta)}{2}\right) \\
P(\alpha_\perp, \beta) &= \int d\lambda\, \rho(\lambda) \left(\frac{1 - A(\lambda, \alpha)}{2}\right)\left(\frac{1 + B(\lambda, \beta)}{2}\right) \\
P(\alpha_\perp, \beta_\perp) &= \int d\lambda\, \rho(\lambda) \left(\frac{1 - A(\lambda, \alpha)}{2}\right)\left(\frac{1 - B(\lambda, \beta)}{2}\right)
\end{aligned} \tag{1.32}$$

It is important to notice that the result is completely predetermined by the value (unknown) of the parameter λ (reality condition) and that the value of $A(\lambda, \alpha)$ is not correlated to the value of $B(\lambda, \beta)$ (locality condition). We introduce the function

$$E(\alpha, \beta) = P(\alpha, \beta) + P(\alpha_\perp, \beta_\perp) - P(\alpha_\perp, \beta) - P(\alpha, \beta_\perp) \tag{1.33}$$

From the definitions in eq. (1.32) we obtain for a real and local theory

$$E(\alpha, \beta) = \int d\lambda\, \rho(\lambda)\, A(\lambda, \alpha) B(\lambda, \beta) \tag{1.34}$$

Then, choosing the angles a, b, a', b' we define the parameter S as

$$S = E(a, b) - E(a, b') + E(a', b) + E(a', b'). \tag{1.35}$$

From eq. (1.34) we obtain the Bell's parameter for a real and local hidden variable theory

$$S = \int d\lambda\, \rho(\lambda)\, s(\lambda, a, b, a', b'), \tag{1.36}$$

with

$$s(\lambda, a, b, a', b') = A(\lambda, a)[B(\lambda, b) - B(\lambda, b')] + A(\lambda, a')[B(\lambda, b) + B(\lambda, b')].$$

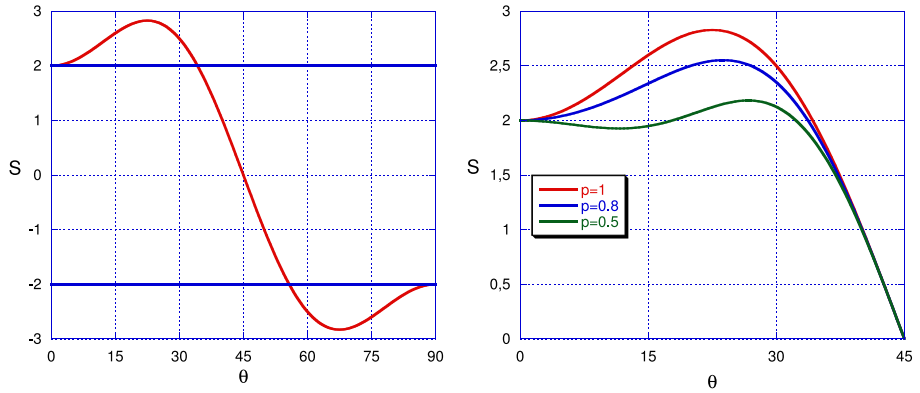

Figure 1.2: *The function $S(\theta)$ calculated using quantum mechanic laws. The limits $|S| \leq 2$ are exceeded only for certain value of θ. On the left we report the case of a maximally entangled state (purity $p = 1$), The maximum occurs for $\theta = 22.5°$ and $S(22.5° = 2\sqrt{2})$. On the right we report the same function for different state purity. Notice that both the maximum value and its position depend on the purity p.*

Since A and B assume only values ± 1, then $s(\lambda, a, b, a', b') = \pm 2$ thus S, which is the average of s, for any local and real theory is

$$|S| \leq 2. \tag{1.37}$$

This result is general and is valid for any real and local theory and does not depend on the assumption done on the observed system.

On the other hand we want to obtain the same parameter using quantum mechanical laws. We write the generic density matrix of a measured state as $\rho_{exp} = p\,\rho_{ent} + (1-p)\rho_{mix}$, where p is the state purity and ρ_{ent}, ρ_{mix} are respectively the maximally entangled state and the statistical mixture defined in sec. 1.3. Using quantum mechanics the coincidence probability with polarizers at angles α and β is

$$\begin{aligned} P(\alpha,\beta) =& \langle\alpha|\langle\beta|\rho_{exp}|\alpha\rangle|\beta\rangle = \\ &= cos^2\alpha\, cos^2\beta + sin^2\alpha\, sin^2\beta + 2\,p\, cos\alpha\, cos\beta\, sin\alpha\, sin\beta. \end{aligned} \tag{1.38}$$

Using the same definition given above in eq. (1.33) and eq. (1.35) and choosing the angles $a = 0$, $b = \theta$, $a' = 2\theta$, $b' = 3\theta$, we obtain the quantum mechanical $S(\theta)$ parameter. The result is depicted in figure. (1.2). We can see that the maximum value of $S(\theta)$ depends on the state purity. For a maximally entangled state ($p = 1$) we have $S(22.5°) = 2\sqrt{2} \simeq 2.828$ which is larger than 2. The Bell parameter S thus allows to discriminate between a real local theory and quantum mechanics. Notice that also the value of θ for which the maximum occur depend on the state purity p.

Chapter 2

Generation of entangled states

In this chapter we will explain the theory behind our experimental generation of entangled state. As we have seen above entanglement occurs when two particle interact somewhere and then become separated. In our source the interaction occurs within nonlinear crystals, thus, in order to give a complete mathematical description of the generated state, we need to better understand the propagation of light in a birefringent media (section 2.1). In fact a non-linear material is always birefringent, *i.e.* the media owns more than one indexes of refraction. Then, in section 2.2 we will explain the Spontaneous Parametric Down Conversion (SPDC): the basic physical phenomena we exploit in the laboratory for photon pairs generation. We will derive the functions which model photon distribution and correlation. Then using a couple of such crystals we generate entangled state in polarization. In section 2.3 we will see how to write the total entangled state and finally, in sec. 2.3.1, we will derive the relative phase term between horizontally and vertically polarized pairs and we calculate an expansion of such phase.

2.1 Wave propagation in a birefringent media

In this first section we will derive from Maxwell's equations the general laws to calculate the eigen-idexes of refraction and the eigen-polarizations of a certain crystal. In sec. 2.1.2 we will describe the ellipsoid method to find the solutions of the above-mentioned problem. In sec. 2.1.3 we will give the results for the uniaxial crystal case and we solve the problem in a more general situation useful for our purposes. Subsequently, in sec. 2.1.4, we will describe the double refraction at an uniaxial crystal surfaces. Finally, in sec. 2.1.5, we will give the formulas for the ordinary and extraordinary optical paths. These will be used to calculate the phase accumulated by the photons travelling within the crystals.

2.1.1 Eigen-indexes of refraction and eigen-polarizations

Maxwell's equations (in MKS units) in a material reads [35]

$$\begin{aligned} \nabla \cdot \mathbf{D} &= \rho; & (2.1)\\ \nabla \cdot \mathbf{B} &= 0; & (2.2)\\ \nabla \times \mathbf{E} &= -\tfrac{\partial \mathbf{B}}{\partial t}; & (2.3)\\ \nabla \times \mathbf{H} &= \mathbf{J} + \tfrac{\partial \mathbf{D}}{\partial \mathbf{t}}; & (2.4) \end{aligned}$$

where ρ and $\mathbf{J}$ are the charge and the current densities inside the medium; $\mathbf{D} = \varepsilon\mathbf{E}$ and $\mathbf{B} = \mu\mathbf{H}$ are, respectively, the electric displacement and the magnetic induction. For an isotropic medium ε and μ are real number, while in an anisotropic material (such as a birefringent crystal) they are tensors and, in general, **D (B)** is not parallel to **E (H)**.

Conservation of energy for electromagnetic fields requires that the time rate of change of electromagnetic energy contained within a certain volume, plus the time rate of energy flowing out through the boundary surfaces of the volume, be equal to the negative of the total work done by the fields on the sources within the volume. This is expressed by the Poynting theorem:

$$\frac{\partial U}{\partial t} + \nabla \cdot \mathbf{S} = -\mathbf{J} \cdot \mathbf{E}, \qquad (2.5)$$

where the electromagnetic energy density U and the Poynting vector $\mathbf{S}$ are defined as

$$\begin{aligned} U &= \tfrac{1}{2}(\mathbf{E} \cdot \mathbf{D} + \mathbf{B} \cdot \mathbf{H}); & (2.6)\\ \mathbf{S} &= \mathbf{E} \times \mathbf{H}. & (2.7) \end{aligned}$$

Poynting vector $\mathbf{S}$ represent the power per unit area carried by the field in the direction of $\mathbf{S}$.

We now address the problem of wave propagation within a birefringent crystal. In an anisotropic material the phase velocities of light depend on its state of polarization as well as its direction of propagation [35]. Because of the anisotropy, the polarization state of a plane wave may vary during the propagation through the crystal. However, given a direction of propagation in the medium, there exist, in general, two eigenwaves with well defined eigen-phase-velocities and polarization directions. A light wave with polarization parallel to one of these directions will remain in the same polarization state as it propagates through the anisotropic medium. These eigen-polarization, as well as the corresponding eigen-phase-velocities (or equivalently eigen-indexes of refraction), can be determined from eqs. (2.3) and (2.4) and the dielectric tensor.

We consider a monocromatic plane wave of angular frequency ω propagating in an anisotropic medium with an electric and magnetic field

$$\begin{aligned} &\mathbf{E}\, e^{\imath(\omega t - \mathbf{k}\cdot\mathbf{r})}, & (2.8)\\ &\mathbf{H}\, e^{\imath(\omega t - \mathbf{k}\cdot\mathbf{r})}, & (2.9) \end{aligned}$$

where the wave vector is $\mathbf{k} = \frac{\omega}{c} n\hat{\kappa}$, with n the refractive index to be determined and $\hat{\kappa}$ the unit vector in $\mathbf{k}$ direction. Substitution for electric and magnetic field from eqs. (2.8) and (2.9), respectively, into Maxwell's equation (2.3) and (2.4) gives

$$\mathbf{k} \times \mathbf{E} = \omega\mu\mathbf{H}, \tag{2.10}$$

$$\mathbf{k} \times \mathbf{H} = -\omega\varepsilon\mathbf{E}. \tag{2.11}$$

From these two equation one simply obtains

$$\mathbf{k} \times (\mathbf{k} \times \mathbf{E}) + \omega^2\mu\varepsilon\mathbf{E} = 0. \tag{2.12}$$

In the principal coordinate system, *i.e* x, y and z axes are chosen in the directions of the eigenvectors of ε, the dielectric tensor ε is given by

$$\varepsilon = \begin{pmatrix} \varepsilon_x & 0 & 0 \\ 0 & \varepsilon_y & 0 \\ 0 & 0 & \varepsilon_z \end{pmatrix}. \tag{2.13}$$

Equation (2.12) can be written as

$$\mathbf{M} \cdot \mathbf{E} = 0, \tag{2.14}$$

with

$$\mathbf{M} = \begin{pmatrix} \omega^2\mu\varepsilon_x - k_y^2 - k_z^2 & k_x k_y & k_x k_z \\ k_y k_x & \omega^2\mu\varepsilon_y - k_x^2 - k_z^2 & k_y k_z \\ k_z k_x & k_z k_y & \omega^2\mu\varepsilon_z - k_x^2 - k_y^2 \end{pmatrix} \tag{2.15}$$

For nontrivial solution to exist, the determinant of $\mathbf{M}$ must be

$$det(\mathbf{M}) = 0. \tag{2.16}$$

The general solution of eq. (2.16) is

$$\frac{|k|^2}{n_x^2}\left[\frac{k_x^2\, n_x^2}{n_y^2 n_z^2} + \frac{k_y^2}{n_z^2} + \frac{k_z^2}{n_y^2} - \frac{\omega^2}{c^2}\right] - \frac{\omega^2}{c^2}\left[k_x^2\left(\frac{1}{n_z^2} + \frac{1}{n_y^2} - \frac{1}{n_x^2}\right) + \frac{k_y^2}{n_z^2} + \frac{k_z^2}{n_y^2} - \frac{\omega^2}{c^2}\right] = 0, \tag{2.17}$$

where we have used the relations $c^2 = \frac{1}{\varepsilon_0\mu}$ and $n_i^2 = \frac{\varepsilon_i}{\varepsilon_0}$ for i=x, y, z. Note that this is a dispersion relation $\omega(\mathbf{k})$. It could be represented by a three dimensional surface in $\mathbf{k}$ space (momentum space). This is known as the normal surface and consists of two shells, which, in general have four points in common. The two lines that go through the origin and these points are known as the optic axes. Given the direction of propagation (k_x, k_y, k_z), there are in general two k values which intercept with the normal surface. These two k values correspond to two different phase velocities $\frac{\omega}{k}$ of the wave propagating along the chosen direction. If we replace $\mathbf{k} = \frac{\omega}{c}\, n\, \hat{\kappa}$ inside eq.

(2.17) we obtain an equation for the refraction index n (two solution). In order to obtain the direction of the electric field vector $\mathbf{E}$ we substitute n found above in the following equation (derived from eq. (2.14))

$$\mathbf{E} = \begin{pmatrix} \frac{k_x}{n^2 - n_x^2} \\ \frac{k_y}{n^2 - n_y^2} \\ \frac{k_z}{n^2 - n_z^2} \end{pmatrix}. \tag{2.18}$$

Using Maxwell's equations and $\mathbf{k} = \frac{\omega}{c} n \hat{\kappa}$ we derive that in a crystal ($\rho = 0$, $\mathbf{J} = 0$)

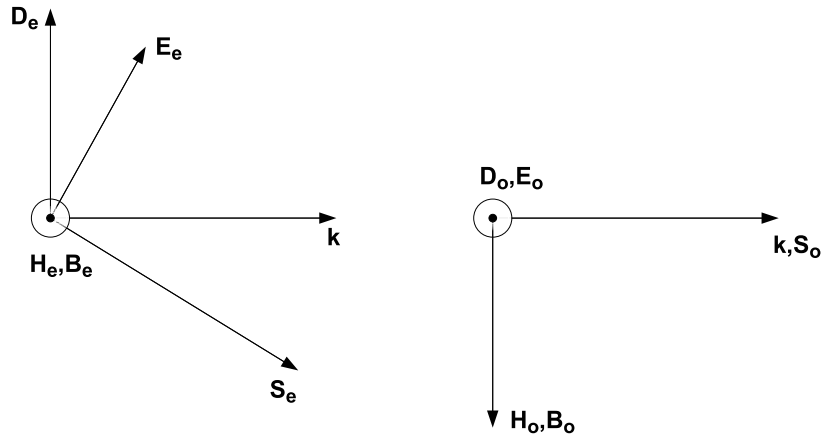

Figure 2.1: *Fields direction in an anisotropic material for extraordinary (left) and ordinary (right) wave propagation.*

$$\begin{aligned} \hat{\kappa} \cdot \mathbf{D} &= 0; & (2.19)\\ \hat{\kappa} \cdot \mathbf{B} &= 0; & (2.20)\\ \mathbf{H} &= \frac{n}{\mu c} \hat{\kappa} \times \mathbf{E}; & (2.21)\\ \mathbf{D} &= -\frac{n}{c} \hat{\kappa} \times \mathbf{H}. & (2.22) \end{aligned}$$

The first two relations means that $\mathbf{D}$ and $\mathbf{B}$ are always orthogonal to the wave vector direction $\hat{\kappa}$. From the third we know that $\mathbf{H}$ is normal to the plane that contain $\mathbf{E}$ and $\hat{\kappa}$, while the fourth add the orthogonality information also between $\mathbf{D}$ and $\mathbf{H}$. In general within an anisotropic material $\mathbf{E}$ and $\mathbf{D}$ are not parallel. The main consequence is that the Poynting vector $\mathbf{S} = \mathbf{E} \times \mathbf{H}$ is not collinear with the wave vector direction $\hat{\kappa}$. This happens for the extraordinary wave. In other words for a certain polarization a light beam (called extraordinary) in an anisotropic material experiments a spatial walk off. However it exists an other polarization (orthogonal to the previous

one) for which ordinary propagation occur (the Poynting vector $\mathbf{S}_o$ is parallel to the wave vector direction $\hat{\kappa}$). These consideration are shown in Fig. (2.1).

2.1.2 Ellipsoid method

A simple method to find the index of refractions and the corresponding polarization directions $\mathbf{D}$ associated with the two independent plane waves propagating along an arbitrary direction $\mathbf{k}$ in a crystal, is exploiting the so called index ellipsoid. The surfaces of constant energy density for the electric field $U_e = \frac{1}{2}(\mathbf{E} \cdot \mathbf{D})$ are:

$$\frac{D_x^2}{\varepsilon_x} + \frac{D_y^2}{\varepsilon_y} + \frac{D_z^2}{\varepsilon_z} = 2\,U_e. \tag{2.23}$$

By replacing $\frac{\mathbf{D}}{\sqrt{2\varepsilon_0 U_e}}$ with $\mathbf{r}$ and defining the principal indexes of refraction n_x, n_y, n_z by $n_i^2 = \varepsilon_i/\varepsilon_0$ (i=x,y,z), the equation above can be written as

$$\frac{x^2}{n_x^2} + \frac{y^2}{n_y^2} + \frac{z^2}{n_z^2} = 1. \tag{2.24}$$

This is the equation of an ellipsoid with mayor axis parallel to x, y, z, whose respective lengths are $2\,n_x$, $2\,n_y$, $2\,n_z$ (see Fig. (2.2)).

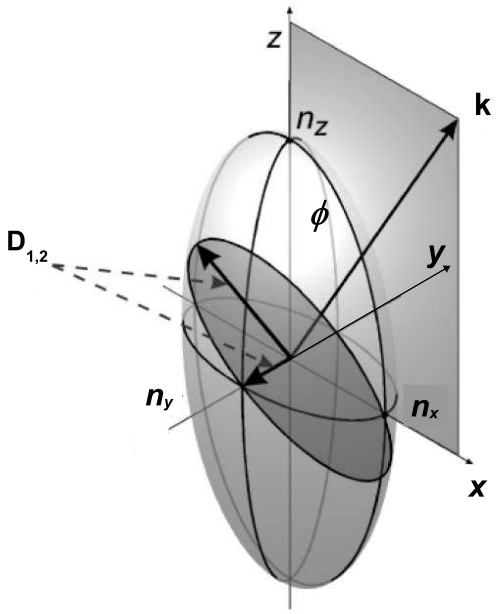

Figure 2.2: *Index ellipsoid method to find the eigen-modes. (x,y,z) are the principal coordinate system.*

The method consists in the following prescription:

- find the intersection ellipse between the index ellipsoid and a plane through the origin that is normal to the propagation direction **k**;
- the two axes of the intersection ellipse are equal in length to $2\,n_1$ and $2\,n_2$ where n_1, n_2 are the two solution of eq. (2.17);
- these axes are parallel to the directions of the vectors $D_{1,2}$ of the allowed solution.

2.1.3 Special case of uniaxial crystal

In general the dielectric tensor components in the principal coordinate system ε_i $(i = x, y, z)$ are different. This is the case of biaxial crystal, since there are two optical axes. There are many crystals in which two components of the dielectric tensor equals ($e.g\, \varepsilon_x = \varepsilon_y = \varepsilon_0 n_o^2$), and so there is only one optical axis. In this section we analyze in details the case of uniaxial crystals. First of all the equation (2.17) can be factored and become

$$\left[\frac{k_x^2 + k_y^2}{n_e^2} + \frac{k_z^2}{n_o^2} - \frac{\omega^2}{c^2}\right]\left[\frac{|k|^2}{n_o^2} - \frac{\omega^2}{c^2}\right] = 0. \tag{2.25}$$

The normal surface in this case consists of a sphere and an ellipsoid of revolution. Notice that for every direction of propagation one of the two eigen-index of refraction is ordinary.

Consider the wave vector $\mathbf{k} = \frac{\omega}{c} n\,\hat{\kappa}$ lying in the (x,z) plane and forming an angle ϕ with the z-axis (optical axis), as depicted in Fig. (2.2). We substitute the wave vector **k** with direction $\hat{\kappa} = (sin(\phi),\, 0,\, cos(\phi))$ inside eq. (2.25), and we obtain two solution for n:

$$n_1 = n_o, \text{ and} \tag{2.26}$$

$$\frac{1}{n_2^2(\phi)} = \frac{cos^2(\phi)}{n_o^2} + \frac{sin^2(\phi)}{n_e^2}. \tag{2.27}$$

The second expresses the refraction index for the extraordinary wave depending on the angle between the optical axes and the propagation direction. The extraordinary electric field $\mathbf{E_e}$ can be calculated from eq. (2.18) and results

$$\mathbf{E_e} = E_{e0} \cdot \begin{pmatrix} -\frac{1}{n_o^2 sin(\phi)} \\ 0 \\ \frac{1}{n_e^2 cos(\phi)} \end{pmatrix}, \tag{2.28}$$

while the ordinary electric field is

$$\mathbf{E_o} = E_{o0} \cdot \begin{pmatrix} 0 \\ 1 \\ 0 \end{pmatrix}. \tag{2.29}$$

Please note that $\mathbf{E_e} \cdot \mathbf{k} \neq 0$, while for the electric displacement

$$\mathbf{D_e} = \varepsilon \mathbf{E_e} = \varepsilon_0 \, E_{e0} \begin{pmatrix} -\frac{1}{sin(\phi)} \\ 0 \\ \frac{1}{cos(\phi)} \end{pmatrix}, \tag{2.30}$$

the orthogonality relation $\mathbf{D_e} \cdot \mathbf{k} = 0$ holds. We calculate the magnetic field $\mathbf{H_e}$ from equation (2.21). It reads

$$\mathbf{H_e} = -\frac{n}{\mu c} E_{e0} \begin{pmatrix} 0 \\ \frac{cotan(\phi)}{n_o^2} + \frac{tan(\phi)}{n_e^2} \\ 0 \end{pmatrix}, \tag{2.31}$$

hence the Poynting vector $\mathbf{S_e} = \mathbf{E_e} \times \mathbf{H_e}$ is

$$\mathbf{S_e} = E_{e0} |H_y| \cdot \begin{pmatrix} \frac{1}{n_e^2 cos(\phi)} \\ 0 \\ \frac{1}{n_o^2 sin(\phi)} \end{pmatrix}. \tag{2.32}$$

Defining ρ the angle between the wave vector $\mathbf{k}$ and the Poynting vector $\mathbf{S_e}$ (positive in the anti-clockwise direction); from the above equation we calculate the fraction $\frac{S_x}{S_z} = \frac{n_o^2}{n_e^2} tan(\phi) = tan(\phi - \rho)$ and we derive the walk-off angle

$$\rho = \phi - atan \left(\frac{n_o^2}{n_e^2} \, tan(\phi) \right). \tag{2.33}$$

In the case of positive crystals ($n_e > n_o$) the walk-off angle ρ is positive (close to the optical axes). In the opposite case ($n_e < n_o$) the Poynting vector go further from the optical axes ($\rho < 0$).

General situation

We now consider the more generic situation of a wave propagating in an other plane. We now consider (x, y, z) as the principal coordinate system of the crystal (z is the optical axis direction) and (x', y' , z') the laboratory coordinate system. In the system of the laboratory the optical axes lies in the (y', z') plane, while the propagation direction $\hat{\kappa}$ lies in the (x', z') plane (see Fig. (2.3). The following rotation allows coordinate system transformation:

$$\begin{pmatrix} x' \\ y' \\ z' \end{pmatrix} = \begin{pmatrix} 0 & 1 & 0 \\ -cos(\phi) & 0 & sin(\phi) \\ sin(\phi) & 0 & cos(\phi) \end{pmatrix} \cdot \begin{pmatrix} x \\ y \\ z \end{pmatrix}. \tag{2.34}$$

In the principal coordinate system the wave vector $\mathbf{k}$ has direction $\hat{\kappa} = (sin\phi \, cos\theta, \, sin\theta, \, cos\phi \, cos\theta)$ and if we substitute it inside eq. (2.25) we obtain the two solution for the refractive indexes:

$$n_1 = n_o, \text{ and} \tag{2.35}$$

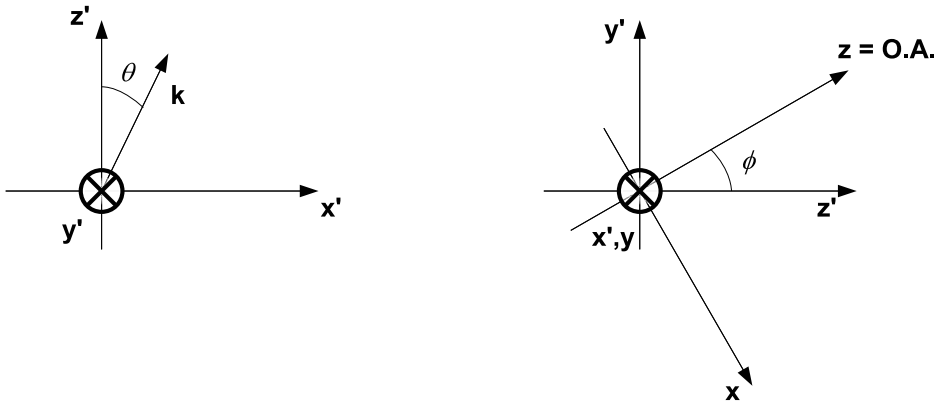

Figure 2.3: *(x,y,z) are the principal coordinates, while (x', y', z') are the laboratory coordinates.*

$$\frac{1}{n_2^2(\phi,\theta)} = \frac{cos^2\phi\, cos^2\theta}{n_o^2} + \frac{sin^2\phi\, cos^2\theta + sin^2\theta}{n_e^2}. \tag{2.36}$$

The extraordinary electric field direction, calculated from eq. (2.18) is

$$\mathbf{E_e} = E_{e0} \cdot \begin{pmatrix} -\frac{sin\phi\, cos\theta}{n_o^2(sin^2\theta + cos^2\theta\, sin^2\phi)} \\ -\frac{sin\theta}{n_o^2(sin^2\theta + cos^2\theta\, sin^2\phi)} \\ \frac{1}{n_e^2 cos\theta\, cos\phi} \end{pmatrix}, \tag{2.37}$$

while the extraordinary electric displacement $\mathbf{D_e} = \varepsilon \mathbf{E_e}$ is

$$\mathbf{D_e} = \varepsilon_0 E_{e0} \cdot \begin{pmatrix} -\frac{sin\phi\, cos\theta}{(sin^2\theta + cos^2\theta\, sin^2\phi)} \\ -\frac{sin\theta}{(sin^2\theta + cos^2\theta\, sin^2\phi)} \\ \frac{1}{cos\theta\, cos\phi} \end{pmatrix}. \tag{2.38}$$

In order to derive the electric displacement direction for the ordinary field we apply the ortogonality relation

$$\mathbf{D_o} = \frac{\mathbf{D_e} \times \mathbf{k}}{|\mathbf{D_e} \times \mathbf{k}|} = \begin{pmatrix} -sin\theta \\ cos\theta\, sin\phi \\ 0 \end{pmatrix}. \tag{2.39}$$

Notice that for $\theta = 0$ all these relation reduces to the ones derived in section 2.1.3. If we write these vector in the laboratory reference frame (x', y', z') we obtain

$$\mathbf{D'_e} \propto \begin{pmatrix} -sin\theta \\ \frac{tan\phi}{cos\theta} \\ tan\theta\, sin\theta \end{pmatrix};\ \mathbf{D'_o} \propto \begin{pmatrix} cos\theta\, sin\phi \\ sin\theta\, cos\phi \\ -sin\theta\, sin\phi \end{pmatrix}. \tag{2.40}$$

The magnetic field vector $\mathbf{H_e}$ calculated using eq.(2.21) and the Poynting vector $\mathbf{S_e} = \mathbf{E_e} \times \mathbf{H_e}$ in the principal coordinate system are

$$\mathbf{H_e} \propto \begin{pmatrix} sin\theta \\ -cos\theta\, sin\phi \\ 0 \end{pmatrix} \text{ and } \mathbf{S_e} \propto \begin{pmatrix} tan\phi \\ \frac{tan\theta}{cos\phi} \\ \frac{n_e^2}{n_o^2} \end{pmatrix}. \tag{2.41}$$

In the laboratory reference frame the Poynting vector become

$$\mathbf{S'_e} \propto \begin{pmatrix} \frac{tan\theta}{cos\phi} \\ sin\phi(\frac{n_e^2}{n_o^2} - 1) \\ \frac{1}{cos\phi}(sin^2\phi + \frac{n_e^2}{n_o^2}cos^2\phi) \end{pmatrix} = |\mathbf{S'_e}| \begin{pmatrix} cos\theta_y\, sin\theta_{xz} \\ sin\theta_y \\ cos\theta_y\, cos\theta_{xz} \end{pmatrix}; \tag{2.42}$$

where θ_y is the angle between the Poynting vector and its projection on the *(x',y')* plane, while θ_{xz} is the angle between this projection and the *z'* axes. The following result will be useful in optical path calculation

$$\theta_{xz} = atan\left(\frac{S'_{ex}}{S'_{ez}}\right) = atan\left(\frac{tan\theta}{sin^2\phi + \frac{n_e^2}{n_o^2}cos^2\phi}\right). \tag{2.43}$$

This angle will be important in the following chapter, when we will calculate the phase accumulated by photon pairs during their propagation.

2.1.4 Double refraction at a boundary

Consider a plane wave incident on the surface of an anisotropic crystal. The refracted wave, in general, is a mixture of the two eigen-modes. In uniaxial crystal it is a mixture of the ordinary and extraordinary wave. The boundary condition implies that the wave vectors lie in the incident plane (x,z) and their tangential component along the boundary be the same. We call $\mathbf{k_0}$ the wave vector of the incident wave, and $\mathbf{k_1}$, $\mathbf{k_2}$ the wave vectors of the refracted waves. The boundary condition for the tangential component implies

$$k_0\, sin(\theta_0) = k_1\, sin(\theta_1) = k_2\, sin(\theta_2). \tag{2.44}$$

It looks like the Snell law but it is important to note that k_1, k_2, in general, are not constant; rather, they vary with the directions of the vectors $\mathbf{k_1}$, $\mathbf{k_2}$.

We now consider the case of uniaxial crystal. One refracted wave is ordinary, say k_1; its displacement vector is orthogonal to the plane containing the optical axis and the propagation direction and k_1 does not depend on the angle θ_1. The ordinary wave thus obeys Snell law $n_i\, sin(\theta_0) = n_o\, sin(\theta_1)$, where n_i is the refraction index of the incident medium. The extraordinary wave refraction is more complex since k_2 depends on the angle θ_2 and also on the optical axes direction. The simplest case is the optical axis lying in

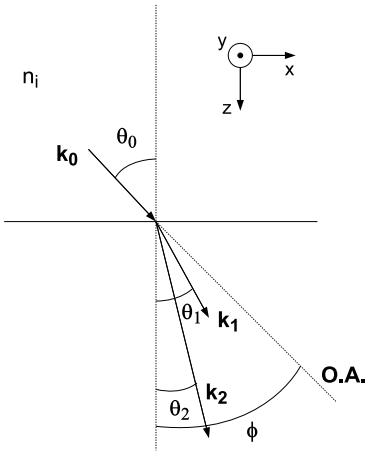

Figure 2.4: *Double refraction at a boundary. Optical Axes in the incident plane.*

the same plane of incidence (x,z). In such a case, calling ϕ the angle between the optical axis of the crystal and the z-axes, the extraordinary wave vector modulus is $k_2 = \frac{\omega}{c} n_2(\phi - \theta_2)$ with n_2 from eq. (2.27) and the refraction condition (2.44) becomes

$$n_i \, sin(\theta_i) = n_2(\phi - \theta_2) \, sin(\theta_2). \tag{2.45}$$

In the case of optical axes in the orthogonal plane (y,z) tilted by ϕ respect to the z-axes, the situation is a bit more complicated. First of all for uniaxial crystal one of the two refracted wave is always ordinary. The extraordinary refracted index for this situation is the one expressed in eq. (2.36). The main difficulty is to solve the following mathematical problem for θ_2

$$n_i \, sin(\theta_i) = n_2(\phi, \theta_2) \, sin(\theta_2). \tag{2.46}$$

In both situation the ordinary wave is orthogonal polarized respect to the plane formed by the optical axis and the propagation direction, while the extraordinary field lies in that plane and the corresponding displacement is normal to the propagation direction. For the second situation analyzed above these polarization are expressed in eq. (2.40) with the correspondence $\theta_2 = \theta$.

These results about the refraction will be important in the analysis of our source because, as we will see, photons which are generated ordinary in the first crystal, then travel extraordinary in the second one.

2.1.5 Optical paths calculation

Inside a birefringent crystal the wave front is orthogonal to the wave vector **k** but the energy flow and the group velocity follow the direction of the Poynting vector **S**. Consider the two situation depicted in Fig. (2.5). On

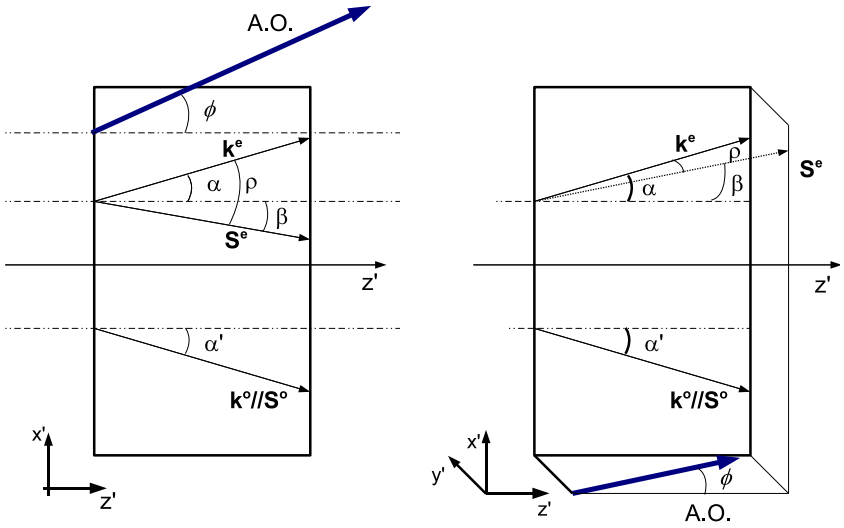

Figure 2.5: *Ordinary and extraordinary optical paths. On the left we report the case in which the optical axis lies in the plane of propagation; here the extraordinary optical path is calculated from eq. (2.49). On the right we report the case in which the optical axis lies in a plane ortogonal to the propagation plane and the extraordinary optical path is calculated from eq. (2.50). In both cases the ordinary optical path is reported in eq. (2.47).*

the left we show the situation with optical axis (O.A.) lies in the plane of propagation (x', z') while on the right the optical axis lies in a plane orthogonal to the propagation plane. We indicate with α (α') the angle formed by the extraordinary (ordinary) wave vector with the z' axis; ρ is the angle between $\mathbf{k^e}$ and $\mathbf{S^e}$ (the walk off angle) and β is the angle between $\mathbf{S^e}$ and the z' axis. Call L the crystal length. In the case of ordinary propagation the optical path in both situation is

$$\phi^o = k^o(\omega)\frac{L}{cos\alpha'} = \frac{\omega}{c}n^o(\omega)\frac{L}{cos\alpha'}, \tag{2.47}$$

while the general formula for the extraordinary optical path is [36]

$$\phi^e = \frac{\omega}{c}n^e(\phi,\omega)\frac{L}{cos\beta}\frac{\mathbf{k^e}\cdot\mathbf{S^e}}{|\mathbf{k^e}\cdot\mathbf{S^e}|} = k^e(\phi,\omega)\frac{L}{cos\beta}cos\rho. \tag{2.48}$$

Here $\frac{L}{cos\beta}$ takes into account the path in the **S** direction, while the dot product $\mathbf{k^e}\cdot\mathbf{S^e}$ accounts for the fact that, although the light travels along

$\mathbf{S^e}$, its wavefronts are perpendicular to $\mathbf{k^e}$, creating a smaller effective optical path length by a factor of the cosine of the angle ρ between these vectors. The last equation is different in the two situation since if the optical axis is in the propagation plane (Fig. (2.5 (left))) then $\beta = \alpha - \rho$ while in the other case (Fig. (2.5 (right)) $cos\beta = cos\rho\, cos\alpha$. Then the optical paths become respectively

$$\phi^e_{\parallel} = \frac{\omega}{c} n^e(\phi,\omega) \frac{L}{cos(\alpha-\rho)} cos\rho, \text{ and} \tag{2.49}$$

$$\phi^e_{\perp} = \frac{\omega}{c} n^e(\phi,\omega) \frac{L}{cos\alpha}. \tag{2.50}$$

These formulas will be very important in the calculation of the phase accumulated by the photons during the propagation within the crystals.

2.2 The Spontaneous Parametric Down Conversion

In this section we will explain how to treat mathematically the physical phenomena of Spontaneous Parametric Down Conversion (SPDC) within nonlinear crystals.

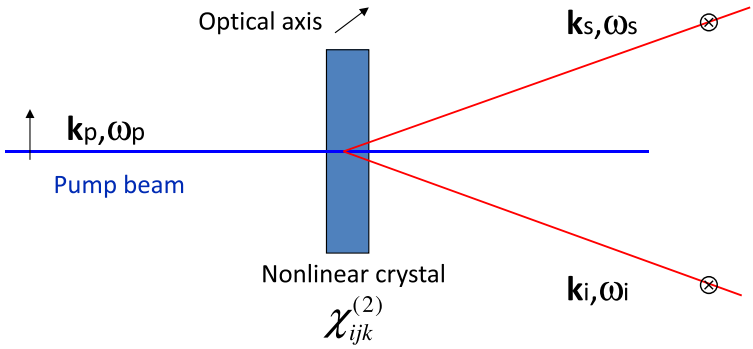

Figure 2.6: *Type-I Spontaneous Parametric Down Conversion.*

An electric field $\mathbf{E}$ in a material induces a polarization $\mathbf{P}$ of the molecules and the total field is defined as displacement vector

$$\mathbf{D} = \varepsilon_0 \mathbf{E} + \mathbf{P}.$$

In isotropic media $\mathbf{P} = \varepsilon_0 \chi \mathbf{E}$ with χ a scalar, so $\mathbf{P}$ and $\mathbf{E}$ are always parallel. In the case of anisotropic media (like crystals) the polarization component

are defined as

$$P_i = \varepsilon_0[\chi^{(1)}_{ij} E_j + \chi^{(2)}_{ijk} E_j E_k + \chi^{(3)}_{ijkl} E_j E_k E_l + \cdots];$$

$\chi^{(1)}$, $\chi^{(2)}$, $\chi^{(3)}$ are a tensors, and we consider the sum over repeated index. The polarization component P_i depends by the electric field vector in such a way because of the anisotropies in the molecular structure. The linear term $\varepsilon^{(1)} = \varepsilon_0(1+\chi^{(1)})$ basically influences the wave propagation, and from it we derive the indexes of refraction and the group velocities of the waves inside the crystal as we have seen above (chapter 2.1). In the following we fix our attention on the second order non-linear term $\chi^{(2)}$.

Consider a second order nonlinear crystal of volume V pumped by a laser beam. Since the electric field energy density is

$$\rho = \tfrac{1}{2} E_i D_i = \rho_0 + \rho_{NL} = \tfrac{1}{2}\varepsilon_0\, E_i \cdot [E_i + \chi^{(1)}_{ij} E_j] + \tfrac{1}{2}\varepsilon_0 \chi^{(2)}_{ijk} E_i E_j E_k + \ldots,$$

the total Hamiltonian is $H = \int_V dr^3 \rho = H_0 + H_{int}$ where H_0 is the energy of the field inside the medium and the interesting part is the interaction Hamiltonian defined as

$$H_{int} = \int_V dr^3 \rho_{NL} = \tfrac{1}{2}\varepsilon_0 \int dr^3 \chi^{(2)}_{ijk} E_i E_j E_k. \tag{2.51}$$

Since the pump power on the crystal is low we can solve the Schrödinger equation $\imath\hbar\frac{\partial}{\partial t}|\varphi\rangle = H_{int}|\varphi\rangle$ in the perturbative regime, thus, starting from the vacuum $|0\rangle = |0\rangle_s|0\rangle_i$, we obtain

$$|\varphi(t)\rangle \simeq |0\rangle - \tfrac{\imath}{\hbar}\int_0^T dt\, H_{int}|0\rangle, \tag{2.52}$$

where T is the interaction time. Note that it is an interaction between three electric field; the first is the pump and the other two are usually called signal and idler and are generated in the non linear process inside the crystal. For a pulsed laser the interaction time T is the pulse duration, while for a continuous wave laser (as in our case) the interaction time is infinite.

We write the pump electric field as a classical radiation

$$\mathbf{E}_p = \mathbf{e}_p\, A_p\, e^{-\imath(\omega_p\, t - \mathbf{k}_p\cdot\mathbf{r})} + c.c.;$$

while for signal and idler we use the quantization form of the electromagnetic field:

$$\widehat{\mathbf{E}}_{s,i} = \imath\, \mathbf{e}_{s,i} \sqrt{\tfrac{\hbar\,\omega_{s,i}}{2\,\varepsilon_0 V}}\, \widehat{a}_{s,i}\, e^{-\imath(\omega_{s,i}\, t - \mathbf{k}_{s,i}\cdot\mathbf{r})} + c.c.,$$

where $\widehat{a}_{s,i}$ is the annihilation operator for the electric field in the modes $s,i = (\omega_{s,i}, \mathbf{k}_{s,i})$ and where $\mathbf{e}_p$, $\mathbf{e}_s$, $\mathbf{e}_i$ are unitary vectors indicating field

polarizations. Considering a single spatial and temporal mode for the pump, the Eq. (2.52) reads

$$|\varphi(t)\rangle \propto \int_{-\infty}^{\infty} dt \int_V dr^3 d_{eff} A_p \, e^{-\imath(\omega_p-\omega_s-\omega_i)t} \, e^{\imath(\mathbf{k}_p-\mathbf{k}_s-\mathbf{k}_i)\cdot\mathbf{r}} \, \hat{a}_s^\dagger \hat{a}_i^\dagger |0\rangle. \quad (2.53)$$

The coefficient $d_{eff} = \chi^{(2)}_{ijk} e_p^i e_s^j e_i^k$ gives the amplitude probability of the process depending on the susceptibility tensor components and fields polarizations. As a first result, for an infinite interaction time and volume, one obtain a pair of single photons $|1\rangle_s|1\rangle_i$ in the modes s and i of signal and idler which satisfy the conditions:

$$\Diamond \quad \text{energy conservation } \Delta\omega = \omega_p - \omega_s - \omega_i = 0; \quad (2.54)$$

$$\Diamond \quad \text{momentum conservation } \Delta\mathbf{k} = \mathbf{k}_p - \mathbf{k}_s - \mathbf{k}_i = 0. \quad (2.55)$$

We split the momentum conservation in two parties: the transverse component $\Delta k_\perp$ and the longitudinal one $\Delta k_\parallel$, which read

$$\Delta k_\parallel = k_p - k_{s\parallel} - k_{i\parallel}; \quad (2.56)$$

$$\Delta k_\perp = k_{s\perp} + k_{i\perp}. \quad (2.57)$$

In the real case, for a monochromatic and continuous wave (CW) pump beam the interaction time is infinite, and thus the energy is conserved, but the integration volume V is limited by the crystal sizes: lenght L and transverse dimension D. We consider a gaussian transverse profile for the pump field $B(\rho) = e^{-\frac{(\rho-\rho_0(z))^2}{w^2}}$ with waist w and centre $\rho_0(z) = (x_0 + z\,tan(\varphi^x_{wo}), y_0 + z\,tan(\varphi^y_{wo}))$, φ_{wo} is the walk off angle which usually is non-zero only in one direction; the integral in equation (2.53) becomes the product of:

$$h(\Delta\omega) = \int_{-\infty}^{\infty} dt \, e^{\imath\Delta\omega\, t} = \delta\left(\frac{\Delta\omega}{2\pi}\right), \quad (2.58)$$

$$f(\Delta k_{tot}) = \int_0^L dz \, e^{\imath\Delta k_{tot} z} = L e^{\imath\frac{\Delta k_{tot} L}{2}} sinc\left(\tfrac{L}{2}\Delta k_{tot}\right) \quad (2.59)$$

and

$$g(\Delta k_\perp) = \int_{-D/2}^{D/2} d\rho \, B(\rho) e^{-\imath\Delta k_\perp \rho} = e^{-\frac{w^2}{4}\Delta k_\perp^2} e^{-\imath\rho_0(0)\,\Delta k_\perp}, \; if \; D \gg 2w, \quad (2.60)$$

with $\Delta k_{tot} = \Delta k_\parallel - \Delta k_\perp tan(\varphi_{wo})$, The function $h(\Delta\omega)$ in eq. (2.58) is thus the Dirac function $\delta(\Delta\omega/2\pi)$ while the functions (2.59) and (2.60) gives respectively the angular and spectral dispersion of the photons pairs and their spatial correlation. Furthermore the pump beam in the general case is not monochromatic thus we may consider its spectrum $A_p = A_p(\omega_p)$. Summing over all the possible frequencies and angles allowed we write the total state

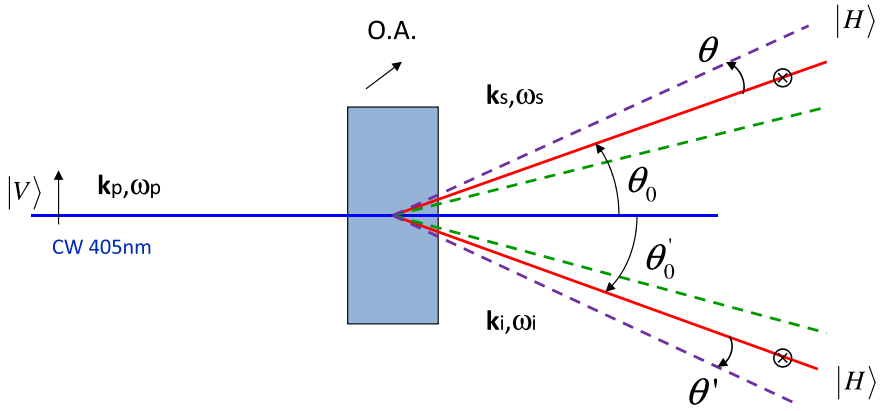

Figure 2.7: *Type-I Spontaneous Parametric Down Conversion inside a nonlinear crystal. A photon from a pump laser polarized in the optical axis plane ($|V\rangle$ in figure) generates a couple of dougther horizontally polarized photons which conserve energy and momentum. Depending on crystal lenght L, the angular and spectral distribution could be rather large. The distribution is given by the function f in eq. (2.59). For large pump beam radius and narrow spectrum the photons are angularly correlated. In general the amount of angular correlation is contained in the g function (eq. (2.60)). In fact if g is a $\delta-$like function, the transverse momentum is perfectly conserved, and from the knowledge of signal frequency and emission angle we know exactly the emission angle of the idler photon.*

resulting from Spontaneous Parametric Down Conversion (SPDC) as the superposition state:

$$|\varphi\rangle \propto \int d\omega_p d\omega_s d\theta d\theta' A(\omega_p) g(\omega_s, \theta, \theta') f(\omega_p, \omega_s, \theta, \theta') |\theta, \omega_s\rangle |\theta', \omega_p - \omega_s\rangle. \tag{2.61}$$

Here $|\theta, \omega_s\rangle$ ($|\theta', \omega_p - \omega_s\rangle$) is a single photon in the Fock state $|1\rangle$ with θ (θ') and ω_s ($\omega_p - \omega_s$) the signal (idler) angular and spectral variables ($\omega_i = \omega_p - \omega_s$ for energy conservation).

The rate R_s of signal photon integrated over all solid angles, and in the spectral window $\delta\lambda$ is proportional to the crystal length L and to the pump power P_p and reads [38, 39]

$$R_s = \mathcal{N}(2\pi)^3 \frac{2\,\lambda_p\, d_{eff}^2}{\varepsilon_0\, n_p^2\, \lambda_s^4\, \lambda_i^2(\lambda_p, \lambda_s)} P_p \cdot L \cdot \delta\lambda_s, \tag{2.62}$$

where $d_{eff} = 2\,pm/V$ for type-I SPDC in a BBO crystal, n_p is the pump refractive index. The term $\mathcal{N} = \alpha \cdot QE \cdot T_{pol} \cdot T_F \cdot C$ accounts for coupling

and detection efficiency; in particular $\alpha \simeq 0.02$ is the portion of the SPDC cone that we select with the slit and the iris (the experimental setup will be explained in detail in the following, see Fig. (3.1)); $QE \simeq 0.13\%$ is the mean detector quantum efficiency, while $T_{pol} \simeq 0.8$ and T_F are respectively the transmittivity of the polarizer and the maximum value of the spectral filter (for the interference filter it is 0.5, for the longpass filter it is 0.85). Finally C is the coupling efficiency. For a spectral window $\delta\lambda = 10\,nm$ and pump power $P_p = 1\,mW$ and considering the coupling efficiency $C = 1$ (overestimated), we calculate a rate $R_s \simeq 1300\,counts/s/mW$, while using a large spectrum ($\delta\lambda \simeq 150\,nm$) we calculate a rate $R_s \simeq 33500\,counts/s/mW$.

The polarization of these photon pairs results from phase matching condition. Writing the momentum as $k = \frac{\omega}{c} n(\omega)$, with c the speed of light in the vacuum, and considering the degenerate case $\omega_s = \omega_i = \frac{\omega_p}{2}$ in the collinear case the condition (2.55) becomes $n(\omega_p) = n(\omega_s)$. Since in normally dispersive materials both ordinary and extraordinary refractive indexes increase with frequency, the previous condition could not be satisfied if pump and down-converted beams are of the same type (ordinary or extraordinary). Such condition could be satisfied considering pump and photons with different polarization. There exists different type of phase matching depending on which beams are ordinary or extraordinary. In the type-I the pump is extraordinary and signal and idler are both ordinary. This means that pump polarization is parallel to the plane containing the optical axes (O.A.) and the direction of propagation $\mathbf{k}_p$, while signal (idler) polarization are orthogonal to the plane formed by the O.A. and $\mathbf{k}_s$ ($\mathbf{k}_i$) (see Sec. (2.1.3)). As we have seen previously in Sec. (2.1.3) the extraordinary refractive index is direction dependent and is calculated from

$$\frac{1}{n_e^2(\phi,\omega)} = \frac{cos^2(\phi)}{n_o(\omega)^2} + \frac{sin^2(\phi)}{n_e(\omega)^2};$$

with ϕ the angle formed by the O.A. and the direction of propagation $\mathbf{k}_p$, n_o (n_e) the ordinary (extraordinary) refractive index of the crystal. It exists a certain angle ϕ_{PM} for which the indexes of refraction match and Eq. (2.55) reads

$$n_e(\phi_{PM}, \omega_p) = n_o(\omega_s) \;\text{ (degenerate and collinear case).} \tag{2.63}$$

When we pump a non-linear crystal with a laser beam polarized in the plane containing the O.A. and the propagation vector $\mathbf{k}_p$ (say vertical direction of the laboratory reference frame), upon setting $\phi = \phi_{PM}$ the generation of photon pairs occurs. In the collinear case ($\mathbf{k}_p \parallel \mathbf{k}_s \parallel \mathbf{k}_i$) the polarization of signal and idler are parallel and perfectly orthogonal to pump polarization (say horizontal in the laboratory coordinates).

2.2.1 Non collinear configuration and spatial correlation

In our apparatus the crystals are β-Barium Borate (BBO) of length L setted for non collinear pairs generation ($\theta_0 = 3°$). We obtain this configuration tilting a bit the phase matching angle found for the collinear case, from a simulation we found $\phi_{PM} = 29.24°$. The equations (2.56) and (2.57) become respectively

$$\begin{aligned} \Delta k_{\parallel} &= k_p^e(\phi, \Omega_p^0 + \omega_p) - k_s^o(\tfrac{\Omega_p^0}{2} + \omega_s)\, cos(\tfrac{\theta_0+\theta}{n_o}) - k_i^o(\tfrac{\Omega_p^0}{2} + \omega_p - \omega_s)\, cos(\tfrac{\theta_0'+\theta'}{n_o}) \\ \Delta k_{\perp} &= k_s^o(\tfrac{\Omega_p^0}{2} + \omega_s)\, sin(\tfrac{\theta_0+\theta}{n_o}) + k_i^o(\tfrac{\Omega_p^0}{2} + \omega_p - \omega_s)\, sin(\tfrac{\theta_0'+\theta'}{n_o}), \end{aligned} \tag{2.64}$$

where k^o, k^e stay for ordinary and extraordinary wave vectors and we have called $\Omega_p^0 = 2\pi\, c/\lambda_p^0$ the central pump frequency ($\lambda_p^0 = 405\, nm$); consequently $\Omega_p^0/2$ is the central frequency for signal and idler. We call ω_p and ω_s the pump and signal frequency shift from the central frequencies, while θ and θ' are signal and idler angular shift from the central external angles θ_0 and $\theta_0' = -\theta_0$. We have used the Snell relation $\theta_1 = asin(\frac{sin(\theta_0+\theta)}{n_o}) \approx \frac{\theta_0+\theta}{n_o}$ and $\theta_1' = asin(\frac{sin(\theta_0'+\theta')}{n_o}) \approx \frac{\theta_0'+\theta'}{n_o}$; θ_1, θ_1' are the internal generation angles, while $\theta_0 + \theta$ and $\theta_0' + \theta'$ are the external angles. Here the phase matching condition reads:

$$n_e(\phi_{PM}, \Omega_p^0) = n_o(\Omega_p^0/2)\, cos\left(\frac{\theta_0}{n_o(\Omega_p^0/2)}\right). \tag{2.65}$$

Spatial correlation

The photons of a couple created by Spontaneous Parametric Down Conversion are intrinsically entangled in frequencies and angles since they must conserve energy and momentum of the pump. Consider for instance a situation in which the pump beam radius on the pump is large enough to consider the function $g(\Delta k_{\perp})$ defined in eq. (2.60) like a delta function $\delta(\Delta k_{\perp})$. In such a case the transverse momentum expressed in eq. (2.64) is conserved (*i.e* $\Delta k_{\perp} = 0$). If we expand this condition to the first order in θ, θ' and ω_s we obtain the relation:

$$\theta' = -\theta + \gamma\omega_s. \tag{2.66}$$

Note that the variables θ, θ' and ω_s are shift from the central angles and frequency. This relation means that if we fix the frequency ω_s, the angles are anticorrelated: the two photons angles increase in the opposite directions; while if we fix the angle θ, the correlated photon angle θ' changes following the frequency variation. Such relation implies that considering a narrow SPDC spectrum we can observe spatial correlation, while using a large spectrum the spatial correlations are washed out. On the other hand when the transverse momentum is not conserved (*i.e.* smaller pump beam radius on the crystals) the relation in eq. (2.66) does not hold. As a consequence the

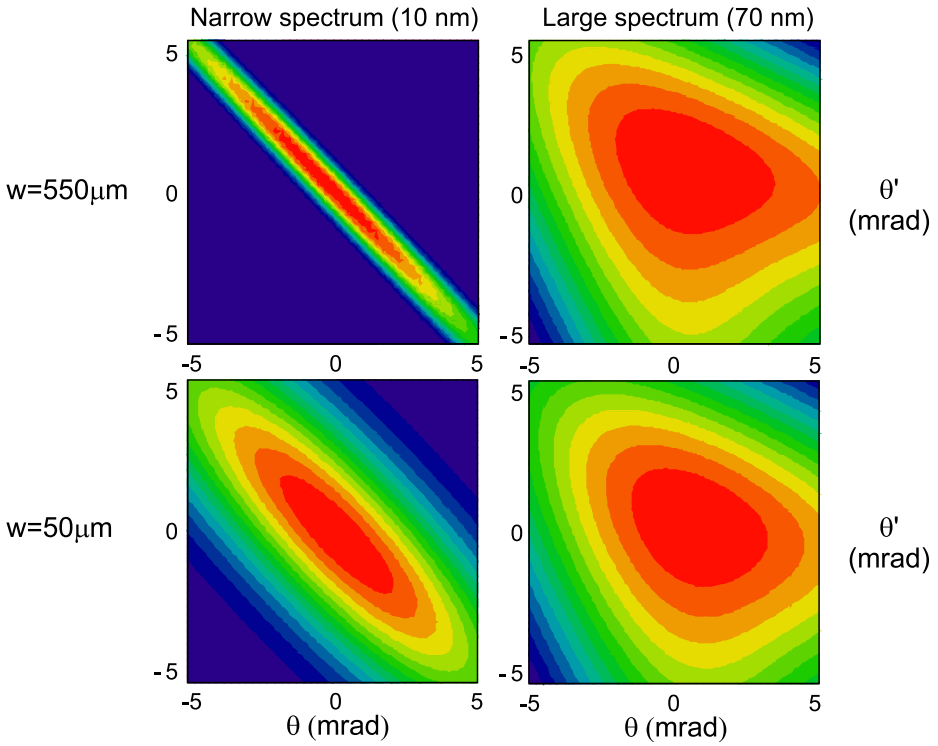

Figure 2.8: *Spatial correlation simulation: the color map represents the coincidence probability for different signal and idler angles (θ and θ' are the shift from central angles $\theta_0 = 3°$ and $\theta'_0 = -3°$). The upper panel are for large pump beam waist (transverse momentum conserved). Strong spatial correlation is visible only for narrow spectral filtering (upper left panel). The large spectrum washed out all spatial correlations (upper right panel). The lower panels represent a situation for smaller beam waist. It is evident that spatial correlation are lost in both cases.*

spatial correlation is gradually lost. Fig. (2.8) reports the simulation result in these conditions. The axes represent the signal and idler angular shift from the central angles θ_0, θ'_0. The color map represent the probability of coincidence counts between the two detectors as a function of the emission angles, evaluated as

$$P_c(\theta,\theta') = \int d\omega_s\, d\omega_p |A(\omega_p) f(\omega_p,\omega_s,\theta,\theta') g(\omega_s,\theta,\theta')|^2\, F(\omega_s) F'(\omega_p-\omega_s) \tag{2.67}$$

where F and F' are spectral filters respectively on signal and idler. In the simulation we used an interference filter with $10\,nm$ bandpass centered around $810\,nm$ and a long pass filter transmitting photons above $715\,nm$.

The effect of detectors quantum efficiency is included in the filters as a slow cut off above $800\,nm$. The upper panels show the situation in which the pump beam waist is large enougth to consider the transverse momentum conserved: the spatial correlation appears only for a narrow spectrum (left panel). In the lower panel the transverse momentum conservation does not hold and in both situation the spatial correlations disappear.

2.3 Entangled state in polarization: the two crystal geometry

Our aim is to generate entangled state in polarization. First of all we use two identical non linear crystals, set with optical axes aligned in perpendicular planes, parallel to horizontal (H) and vertical (V) coordinates of the laboratory. The pump power is low enough to consider SPDC in the perturbative regime (as described in the previous section). We thus neglect the probabilty of generating photon pairs contemporary in the first and in the second crystals. What we have, using a pump polarized at 45°, is half probability of generating in the first crystal and half in the second one. In quantum mechanics terms we write the total state summing the amplitude probability of all possible paths. Finally we obtain a quantum superposition of $|\mathrm{HH}\rangle$ and $|\mathrm{VV}\rangle$ pairs, thus entangled states of the form $\frac{1}{\sqrt{2}}(|\mathrm{HH}\rangle + |\mathrm{VV}\rangle)$.

Using the previous notation with eqs. (2.59), (2.60), calculated respectively with $\Delta k_{\parallel}$ and $\Delta k_{\perp}$ from eq. (2.64), and by using eq. (2.61) we obtain at the output of the two crystals the overall entangled state

$$|\psi\rangle = \frac{1}{\sqrt{2}} \int d\omega_p \, d\omega_s d\theta \, d\theta' A(\omega_p) g(\omega_s, \theta, \theta') f(\omega_p, \omega_s, \theta, \theta') \times \\ \left[|H, \theta, \omega_s\rangle |H, \theta', \omega_p - \omega_s\rangle + e^{\imath \Phi(\omega_p, \omega_s, \theta, \theta')} |V, \theta, \omega_s\rangle |V, \theta', \omega_p - \omega_s\rangle \right]. \tag{2.68}$$

The relative phase term $\Phi(\omega_p, \omega_s, \theta, \theta')$ arises taking into account both the pump and the photon pairs optical paths both other effects such as the pump walk off. In the following section we will describe in details how to derive these terms.

2.3.1 The relative phase term (VV generated in the first crystal)

There are many contribution to the phase Φ in eq. (2.68). We consider for instance the case in which the first crystal generates $|VV\rangle$ photon pairs and the second $|HH\rangle$ pairs as depicted in Fig. (2.9). Consider the generation at the middle of the crystals. Both polarization pairs have three common phase terms due to the optical paths of the extraordinary pump inside the

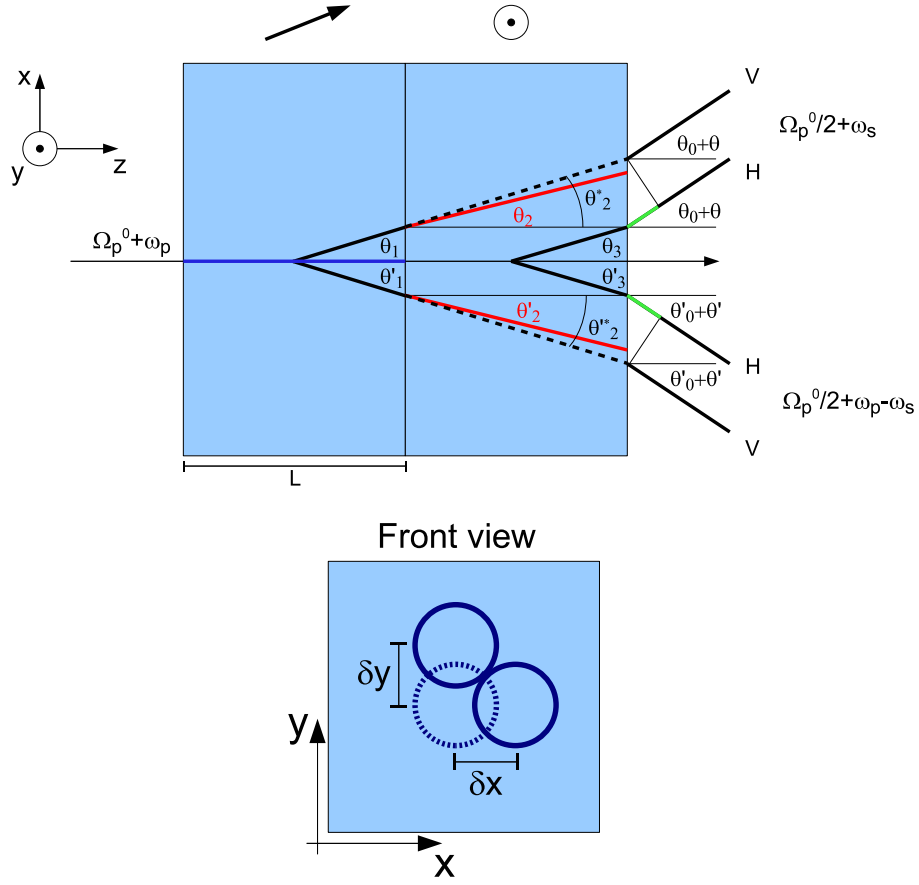

Figure 2.9: *Generating crystal. (top) $|VV\rangle$ photons are generated in the first crystal and travel extraordinary in the second one which have the optical axes in a plane normal to the propagation. Blue, red and green lines represent the optical paths which are important for phase calculation. (bottom) The crystals front view with depicted the walk off induced on the pump beam.*

generating crystals and of the ordinary photons propagation. Respectively we have $k^e(\phi_{PM}, \Omega_p^0+\omega_p)\frac{L}{2}$ for the pump, $k^o(\Omega_p^0/2+\omega_s)\frac{L}{2cos\theta_1}$ for the signal and $k^o(\Omega_p^0/2+\omega_p-\omega_s)\frac{L}{2cos\theta'_1}$ for the idler. These phase terms are not interesting since are common phase terms ($\theta_1=\theta_3$ and $\theta'_1=\theta'_3$) and are not written in the state in eq. (2.68). Photon pairs $|HH\rangle$ have an additional phase term $k^o(\Omega_p^0+\omega_p)L$ due to ordinary propagation of the pump inside the first crystal before it generates pairs in the second one (blue path in fig. (2.9)). On the contrary $|VV\rangle$ pairs must traverse the second crystal accumulating a phase equal to $k^e(\phi_{PM}, \theta_2, \Omega_p^0/2+\omega_s)\frac{L}{cos\theta_2}$ for the signal and $k^e(\phi_{PM}, \theta'_2, \Omega_p^0/2+\omega_p-\omega_s)\frac{L}{cos\theta'_2}$ for the idler (red paths in fig. (2.9)).

Here we have considered negligible the ordinary component (it is the 0.3% of the total photons: see eq. (2.40) and [37]).

Two additional phase components derive from external path difference between vertical and horizontal pairs (green paths in figure (2.9)). These terms can be simply calculated from geometrical consideration once one knows the exact output position. Black dotted lines in the second crystals represent the projection of the paths followed by the Poynting vectors of SPDC photons over the (x, z) plane. The angles θ_2^* and $\theta_2'^*$ have been calculated in eq. (2.43) of section 2.1.3. Thus the additional external phases are $k_{air}(\Omega_p^0/2 + \omega_s)\, L\, tan(\theta_2^*(\theta))\, sin(\theta_0 + \theta)$ for the signal, and $k_{air}(\Omega_p^0/2 + \omega_p - \omega_s)\, L\, tan(|\theta_2'^*(\theta')|)\, sin(|\theta_0' + \theta'|)$ for the idler. In our quasi-collinear situation ($\theta_0 = 3°$) we do the approximation $\theta_2^* \simeq \theta_2$ and $\theta_2'^* \simeq \theta_2'$.

As we have seen above the extraordinary pump propagates in the direction of the Poynting vector and so it suffers of a spatial walk off in the plane containing the O.A. and the the wave vector $\mathbf{k_p}$ (see eq. (2.33)). A spatial walk off δx (δy) inside the first (second) crystal contributes to the phase Φ with a term $\delta x \Delta k_\perp$ for the $|VV\rangle$ pair, and $\delta y \Delta k_{\perp y}$ for the $|HH\rangle$ pair, as expressed in eq. (2.60). The relative phase is thus

$$\begin{aligned}\Phi(\omega_p, \omega_s, \theta, \theta') =& k^e(\phi_{PM}, \theta_2, \omega_s)\frac{L}{cos(\theta_2(\theta))} + \\ &+ k^e(\phi_{PM}, \theta_2', \omega_p - \omega_s)\frac{L}{cos(\theta_2'(\theta'))} + \\ &- k^o(\omega_p)\, L + \\ &- k_{air}(\omega_s)\, L\, tan(\theta_2(\theta))\, sin(\theta_0 + \theta) + \\ &- k_{air}(\omega_p - \omega_s)\, L\, tan(|\theta_2'(\theta')|)\, sin(|\theta_0' + \theta'|) + \\ &+ \delta x\, \Delta k_\perp - \delta y \Delta k_{\perp y}; \end{aligned} \tag{2.69}$$

where $k^e(\phi_{PM}, \theta_2, \omega_s) = \frac{\Omega_p^0/2+\omega_s}{c}\, n_s^e$, $k^e(\phi_{PM}, \theta_2', \omega_p - \omega_s) = \frac{\Omega_p^0/2+\omega_p-\omega_s}{c}\, n_i^e$ and $k^o(\omega_p) = \frac{\Omega_p^0+\omega_p}{c}\, n_p^o$; while $k_{air}(\omega) = \frac{\Omega_p^0/2+\omega}{c}$. The index of refraction $n_s^e = n_s^e(\phi_{PM}, \theta_2(\theta))$ and $n_i^e = n_i^e(\phi_{PM}, \theta_2'(\theta'))$ are calculated from eq. (2.36). The subscripts s, i and p indicate that the refractive indexes are calculated respectively at frequencies $\Omega_p^0/2 + \omega_s$, $\Omega_p^0/2 + \omega_p - \omega_s$, and $\Omega_p^0 + \omega_p$. Furthermore we use as $\Delta k_\perp$ the one expressed in eq. (2.64) while $\Delta k_{\perp y}$ could be taken from the same expression with $\theta_0 = 0$ and with $\theta = \theta_y$ the angular shift in y-direction. The internal angles are:

$$\begin{aligned}\theta_2(\theta) =& asin(\tfrac{sin(\theta_0+\theta)}{n_s^e}) \approx \tfrac{\theta_0+\theta}{n_s^e} \text{ and} \\ \theta_2'(\theta') =& asin(\tfrac{sin(\theta_0'+\theta')}{n_i^e}) \approx \tfrac{\theta_0'+\theta'}{n_i^e}.\end{aligned}$$

Notice that their calculation involves a recursive problem since the refractive indexes depends respectively on the angles θ_2 and θ_2' one want evaluate.

Expansion of the phase term

We expand the expression of Φ using

$$k(\Omega^0+\omega) = k(\Omega^0) + \frac{1}{v_g}\omega + \frac{1}{2}\beta\omega^2 + ... \tag{2.70}$$

$$\frac{1}{cos(\varphi)} = 1 + \tfrac{1}{2}\varphi^2 + ... \tag{2.71}$$

where $\frac{1}{v_g} = \frac{\partial k}{\partial \omega}|_{\omega=\Omega^0}$ and $\beta = \frac{\partial^2 k}{\partial \omega^2}|_{\omega=\Omega^0}$. We obtain after some math

$$\Phi(\omega_p, \omega_s, \theta, \theta') \simeq \Phi_0 + \Delta\tau\omega_p + \alpha\theta - \alpha\theta' + \delta_x[\zeta(\theta+\theta') + \eta\omega_s] + \gamma\,\omega_s^2 \tag{2.72}$$

where

$$\Phi_0 = 2\,k_s^e(\Omega_p^0/2)\,L\left(1+\tfrac{1}{2}\left(\frac{\theta_0}{n_s(\phi_{PM})}\right)^2\right)\cdot\left(1-\tfrac{1}{2}cos^2(\phi_{PM})\,\theta_0^2\,\frac{(n_s^o)^2-(n_s^e)^2}{(n_s^o)^2\,(n_s^e)^2}\right) + -k_p^o(\Omega_p)\,L - \frac{L}{c}\frac{\Omega_p^0\,\theta_0^2}{n_s(\phi_{PM})}; \tag{2.73}$$

$$\Delta\tau = \frac{L}{v_{gPDC}^e}\left(1+\tfrac{1}{2}\left(\frac{\theta_0}{n_s(\phi_{PM})}\right)^2\right) - \frac{L}{v_{gp}^o} - \frac{L}{c}\frac{\theta_0^2}{n_s(\phi_{PM})} - \delta_x\frac{\theta_0}{v_{gPDC}^o\,n_s^o}; \tag{2.74}$$

$$\alpha = -\frac{\Omega_p^0/2}{c}\,n_s(\phi_{PM})\,L\left[\frac{\theta_0}{(n_s(\phi_{PM}))^2} + cos^2(\phi_{PM})\,\theta_0\,\frac{(n_s^o)^2-(n_s^e)^2}{(n_s^o)^2\,(n_s^e)^2}\right]; \tag{2.75}$$

$$\zeta = k_s^o(\Omega_p^0/2)\frac{1}{n_s^o}; \tag{2.76}$$

$$\eta = \frac{2\theta_0}{v_{gPDC}^o\,n_s^o}; \tag{2.77}$$

$$\gamma = \beta_{PDC}^e\,L\left(1+\tfrac{1}{2}\left(\frac{\theta_0}{n_s(\phi_{PM})}\right)^2\right). \tag{2.78}$$

We have used the contracted notation $v_{gPDC}^{o,e} = v_g^{o,e}(\Omega_p^0/2)$, $v_{gp}^o = v_g^o(\Omega_p^0)$, $\beta_{PDC}^e = \beta^e(\Omega_p^0/2)$, $n_s^{e,o} = n^{e,o}(\Omega_p^0/2)$ and $n_s(\phi_{PM})$ the extraordinary index of refraction calculated from eq. (2.27) at signal and idler central frequency $\Omega_p^0/2$. In writing eq. (2.72) we neglect the second order in θ^2 and θ'^2 due to the cosine expansion and the terms in ω_s^2 and $\omega_s\omega_p$.

In our experimental condition, considering a null walk off, this model provides: $\Delta\tau = -453\,fs$, the minus sign means that the HH pairs exit before than the VV; the linear angular term is $\alpha = -0.297\,rad/mrad$: this means that the relative phase profile decrease of $0.297\,rad$ increasing the emission angle of $1\,mrad$ respect to the pump propagation direction. This

is symmetrical on both arms. The walk off effect becomes important when the transverse momentum is not conserved (small pump beam radius) and results in an asimmetric angular slope values between signal and idler and in a linear spectral dependence.

2.3.2 The relative phase term (HH generated in the first crystal)

Consider the opposite situation with $|HH\rangle$ pairs are generated in the first crystal. They travel in the second crystal having the optical axes in the propagation plane as depicted in figure (2.5 (left)). Thus the optical path is calculated in a different way (*i.e.* using eq. (2.49)). In such a case the phase Φ reads

$$\begin{aligned}\Phi(\omega_p,\omega_s,\theta,\theta') = &- k^e(\phi_{PM},\theta_2,\omega_s)\frac{L}{cos(\rho-\theta_2(\theta))}\,cos(\rho)+\\ &-k^e(\phi_{PM},\theta_2',\omega_p-\omega_s)\frac{L}{cos(\rho'+\theta_2'(\theta'))}\,cos(\rho')+\\ &+k^o(\omega_p)\,L+\\ &-k_{air}(\omega_s)\,L\,tan(\rho-\theta_2(\theta))\,sin(\theta_0+\theta)+\\ &+k_{air}(\omega_p-\omega_s)\,L\,tan(|\rho'+\theta_2^{'}(\theta')|)\,sin(|\theta_0'+\theta'|)+\\ &-\delta x\,\Delta k_\perp+\delta y\Delta k_{\perp y};\end{aligned} \tag{2.79}$$

with ρ and ρ' the angles between the wave vectors and the Poynting vectors of the two horizontal photons which travels in the second crystal as extraordinary wave. These angles are calculated with eq. (2.33).

Chapter 3

The experimental setup

In this chapter we will describe the experimental setup we used in our laboratory to generate and manipulate entangled state in polarization and momentum. In the first section (sec. 3.1) we will describe the optical system used in our laboratory. The peculiarity of our source is the large angle and spectrum coupled; in section 3.2 we will describe the coupling system and the methods used to optimize its efficiency. We also describe in sec. 3.3 the alignement procedure for descendants. Then we will explain the working principle of the Spatial Light Modulator in sec. 3.4. In the section 3.5 we will describe the spectrometer we build to analise the SPDC output spectrum since cheap commercial spectrometers does not have intensity resolution. The section 3.6 closes the chapter with a brief description of our home made single photon detectors.

3.1 The optical system

The experimental setup is depicted in fig. (3.1). The pump is a linearly polarized continuous wave, $405\,nm$, $40\,mW$ laser diode (Newport $LQC405-40P$). The output of such a laser suffers of astigmatism (*i.e.* a different divergence over the two axis) and the spatial profile is not gaussian. We thus compensate for beam astigmatism using a couple of cilindrical lenses and then, with a spatial filter, we "clean" the transverse profile of the beam. Hence the laser passes through a telescopic system which prepares the desired beam radius. An half wave plate (HWP) rotates the polarization at 45° in order to pump equally both crystals. A birefringent crystal (or a system of crystals), denoted as $\Delta\tau$ in figure, precompensate for the delay time as we will see in the following chapter. The polarization entanglement source is based on two $1.07 \pm 0.003\,mm$ length, $\beta-$Barium borate (BBO) crystals cut for type-I SPDC stacked back to back with the optical axis aligned in perpendicular planes (horizontal and vertical in the laboratory reference frame), the method proposed in [8] and realized for the first time

by Kwiat et al. in [11]. We can use two different configuration of the crystals depending on which is the plane (H or V) that contain the first crystal optical axes, *i.e.* the first crystal generates $|VV\rangle$ or $|HH\rangle$ photons. The crystals generates photon pairs in a non collinear configuration ($\theta_0 = 3°$). The pump beam is stopped and the SPDC photon pairs passes through a spatial light modulator (SLM) which introduces a polarization and position dependent phase shift. Then two slit select the angular aperture $\Delta\theta$ in the horizontal plane, while two larger irises select the vertical coupling. P and P' in the figure denote the polarization projectors: during alignement and visibility measure they are two polarizers, while for the quantum tomography they are both replaced by a quarter wave plate, an half wave plate and a polarizer. Then two spectral filters (F and F') select the spectral width or simply reduce the background. Then a large coupling system send photons into two multimode fibers (MMF) and then to single photon counting modules. A computer controls the SLM and receives direct and coincidence

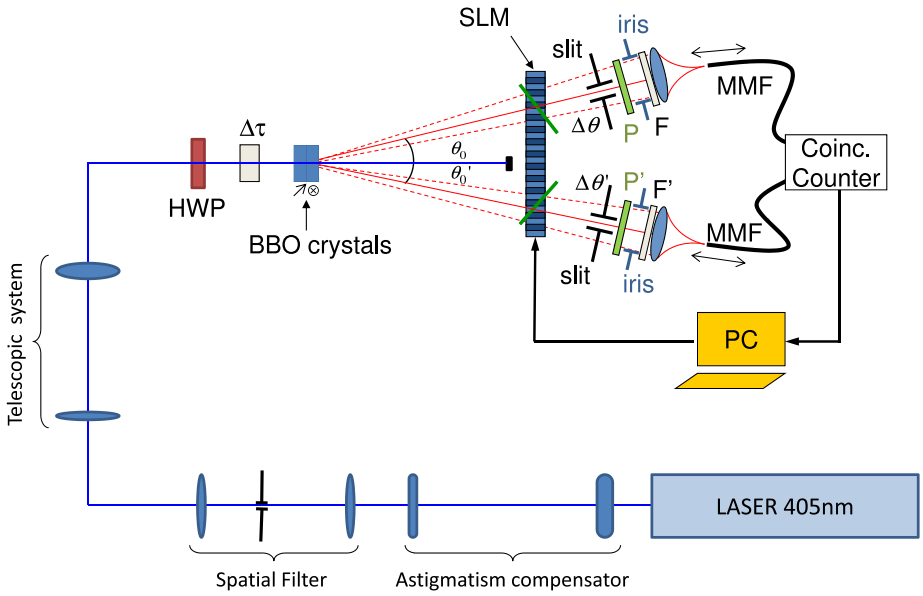

Figure 3.1: *Sketch of the experimental setup.*

3.2 The large coupling system

Our goal was to couple efficiently in an optical fiber photons over a large angular and spectral distribution. In order to maximize the angular collection efficiency we use as fiber couplers two Air-Spaced Doublet Collimators from

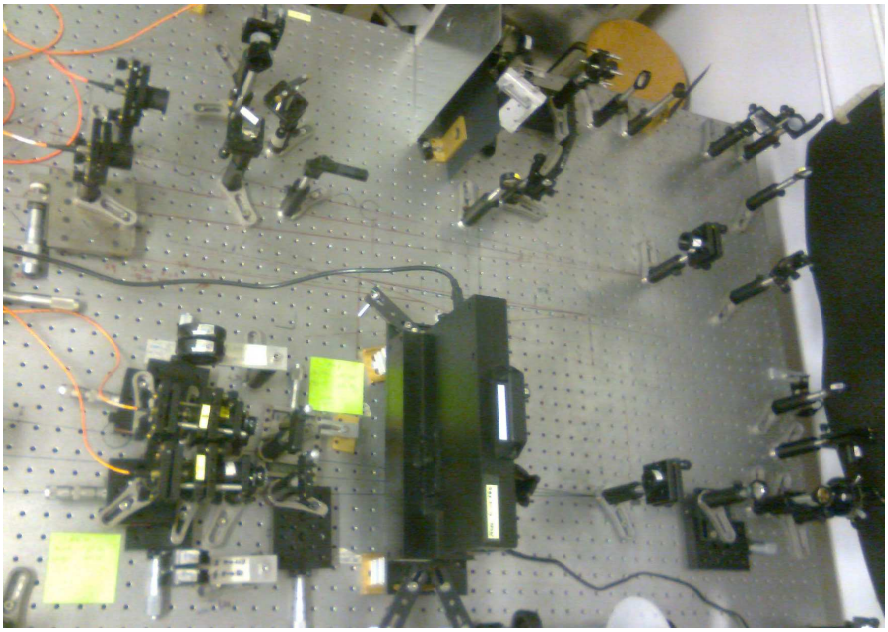

Figure 3.2: *Photo of the experimental setup. The laser source is not shown; it is out of the photo on the left-top side.*

thorlabs (F810-FC-780) having a theoretical $1/e^2$ collimated beam diameter of $7.5\,mm$. In order to maximixe photon coupling into a multimode fiber (core diameter of $62.5\,\mu m$) we use an imaging technique [40, 41, 42]. The coupler lens is at a fixed distance respect to the generating crystals but the fiber is mounted on a linear translation stage, thus we can finely adjust the fiber edge distance from the lens. The purpose is to image on the fiber edge a spot on the crystals which has the same width of the pump beam radius. Experimentally one optimize the coupling looking for the maximum of the detector's counts as a function of the fiber edge position.

The choice of the coupler has been tested with the following measurement. Once we have optimized the coupling with the fiber position, we measure the direct counts as a function of the iris aperture (diameter d). We use a large pump beam waist thus the transverse momentum is conserved and the relation in eq. 2.66 holds, thus we can use $\omega_s = \omega_s(\theta, \theta')$. The measure is reported in fig. (3.3) together with the following fit function

$$F(d, \sigma, M) = \int_{-d/2}^{d/2} d\theta\, I(\theta) T(\theta, \sigma, M); \tag{3.1}$$

where $I(\theta) = \int d\theta' |f(\Omega_p^0, \omega_s(\theta, \theta'), \theta, \theta')|^2$, and $T(\theta, \sigma, M) = e^{-2\left(\frac{\theta}{\sigma}\right)^{2M}}$ is the lens transmittivity function. As it is evident from the plots the Air-Spaced Doublet Collimator couples efficiently also photons at large angles.

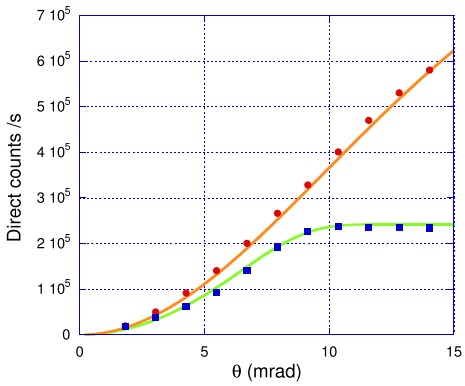

Figure 3.3: *Coupling versus iris diameter. Red circle correspond to the air-spaced doublet collimators (F810-FC-780), blue squares correspond to an acromatic lens. Solid lines are fits with the function in equation (3.1). Orange fit correspond to* $\sigma_{FWHM} = 20\,mrad$*,* $M = 1$ *while green fit correspond to* $\sigma = 5.1\,mrad$*,* $M = 5$*.*

3.2.1 Coupling efficiency versus pump beam radius

We report here the measure of the detected number of photons (per second and per mW of pump power) as a function of the pump beam radius r. We consider the beam transverse profile as gaussian $\sim e^{-2\frac{x^2+y^2}{r^2}}$. Changing the telescopic system we set several quasi collimated pump beam with different radius. The spatial filtering is done with the slits setted at $\Delta\theta = 10\,mrad$. On the left part figure (3.4) shows the result for direct counts; red circles are with a longpass filter (cut-on wavelength of $715\,nm$) while blue squares are with the $10\,nm$ bandpass filter around $810\,nm$. On the right are plotted the coincidences (within $10\,nm$) per second and mW of pump power.

3.3 Alignement procedure

The procedure for the alignement of the apparatus goes as follow:

- Align the pump laser beam;
- Align the optical axes of the crystals in the horizontal and vertical of the laboratory;
- Using a probe laser (at $780\,nm$) align the couplers (F810-FC-780) at the noncollinear angle (3°) following the line on the optical table. We couple the probe laser into a fiber and then into the coupler. In such a way the laser travels in the opposite direction respect to SPDC signal (idler) photons.

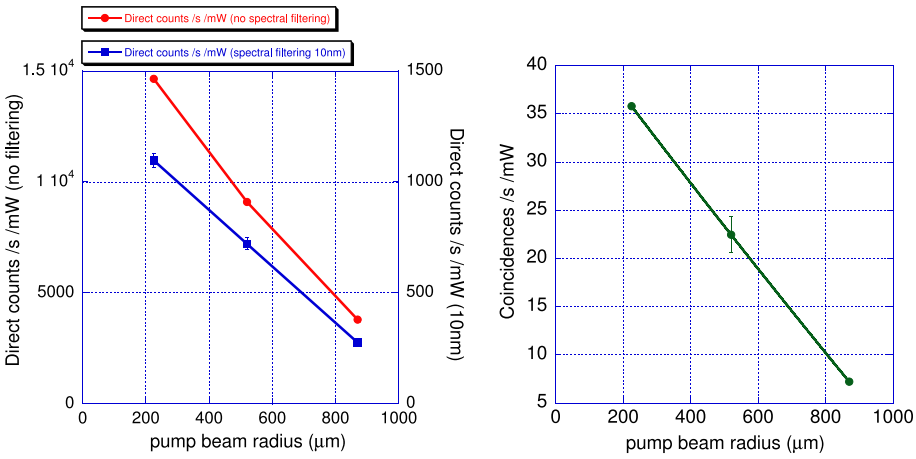

Figure 3.4: *On the left we show the direct counts per second and mW of pump power versus the radius of a quasi-collimated pump beam; red circles are with a longpass filter (cut-on wavelength of* 715 *nm) while blue squares are with the* 10 *nm bandpass filter around* 810 *nm. On the right we plot the coincidences between signal and idler (within* 10 *nm) per second every mW of pump power.*

- Mount the spectral filter and the iris on the coupler and align the polarizer.
- Align the slit taking care that it cuts the beam simmetrically. We image the slit on a camera using the same probe laser to enhance the precision.
- Search for the central pixel, *i.e.* the SLM pixel which is at the centrum of the beam, that is along the path at $\theta_0 = 3°$. By inserting a polarizer before the SLM set at 45° and one after set at 45°, and by using a lens we image the SLM surface on a camera. We set the SLM phase at π on the candidate pixel and at 0 elsewhere. On the camera we see a black line in correspondence of the phase π (see fig. (3.5)).
- Switch off the probe laser and switch on single photon detectors; set the pump laser beam at vertical polarization using the half-wave plate, then set the polarizers transmitting horizontal polarization. Find the optimal phase matching angle tilting the vertical screw on crystals mounting and looking for the maximum counts on both channels.
- Optimize the coupling efficiency with coupler's screw and with the fiber edge position behind the coupler's lens.

- Rotate the pump polarization till horizontal and set the polarizer at verical position. Tilting the horizontal screw of the crystal mounting find the optimal phase matching optical axis angle.
- Set pump polarization and polarizers at 45°. Using the SLM send a constant phase which maximize the coincidences. With the couplers screw optimize direct counts and coincidences.
- Adjust the pump polarization for perfect balancing of HH and VV pairs.
- Set with the SLM the desired compensation function. Set the polarizers at 45° and −45°. Scan a constant phase to find the minimum number of coincidences.
- Set the optimal parameters and measure Visibility. For the optimization procedure repeat this procedure for different compensation functions in order to obtain the highest visibility as possible.

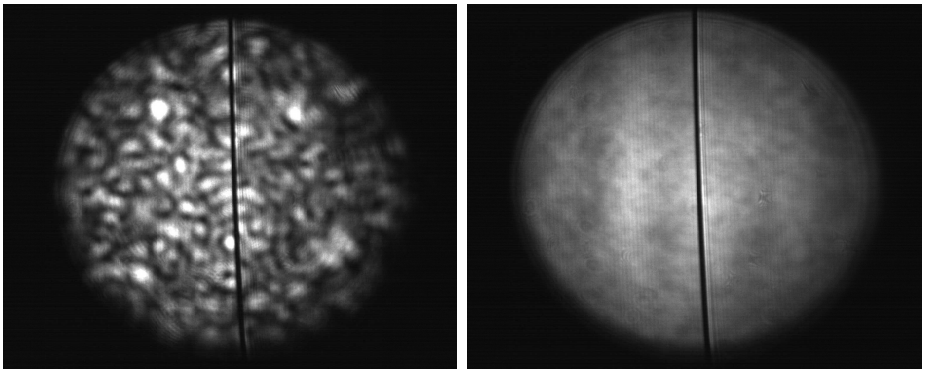

Figure 3.5: *Method for the search of the central pixel. On the left the image of SLM plane; the fiber input is the light diffracted by a polished surface. On the right the same image but using as fiber input the light diffracted by a rotating polished disc. The black line is the SLM pixel.*

3.4 The spatial light modulator

The Spatial Light Modulator (SLM) has a basic role in this work. In this section we will explain its operating principle and the calibration procedure.

Our SLM is a one-dimensional $SLM - S640$ from Jenoptik Optical Systems. Confined by two glasses there is a nematic liquid crystals with the axes in the horizontal plane. The orientation α of this axes respect to the propagation direction, depends on the electric field applied by transparent

electrodes. Vertically polarized light feel an ordinary refractive index while the horizontal polarization see an extraordinary index of refraction dependent on the liquid crystal orientation α. The relative phase between the two polarization introduced by the SLM is thus

$$\psi_{SLM}(\Delta V) = \frac{\omega}{c}\left[n_H(\alpha(\Delta V)) - n_V\right] d; \tag{3.2}$$

where $d = 10\,\mu m$ is the liquid crystal depth, $n_V = n_o$ is the ordinary refractive index of the liquid crystal and

$$\frac{1}{n_H(\alpha(\Delta V))^2} = \frac{sin^2(\alpha(\Delta V))}{n_e^2} + \frac{cos^2(\alpha(\Delta V))}{n_o^2}$$

As depicted in Fig. (3.6) our SLM is one dimensional and is composed by 640 pixels. Each pixel is driven independently, thus we can introduce a position and polarization dependent phase shift. Each pixel is 97 μm width and the distance between two adiacent electrodes is 3 μm. The liquid crystal

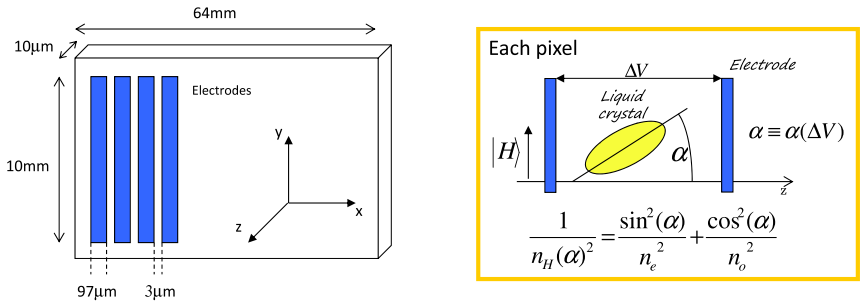

Figure 3.6: *The Spatial Light Modulator. On the left a sketch of the device with the important sizes. On the right the zoom of a single pixel with the representation of an oriented liquid crystal; the orientation α depends on the voltage difference applied by the electrodes, thus the extraordinary index of refraction, seen by horizontal polarization, is voltage dependent too.*

refractive indexes, like other materials, depend on the frequency of light ω. Furthermore non-normal incidence on the SLM surface induce an angular phase dependence since the liquid crystal orientation $\alpha(\Delta V)$ is considered respect to the propagation direction. From this consideration we can rewrite the relative phase as $\psi_{SLM}(\Delta V) = \psi_{SLM}(\Delta V, \omega, \Theta_{in})$. From a PC we send to the SLM an array of 640 integer number in the range $0 \leq n \leq 4000$; each number n correspond to a different ΔV.

3.4.1 Calibration procedure

The calibration of the SLM is done using SPDC light from the same generating crystals and selecting 10 nm using a band pass filter in front of the

couplers and $10\,mrad$ using the slit (see Fig. (3.1)). Since signal and idler incident angles are different we need two distinct calibrations, one for each branch.

Considering a single channel we insert a polarizer set at 135° in front of the SLM and one behind set at 45°. The Spatial Ligth Modulator insert a phase $\psi_{SLM}(n)$, where n is the number sent by PC, remember that each number n correspond to a different voltage ΔV. We generate horizontal polarized photons $|H\rangle$ with one of the two crystals; then the first polarizer transmits the polarization $\frac{1}{\sqrt{2}}(|H\rangle - |V\rangle)$, hence the photons passes through the SLM and the polarization becomes $\frac{1}{\sqrt{2}}(e^{i\psi_{SLM}(n)}|H\rangle - |V\rangle)$. Then the second polarizer projects over $|45°\rangle\langle 45°|$, obtaining at the output the following intensity

$$T(n) = T_0\, sin^2(\tfrac{\psi_{SLM}(n)}{2} + k\pi) \;\text{ with }\; k \in \mathbb{Z}. \tag{3.3}$$

In Figure (3.7) we report a typical calibration measurement; we report the direct counts as a function of the numbers n sent to the SLM. We measure

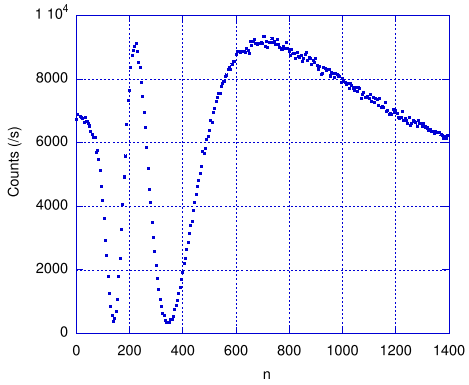

Figure 3.7: *A typical calibration measurement. The counts are proportional to the function (3.3).*

the number of photons for a proper interval of numbers n giving at least a range of 2π; for example for a plot like the one depicted in fig. (3.7) we can select the region between $200 \leq n \leq 900$. Then we invert the relation in eq. (3.3) in the different region, obtaining the calibration function $\psi_{SLM}(n)$ in

the following way

$$\phi_{SLM}(n) = \begin{cases} 2\,arcsin\sqrt{\frac{T(n)}{T(n_1)}} & n_1 \leq n \\ 2\pi - 2\,arcsin\sqrt{\frac{T(n)-T(n_2)}{T(n_1)-T(n_2)}} & n_2 \leq n \leq n_1 \\ 2\pi + 2\,arcsin\sqrt{\frac{T(n)-T(n_2)}{T(n_3)-T(n_2)}} & n_3 \leq n \leq n_2 \\ \vdots & \\ 2\,k\pi + 2\,arcsin\sqrt{\frac{T(n)-T(n_{2k})}{T(n_{2k+1})-T(n_{2k})}} & n_{2k+1} \leq n \leq n_{2k} \end{cases} . \quad (3.4)$$

Using KALEIDAGRAPH Smooth we fit the data $\phi_{SLM}(n)$ in order to solve ordering problems. Then we plot the inverse function $n(\phi_{SLM})$ and we fit another time with 10000 points. In this way we have a file equispaced in the phase ϕ_i. We call i the index of the calibration file $n_i(\phi_i)$. We take as calibration array just the column which contains the numbers n_i. Labview programs driving the SLM uses the array n_i and the searching function $i = a \cdot \phi + b$, with ϕ the phase one want to impose and a, b constants depending on the calibration array and calculated solving the following system:

$$\begin{cases} 0 = a \cdot \phi_0 + b; \\ 9999 = a \cdot \phi_{9999} + b, \end{cases} \quad (3.5)$$

where ϕ_0 and ϕ_{9999} are the phase in the calibration file corresponding to the positions $i = 0, 9999$. These two constants a and b could be added at the end of the calibration array n_i respectively in positions $i = 10001$ and $i = 10002$. We repeat the procedure on the other channel obtaining a different calibration.

3.4.2 Angular and spectral dependence

We want to estimate the effect of different incidence angles and frequencies. Considering a linear angular and spectral dependence we can write the SLM phase shift as

$$\psi_{SLM}(n, \delta\theta, \delta\omega) = \psi_0 + \beta\delta\theta + \gamma\delta\omega. \quad (3.6)$$

We can estimate the angular dependence exploiting the two different calibration. Calling $\psi^{(1)}_{SLM}(n)$ the calibration at $\theta_0 = 3°$ and $\psi^{(2)}_{SLM}(n)$ the calibration on the other branch (at angle $\theta'_0 = -\theta_0$) we have

$$\psi^{(1)}_{SLM}(n) = \psi_0 + \beta\theta_0$$

and

$$\psi^{(2)}_{SLM}(n) = \psi_0 - \beta\theta_0$$

since the spectrum is narrow. Thus we obtain

$$\beta = \frac{\psi^{(1)}_{SLM}(n) - \psi^{(2)}_{SLM}(n)}{2\theta_0} \simeq 7.92. \quad (3.7)$$

Considering $h = 100\,\mu m$ the total pixel width and $D = 310\,mm$ the distance between the SLM and the crystals along θ_0, and calling n_p the pixel number, we have $\delta\theta \simeq \frac{h}{D}\delta n_p$. We thus have $\beta' = \beta\frac{h}{D} \simeq 2.4 \cdot 10^{-3}\, rad/pixel$.

On the other hand, considering the SPDC output central frequency $\Omega_p^0/2$, the signal and idler frequency shift ω_s and $\omega_i = \omega_p - \omega_s$ (ω_p being the pump frequency shift), the SLM phase shift is frequency-dependent and reads

$$\psi_{SLM}^{(1)}(n) = \psi_0 + \gamma\omega_s$$

and

$$\psi_{SLM}^{(2)}(n) = \psi_0 + \gamma\omega_i = \psi_0 + \gamma(\omega_p - \omega_s).$$

The consequence is that if one considers the photons on a single arm, he cannot neglect the SLM spectral effect. While measuring the coincidences between the two channels the phase is a total phase between $|HH\rangle$ and $|VV\rangle$ pairs and one must sum the contribution:

$$\psi_{SLM}^{(1)}(n) + \psi_{SLM}^{(2)}(n) = 2\psi_0 + \gamma\omega_p. \tag{3.8}$$

The net effect is the removal spectral dependence on the broad SPDC spectrum; what remains is only a contribution in the pump frequency shift (*i.e.* γ is an effective delay time). In order to estimate this contribution we take the expression given by the SLM manual

$$\psi_{SLM}^{man}(n, \lambda) = \psi_{SLM}(n) \cdot C(\lambda) \tag{3.9}$$

where $\psi_{SLM}(n)$ is the calibration curve with $\lambda = \lambda_0 = 810\,nm$. The correction function is $C(\lambda) = \frac{\lambda_0}{\lambda}\frac{\Delta n(\lambda)}{\Delta n(\lambda_0)}$ with $\Delta n(\lambda) = n_e(\lambda, n) - n_o(\lambda)$ the optical anisotropy which could be fitted by the function $\Delta n(\lambda) = \frac{\Delta n_\infty\,\lambda}{\sqrt{\lambda^2 - \lambda_r^2}}$ (with $\Delta n_\infty = 0.2002$ and $\lambda_r = 327.44\,nm$). Expanding this expression to the first order in λ and considering $\frac{\partial\omega}{\partial\lambda} = -\frac{2\pi\,c}{\lambda^2}$ we obtain

$$\gamma(n) = \psi_{SLM}(n)\left(-\frac{\lambda_0^2}{2\pi\,c}\right)\frac{\partial C(\lambda)}{\partial\lambda}\Big|_{\lambda_0}. \tag{3.10}$$

We observe that γ depend by the count n because for different count the liquid crystal have a different orientation. In our calibration we consider the range $2\pi \leq \psi_{SLM}(n) \leq 4\pi$, thus $3.2\,fs \leq \gamma \leq 6.5\,fs$ is a small correction to the delay time.

3.5 The spectrometer

In order to measure the large SPDC spectrum we build a spectrometer in the following way. We exploit two gratings ($1200\,lines/mm$) set in a $4-f$ configuration, two lenses ($f = 35\,mm$) and a knife which cut the spectral

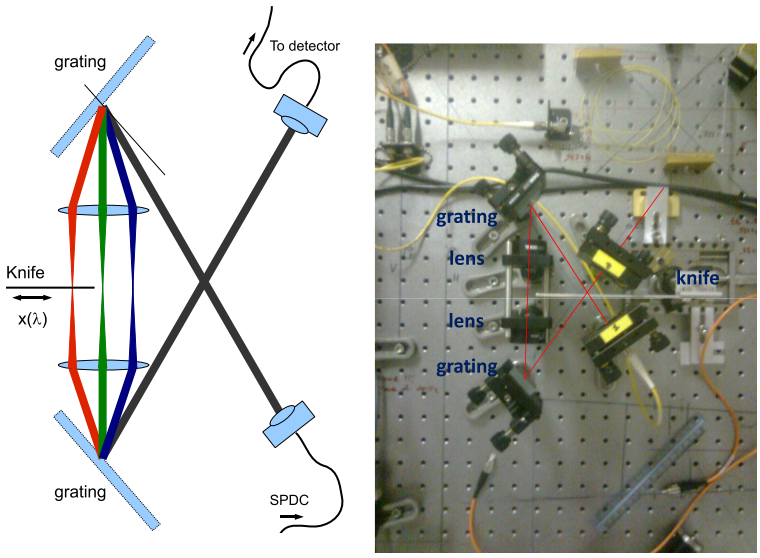

Figure 3.8: *The Spectrometer. (left) Sketch. (right) Photo.*

distribution in the focal plane (see fig. (3.8)). The first grating separates the wavelengths following the law:

$$\theta_d(\delta\lambda) = asin\left(\frac{\lambda_0 + \delta\lambda}{d} - sin(\theta_i)\right), \tag{3.11}$$

where θ_i and θ_d are respectively the incident and diffracted angles measured from the grating normal, $d = 1/1200\,mm$ is the line separation, $\lambda_0 = 810\,nm$ and $\delta\lambda$ is the shift from the central wavelength. At a distance f from the grating we set the first lens, thus the spectral components are then focalized and travels parallel one to each other. The spectral range of this device is limited by the angular acceptance of the lens. In the focal plane of the first lens we have the spectral components well separated. The resolution of the spectrometer is limited by the focalized spot size; in our case the resolution is few nanometers. A second lens set at a distance $2\,f$ from the first collimates the spectral component which then converge on the second grating. The latter gathers the components on the same output beam. Photons are then collected into a multimode fiber by a coupler and sent to a single photon detector. Using a knife in the focal plane with horizontal position x we cut the spectral distribution for an integral measure. Using a lamp and a commercial spectrometer (Thorlabs SPLICCO) we calibrate the knife position obtaining

$$\lambda(x) = 985.69 - 18.11 \cdot x + 0.436 \cdot x^2 - 0.018 \cdot x^3.$$

Then we measure the transmittivity of the spectrometer, useful for renormalization obtaining after a fit

$$T(\lambda) = 0.111 \cdot \exp\left[-2\left(\frac{\lambda - 773.79}{134.85/1.177}\right)^2\right].$$

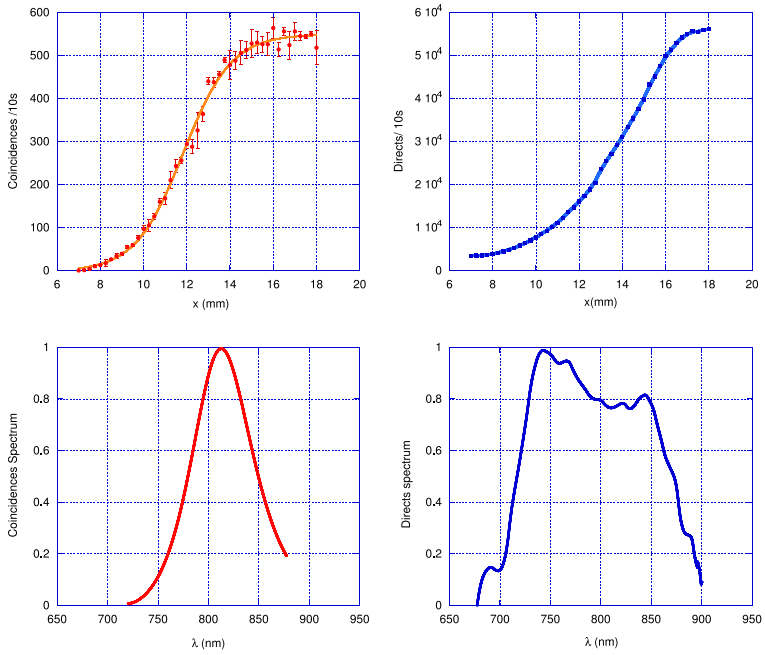

Figure 3.9: *SPDC spectrum. (top) Raw measure of the counts versus the knife position: (left) Coincidences, (right) Direct counts. (bottom) Reconstructed spectral distribution of coincidences (left) and directs (right). The coincidences spectrum have a Full Width at Half Maximum of* 72 *nm (from a Gaussian fit), while directs is large about* 160 *nm. Experimental conditions: slit apertures* $\Delta\theta = 10\,mrad$*, pump beam radius of* 550 μm *and longpass filters on both channels with cut on wavelength of* 715 *nm.*

We call $S(\lambda)$ the spectral distribution one want measure; in the focal plane of the spectrometer it become $S(\lambda(x))$. We measure the integral photon counts

$$N(\lambda(x)) = \int_{-\infty}^{\lambda(x)} d\lambda_s \, S(\lambda_s) \cdot T(\lambda_s) \cdot QE(\lambda_s). \tag{3.12}$$

$QE(\lambda)$ for direct counts is the quantum efficiency of a single detector, while for coincidences it includes the effect of the two detectors and reads $QE(\lambda_s) = QE_1(\lambda_s)QE_2(\lambda_i(\lambda_s))$, where idler wavelength λ_i is linked to the

signal one λ_s by energy conservation see eq. (2.54). A typical measure is reported in figure (3.9) togheter with the fit. Coincidences are well fitted by a Fermi-Dirac function:

$$C(x) = a + \frac{b}{e^{\frac{x-c}{d}} + 1},$$

while the direct counts are fitted with the *KaleidaGraph*'s Smooth function. From the numerical derivative of the fit we obtain the raw spectral distribution. After renormalization with the Spectrometer's transmittivity $T(\lambda)$ and the detector's quantum efficiency $QE(\lambda)$ we obtain the SPDC spectral distribution. The spectral measurements, reported in figure (3.9), are taken with slit apertures $\Delta\theta = 10\,mrad$, pump beam radius of $550\,\mu m$ and longpass filters on both channels with cut on wavelength of $715\,nm$. The coincidences spectrum have a Full Width at Half Maximum of $72\,nm$ (from a Gaussian fit), while directs is large about $160\,nm$. Basically the coincidence spectrum is reduced by the quantum efficiencies of the detectors.

3.6 The detectors

Our home-made detectors are based on silicon avalanche photodiodes operating in Geiger configuration with passive quenching. Light is driven to the photodiodes by the multimode fibers. According to the semi-classical theory of photoemission, when a photon is absorbed, an electron is excited to the conduction band. The p-n junction is polarized inversion with a tension V, and thus a flow of electrons occurs only above the breakdown tension $V > V_{BD} \simeq 200\,V$. The emission probability depends on the difference $\Delta V = V - V_{BD}$. Such an avalanche, caused by the initial acceleration of a single electron, is detected as a macroscopic current. This current is then *quenched* by resistors R_1 and R_2 in series with the photodiode. The pulse lenght is $\tau = (R_1 + R_2)\,C \simeq 1\,\mu s$, where C is the photodiode capacitance. It is a death time for the detectors and thus limits the maximum counting rate to be much smaller than $1/\tau \simeq 10^6$ counts/s. Then the photodiode signal passes through an electronic circuit for pulse shaping exploiting a comparator and a monostable. The former gives a square pulse with a variable length, depending on time windows in which the photodiode pulse remains above a certain voltage threshold. Then a monostable gives equals square pulses of $50\,ns$.

Of course electrons can reach the conduction band also by thermal excitation: such effect is reduced by cooling the detectors up to $-20°C$ with a Peltier cooler. In such a way the so called *dark counts* are limited to $100 - 200$ counts/s using $\Delta V = 4\,V$. The Quantum Efficiency of the detectors thus depends both on the tension above breakdown ΔV, both on the incident wavelength. Our silicon photodiodes have an absorption peak

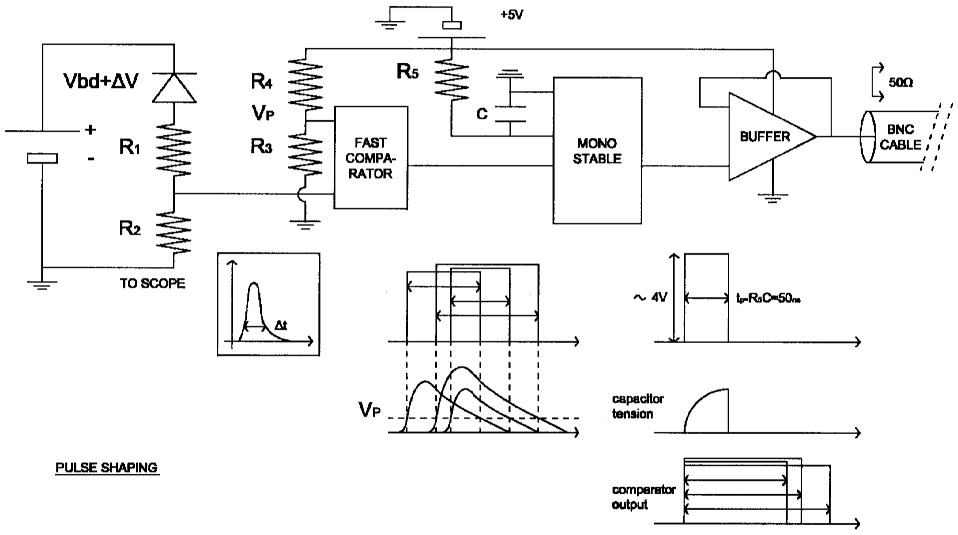

Figure 3.10: *Sketch of the pulse shaping circuit.*

of about 80 % around $\lambda = 800\,nm$. For $\Delta V = 4\,V$ the probability of photoemission is $\sim 17.5\,\%$ (from photodiode's datasheet). The total Quantum Efficiency is about 13.5 % on the peak ($\lambda \simeq 800\,nm$), with a slow decline for shorter wavelength and a sharp drop increasing the wavelength.

Coincidences are measured electronically sending the count pulses to a TAC/SCA: when the first pulse arrives, a linear voltage ramp start to increase (START), while the second pulse passes throught a delay line τ_D. When the delayed count reach the TAC/SCA the ramp is interrupted (STOP); the two counts are said to be contemporary if the STOP is detected at time τ^{TAC} within a temporal window $\Delta\tau^{TAC}$. The last two parameters are adjustable, in particular $\Delta\tau^{TAC}$ could be reduced till $1\,ns$, thus drastically reducing the accidental coincidence counts $C_{Acc} = N_1\,N_2\,\Delta\tau^{TAC}$, with N_1, N_2 the direct counts on the two detectors. The other parameter τ^{TAC} is set equal to τ_D maximizing the coincidences rate within the window $\Delta\tau^{TAC}$. Actually, even if the electronics of the detectors is the same, the shape of the photodiode pulse changes at every count. This results in different delays between the photodiode and the monostable signal, since the photodiode rises exceed the comparator threshold at different instants. Hence "true" coincidence counts are also reduced by a narrow contemporary window, due to the detectors' *jitter*. The jitter has been measured to be $5\,ns$ on the signal detector and $9.5\,ns$ on the idler one. About half of coincidences are lost setting $\Delta\tau^{TAC}$ of the same order of the jitter. As a trade-off between limiting accidental counts and detecting efficiently "true" coincidences we therefore set a contemporary windows $\Delta\tau^{TAC} = 50\,ns$.

Chapter 4

Entanglement measures

In this chapter we will explain the measures we usually made on the entangled state. In order to quantify the state purity and the concurrence we measure the state visibility as explained in section 4.1. Then, in sec. 4.2, we report an example of quantum tomographic measurement with the reconstruction of the density matrix and in sec. 4.3 I suggest a way to measure the concurrence in our particular case. In sec. 4.4, we report the measure of Bell parameter S which demonstrates the presence of nonlocality when it is larger than 2. Finally in sec. 4.5 we report the experimental measure of the angular correlation between signal and idler for different spectrum coupled.

4.1 Visibility

We want to quantify the amount of polarization entanglement. We consider a generic state

$$|\psi\rangle = \frac{1}{\sqrt{2}} \int d\xi F(\xi) \left(|HH\rangle + e^{\imath\Phi(\xi)} |VV\rangle \right) \tag{4.1}$$

with ξ a certain variable with amplitude probability distribution $F(\xi)$ (even and normalized function $\int d\xi |F(\xi)|^2 = 1$). The phase $\Phi(\xi) = \Phi_0 + \alpha\xi + \frac{1}{2}\beta\xi^2 + \dots$ is a generic phase function expanded in a Taylor series with constant term Φ_0 set to 0. Using the two polarizers (see Fig. (3.1)) we project signal photons over $|45^\circ\rangle = \frac{1}{\sqrt{2}}(|H\rangle + |V\rangle)$ and idler photons over a generic polarization at angle $|\varphi\rangle = cos(\varphi)|H\rangle + sin(\varphi)|V\rangle$. The probability of coincidence counting reads

$$\begin{aligned} P(\varphi) =& |\langle 45^\circ, \varphi|\psi\rangle|^2 = \\ =& \frac{1}{4} \int d\xi |F(\xi)|^2 (1 + sin(2\varphi)\, cos(\Phi(\xi))) \\ =& \frac{1}{4} \left(1 + sin(2\varphi) \cdot \int d\xi |F(\xi)|^2 cos(\Phi(\xi)) \right). \end{aligned} \tag{4.2}$$

Such a function has a maximum for $\varphi_M = 45°$ and a minimum for $\varphi_m = -45°$ (see fig. (4.1)). The $cos(\Phi(\xi))$ term reduces the maximum value and lifts the minimum, furthermore the effect of different $\Phi(\xi)$ is averaged by the integral, giving a global reduction of the relative amplitude. The Visibility

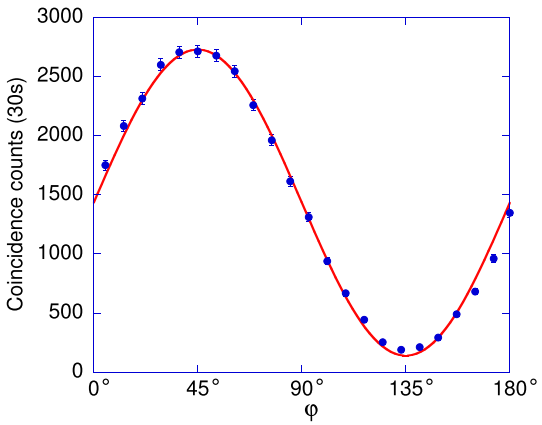

Figure 4.1: *Coincidence counts with signal polarizer set at* 45° *and scanning idler polarizer. We can see that maximum and minimum occurs respectively at* 45° *and* 135° $= -45°$. *The red line is the fit with the function in eq. (4.2). The Visibility of the entangled state is always calculated using the maximum and the minimum of this plot.*

reads

$$Vis = \frac{P(45°) - P(-45°)}{P(45°) + P(-45°)} = \int d\xi |F(\xi)|^2 \, cos(\Phi(\xi)) = \mathcal{R}e[\varepsilon], \qquad (4.3)$$

where $\varepsilon = \int d\xi |F(\xi)|^2 \, e^{\imath\Phi(\xi)}$. We put in evidence that only in the case with $\Phi_0 = 0$ and odd phase function $\Phi(\xi)$, the visibility is a good measure of the amount of polarization entanglement, since $\int d\xi |F(\xi)|^2 \, sin(\Phi(\xi)) = 0$ and thus the visibility equals the concurrence $\mathcal{C} = |\int d\xi |F(\xi)|^2 \, e^{\imath\,\Phi(\xi)}|$ (see section 1.3). Nevertheless this situation often occur and we refer to visibility as the state purity and as good polarization entanglement measure.

To report our state into the situation of null constant term Φ_0 we use the Spatial light Modulator. The total phase is thus $\Phi(\xi) - \phi_{SLM}$ with $\phi_{SLM} = b_1 + b_2$ where b_1 and b_2 are constant phases introduced by the SLM respectively on signal and idler channel. We act as follow: setting the polarizers in the configuration for a minimum $(45°, -45°)$ and keeping fixed the constant phase term on one channel (say $b_2 = 0$), we measure the coincidences for different constant phase term b_1 on the other arm. As one can see from fig. (4.2) we obtain a sinusoidal function. Notice that the procedure gives the same result scanning b_2 instead of b_1 (setting $b_1 = 0$). The minimum occurs for $\phi_{SLM} = b_1 + b_2 = \Phi_0$.

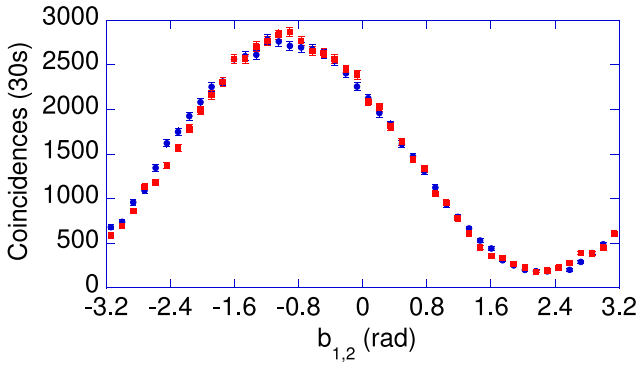

Figure 4.2: *Coincidence counts with polarizers set at* $45°$, $-45°$ *for different value of the constant phase* b_1 *(with* $b_2 = 0$ *(blue circles)) or* b_2 *(with* $b_1 = 0$ *(red squares)).*

4.2 Tomography of the state

The most complete analysis of the state is the two-qubit tomography. It consists in the reconstruction of the global density matrix and requires 16 different projectors as explained in sec. 1.4. We insert on both channel a quarter-wave plate, an half-wave plate and a polarizer which transmit vertical polarized photons. Setting wave plate angles in the configurations expressed in table 1.1 we measure the coincidences between signal and idler.

We report an example of the set of 16 measurements (coincidences over $60\,s$): $\{n_1 = 2020; n_2 = 71; n_3 = 2050; n_4 = 68; n_5 = 1000; n_6 = 1030; n_7 = 970; n_8 = 1000; n_9 = 1120; n_{10} = 1730; n_{11} = 1100; n_{12} = 1030; n_{13} = 1000; n_{14} = 975; n_{15} = 1025; n_{16} = 1705\}$. Then following the procedure explained in sec. 1.4.2 a Maximum likelihood reconstruction with a numeric optimization procedure is carried out. The result is the physical density matrix $\rho = |\psi\rangle\langle\psi|$ of the generated state. In figure (4.3) we report the result for the previous set of measurements. It is a typical representation of a density matrix; on the right we report the Real part while on the left the Imaginary part. From the knowledge of the density matrix one can calculate some important quantity. For example the Concurrence defined in sec. 1.3 for the previous example is $\mathcal{C} = 0.70$ while the visibility, measured as explained in sec. (4.1) reads $Vis = 0.696 \pm 0.013$.

4.3 Concurrence measurement

We consider a situation in which the relative phase $\Phi(\xi)$ is an even function. As we have seen in sec. 4.1, in such a situation one cannot give the visibility as a good estimation of the entanglement. A possible correct estimator is the

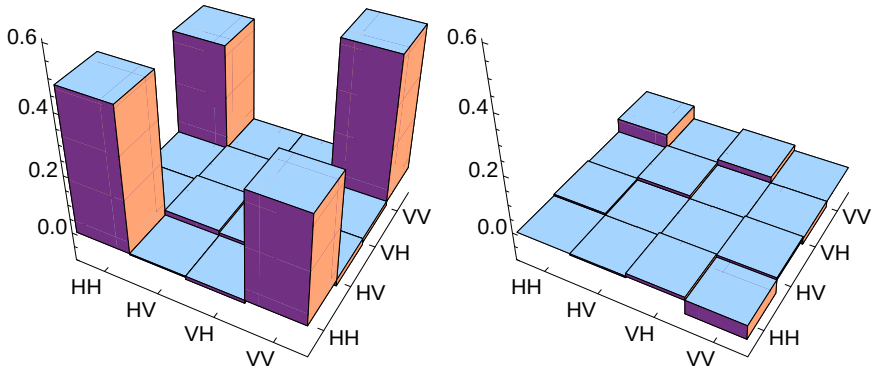

Figure 4.3: *Example of a Tomographic reconstruction of a polarization two-qubit density matrix. On the right the Real part and on the left the Imaginary part.*

Concurrence [31]. Definition has been given in eq. (1.10), here we address the problem of its measure.

In the general case concurrence estimation requires the knowledge of the whole density matrix. In some cases its calculation is simplified. Here we consider states like the Bell ones

$$\begin{aligned} |\Phi\rangle =& \frac{1}{\sqrt{2}} \int d\xi F(\xi) \left(|HH\rangle + e^{\imath\Phi(\xi)} |VV\rangle \right); \\ |\Psi\rangle =& \frac{1}{\sqrt{2}} \int d\xi F(\xi) \left(|HV\rangle + e^{\imath\Phi(\xi)} |VH\rangle \right). \end{aligned} \tag{4.4}$$

Considering $\varepsilon = \int d\xi |F(\xi)|^2 \, e^{\imath\Phi(\xi)}$, in both these cases the concurrence is $\mathcal{C} = |\varepsilon|$. The method to measure the real part $\mathcal{R}e[\varepsilon]$ has been reported in the section 4.1 and it is valid for all the state which can be written as in eqs. (4.4). I suggest the following procedure to measure the Imaginary part:

- Insert on signal path a quarter-wave plate QWP set with the fast axis at angle $q = 90°$ respect to the vertical of the laboratory (see the inset in fig. (1.1) and equation (1.14));
- Then we measure coincidences with polarizers at $45°, 45°$ and $45°, -45°$ and we measure the Visibility as defined in sec. 4.1.
- In such a case the visibility equals the imaginary part of the out of diagonal element:

$$Vis_Q = \int d\xi |F(\xi)|^2 \, sin(\Phi(\xi)) = \mathcal{I}m[\varepsilon]. \tag{4.5}$$

Then Concurrence is thus

$$\mathcal{C} = \sqrt{\mathcal{R}e^2[\varepsilon] + \mathcal{I}m^2[\varepsilon]} = \sqrt{Vis^2 + Vis_Q^2},$$

where Vis is the visibility measured without the insertion of the QWP.

4.4 Measurement of the Bell's parameter in the CHSH form

In sec. 1.5 we have explained the theory behind the measurement of the Bell's parameter and its role in the discrimination between a local and real theory and quantum mechanics. We have seen that quantum mechanics predicts a value larger than 2 for certain choice of the polarizer's angle θ, while a real and local theory based on hidden variable limits its value to $|S| \leq 2$. We have seen (see Fig. (1.2)) that the maximum expected by quantum mechanics in the function $S(\theta)$ depends on the state purity. Thus, in order to measure the highest violation as possible of the limit 2, we have to measure first of all the state purity, and then to choose the angle θ for which the function $S(\theta)$, evaluated from a numerical prediction, has a maximum. Then we measure the functions P and E in order to have an experimental value of the Bell parameter S using the definitions in eq. (1.33) and eq. (1.35), which we report here for convenience:

$$E(\alpha, \beta) = P(\alpha, \beta) + P(\alpha_\perp, \beta_\perp) - P(\alpha_\perp, \beta) - P(\alpha, \beta_\perp),\ \forall\, \alpha, \beta; \tag{4.6}$$

$$S = E(a, b) - E(a, b') + E(a', b) + E(a', b'),\ with\, a = 0,\ b = \theta,\ a' = 2\theta,\ b' = 3\theta. \tag{4.7}$$

From the experimental point of view, we obtain $P(\alpha, \beta)$ from 4 coincidence measurements; in effect it reads

$$P(\alpha, \beta) = \frac{N_c(\alpha, \beta)}{N_c(\alpha, \beta) + N_c(\alpha_\perp, \beta) + N_c(\alpha, \beta_\perp) + N_c(\alpha_\perp, \beta_\perp)}, \tag{4.8}$$

where $N_c(\alpha, \beta)$ is the coincidences with signal and idler polarizers set respectively at angles α and β. These are the same 4 measurements required to calculate $E(\alpha, \beta)$. Since S is composed by 4 different E values we need 16 coincidence measurements. In the table (4.1) we report the sixteen experimental measurement required. For example, we have an entangled state with visibility (purity) equal to 88.5 ± 1.2. The function $S(\theta)$ has a maximum for $\theta = 23°$ and the theoretical value is $S(23°) \simeq 2.668$. We measure coincidences over $90\,s$ for the sixteen projectors given in table 4.1 and we obtain the following set of measurement $\{N_1 = 7195;\ N_2 = 1294;\ N_3 = 1141;\ N_4 = 7200;\ N_5 = 1333;\ N_6 = 7078;\ N_7 = 7135;\ N_8 = 1089;\ N_9 = 6765;\ N_{10} = 1733;\ N_{11} = 1817;\ N_{12} = 6787;\ N_{13} = 7026;\ N_{14} = 1478;\ N_{15} = 1459;\ N_{16} = 6986\}$. The error for the count N_i is the square

coinc	*signal polarizer*	*idler polarizer*	P
N_1	a	b	$P(a,b)$
N_2	a	$b_\perp$	$P(a,b_\perp)$
N_3	$a_\perp$	b	$P(a_\perp,b)$
N_4	$a_\perp$	$b_\perp$	$P(a_\perp,b_\perp)$
N_5	a	b'	$P(a,b')$
N_6	a	$b'_\perp$	$P(a,b'_\perp)$
N_7	$a_\perp$	b'	$P(a_\perp,b')$
N_8	$a_\perp$	$b'_\perp$	$P(a_\perp,b'_\perp)$
N_9	a'	b	$P(a',b)$
N_{10}	a'	$b_\perp$	$P(a',b_\perp)$
N_{11}	$a'_\perp$	b	$P(a'_\perp,b)$
N_{12}	$a'_\perp$	$b_\perp$	$P(a'_\perp,b_\perp)$
N_{13}	a'	b'	$P(a',b')$
N_{14}	a'	$b'_\perp$	$P(a',b'_\perp)$
N_{15}	$a'_\perp$	b'	$P(a'_\perp,b')$
N_{16}	$a'_\perp$	$b'_\perp$	$P(a'_\perp,b'_\perp)$

Table 4.1: *Summary of the sixteen projective measurements for the measurement of the Bell parameter S. Signal and idler polarizers angles are $a = 0, b = \theta, a' = 2\theta, b' = 3\theta$. The angle θ is the one which maximize the function $S(\theta)$ given the state purity p. Using N_1, N_2, N_3, N_4 we evaluate $E(a,b)$; with N_5, N_6, N_7, N_8 we evaluate $E(a,b')$; while using N_9, N_{10}, N_{11}, N_{12} we evaluate $E(a',b)$ and with N_{13}, N_{14}, N_{15}, N_{16} we evaluate $E(a',b')$.*

root of the number $\sqrt{N_i}$. With these coincidence counts and from error propagation we obtain $S_{exp} = 2.658 \pm 0.011$. The value violate the limit of 2 for $57\,\sigma$. This prove that a local and real theory cannot explain the phenomena of entanglement.

4.5 Angular correlation

The entanglement in the momentum could be visualized by the angular correlation between signal and idler. The theory and the simulation are reported in sec. 2.2.1. As sketched in fig. (4.4) we measure coincidences for different slits positions both on signal and idler. We place two slits of aperture Δ, along the downconversion arms and we measure

$$C(\theta_s,\theta_i) = \int_{\theta_i-\frac{\Delta}{2}}^{\theta_i+\frac{\Delta}{2}} d\theta' \int_{\theta_s-\frac{\Delta}{2}}^{\theta_s+\frac{\Delta}{2}} d\theta \int d\omega_p\, d\omega_s \left| f(\omega_p,\omega_s,\theta,\theta') g(\omega_s,\theta,\theta') \right|^2 F(\omega_p,\omega_s)\ , \tag{4.9}$$

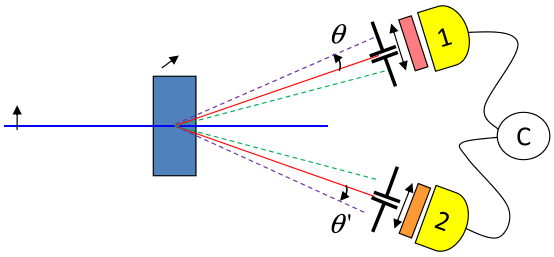

Figure 4.4: *Sketch of the apparatus for angular correlation measurement. We measure coincidences for different slits positions both on signal and idler. In front of the couplers there are spectral filters: on channel* 1 *it is a long pass filter (cut-on wavelength* 715 *nm), while on channel* 2 *we insert at will a bandpass filter centered around* 810 *nm with a band* 10 *nm or a similar long pass filter as channel* 1*.*

with $F(\omega_p, \omega_s) = F_s(\omega_s)F_i(\omega_p - \omega_s)$. The phase matching (central) angles correspond to $\theta_s, \theta_i = 0$. Coincidences are taken over an acquisition time of 6s within a coincidence time window of 50ns. Fig. (4.5) reports the results for the coincidence C obtained by coupling a narrow ($10\,nm$) or rather large ($60\,nm$) spectrum and using large pump beam radius ($550\,\mu m$), thus with transverse momentum conserved.

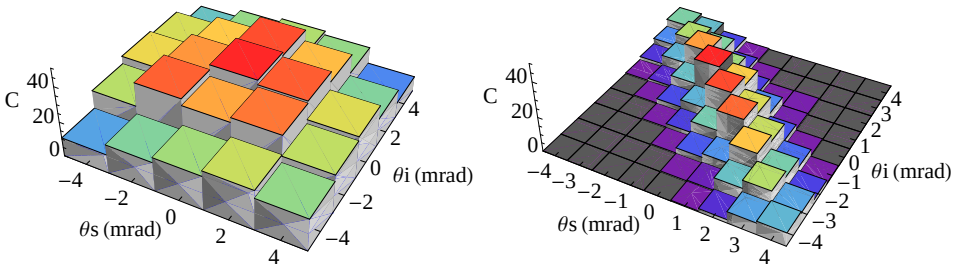

Figure 4.5: *Coincidences as a function of signal and idler angular displacement θ_s and θ_i from the central angles. (Left panel) Completely uncorrelated regime in the case of very large spectral distribution ($\sim$ 60 nm, the angular resolution is* 2 *mrad); (right panel) Angular correlation regime, we select* 10 *nm of the overall SPDC spectral distribution (angular resolution* 1 *mrad).*

Let us devote some attention to the angular function $f(\theta, \theta')$ in the uncorrelated case (large spectrum coupled), which will be important for the following discussion. We assume that it has the factorized form $G(\theta)G'(\theta')$.

The corresponding coincidence counts distribution $C = |f_{\rm exp}(\theta, \theta')|^2$, reported in the left panel of fig. (4.5), has been compared with the one computed as

$$\frac{\mid f_{\rm exp}(\theta, 0) f_{\rm exp}(0, \theta') \mid^2}{\mid f_{\rm exp}(0, 0) \mid^2},$$

and an excellent agreement was found, also corroborated by a significant χ^2 test ($P_{\chi^2 > \chi^2_0} \simeq 0.9$). Upon inspecting the distribution one sees that the angular distributions $G(\theta)$, $G'(\theta')$ are peaked around the central values $\theta = \theta' = 0$ value with a width of 8.6 mrad.

Chapter 5

Purification of entanglement

In this chapter we will describe in details the different effects which causes a loss of purity of the polarization entangled state [25], and some technique we used to compensate them. In sec. 5.1 we will explain the decoherence due to the delay time in the relative phase term and its link with the power spectrum of the pump beam. Then in section 5.2 we will explain the compensation of the angular phase term, linear both in signal and idler angles, using the SLM in a programmable way. Such procedure has been published on Applied Physics Letters [26]. In sec. 5.3 we will describe the decoherence due to the large spectrum coupled. In type-I SPDC this contribution is just at second order since signal and idler have the same group velocities. We will discuss the possibility of partial compensation using angular degrees of freedom. In section 5.4 we will describe a method allowing the study of the fourier transform of the pump spatial profile (g function) using the entanglement purity and the SLM.

5.1 Power spectrum and Delay time

The total polarization entangled state we generate by type-I SPDC in the two crystal geometry was written in eq. (2.68). In this section we will analyse just the effect of pump frequency $\Omega_p^0 + \omega_p$. The important contribution in ω_p comes from the pump spectrum; we have tested that the contribution of the function f is negligible. We consider the situation in which the first crystal have the optical axis in the horizontal plane, thus it generates VV photon pairs. Considering just this variable the state become:

$$|\psi\rangle = \frac{1}{\sqrt{2}} \int d\omega_p A(\omega_p) \left[|H\rangle|H\rangle + e^{\imath \Delta\tau\, \omega_p} |V\rangle|V\rangle \right], \tag{5.1}$$

where $A(\omega_p)$ is the pump field amplitude and the phase term in ω_p comes from the expansion (see eq. (2.72)). $\Delta\tau = 453\, fs$ is the delay time between $|HH\rangle$ and $|VV\rangle$ pairs at the crystal output. Its calculation is written in eq.

(2.74) and it has been calculated numerically. The visibility reads

$$Vis(\Delta\tau) = \mathcal{R}e\left[\int d\omega_p |A(\omega_p)|^2 \, e^{i\Delta\tau\,\omega_p}\right]; \tag{5.2}$$

as one can see it is the real part of the Fourier transform of the pump power spectrum.

We have thus measured the power spectrum of the laser. The result, together with its numerical fourier transform (visibility) is reported in fig. (5.1). From the Fourier transform of the pump power spectrum we obtain

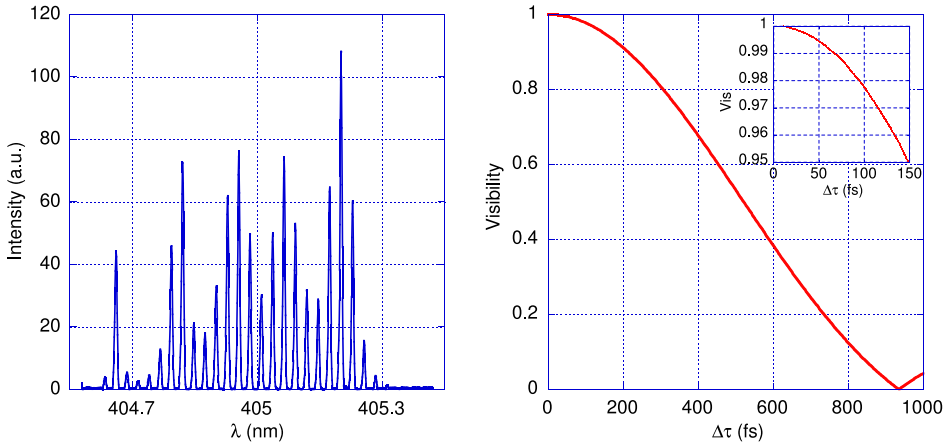

Figure 5.1: *On the right the power spectrum of the pump laser. On the left its Fourier transform, which correspond to the Visibility of the entangled state written in eq. (5.2). The inset is a zoom of the Visibility for short delay time; we can see that about* $50\,fs$ *gives a visibility reduction of* 0.005 *which could be considered negligible.*

also an information about the temporal coherence of our laser source. If we take the $1/e^2$ temporal value of such curve we obtain that the coherence time is $\tau_c \simeq 790\,fs$. Thus the delay time $\Delta\tau$ of the entangled source is comparable to the coherence time of the pump. The consequence is that the entangled state visibility is partially reduced.

5.1.1 Delay time compensation

We now address the problem of entanglement purification. Since visibility is the Fourier transform of the pump power spectrum, we could use a laser beam with larger coherence time (for example a laser with a single temporal mode) to remove this contribution to decoherence. A simpler idea is to precompensate the delay time on the pump path inserting a proper birefringent crystal which introduces the opposite delay [43, 44, 45, 46, 47, 48], as

calculated in the following formula

$$\Delta t = L \cdot \left(\frac{1}{v_g^e(\Omega_p^0, \phi_{OA})} - \frac{1}{v_g^o(\Omega_p^0)} \right), \tag{5.3}$$

where L is the crystal length while v_g^e and v_g^o are respectively the extraordinary and ordinary group velocities within the birefringent crystal; ϕ_{OA} is the angle between the optical axis of the crystal and the propagation direction. Fig. (5.2) report the visibility measure for different delay time obtained using different crystal length and optical axis orientation (ϕ_{OA}). The red curve is the theoretical prediction evaluated from eq. (5.2) substituting $\Delta\tau$ with $\Delta\tau - \Delta t$. These measurement has been taken with the following pa-

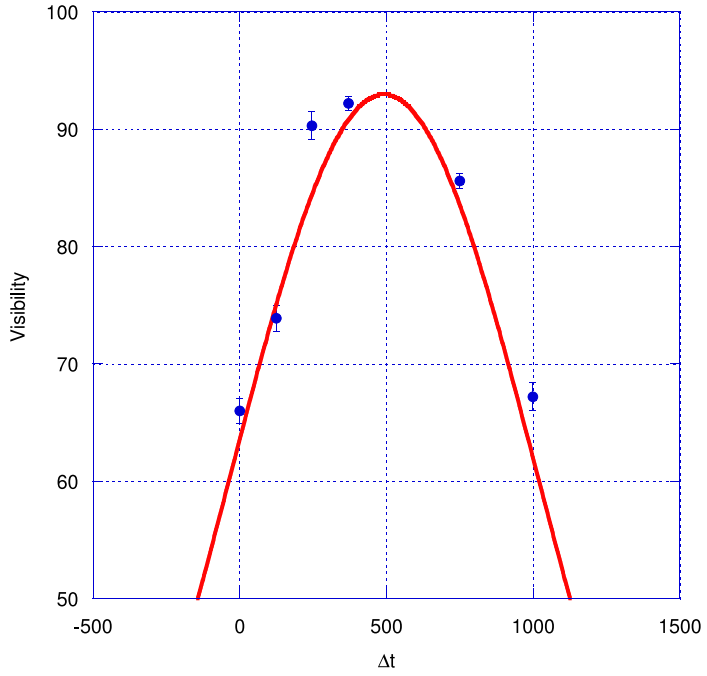

Figure 5.2: *Visibility for different delay time compensation Δt obtained with birefringent crystals set on the pump path (see Fig. (3.1)). The red curve is the theoretical prediction evaluated from eq. (5.2) substituting $\Delta\tau$ with $\Delta\tau - \Delta t$.*

rameter of the experimental setup (see fig. 3.1): the pump beam waist is set at $550\mu m$, the slits width are $\Delta\theta = \Delta\theta' = 8\,mrad$; the iris aperture which limits the vertical coupling are set at $12\,mrad$; the spectral filters F and F' are longpass filters with cut on wavelength $780\,nm$. Furthermore the angular phase is compensated to the first order by the SLM as explained in the following section.

The optimal compensation for the delay time has been found using a $3\,mm$ type-I BBO crystal with optical axis in the vertical plane. It introduces a delay of $397\,fs$. In the following the delay time is considered always compensated. This crystal introduces a walk off in the vertical direction of $203\,\mu m$.

5.2 Programmable purification of angular phase term

In this section we will describe the purification procedure using the Spatial Light Modulator. The advantages of this operation is twofold; on the one hand this allows us to dramatically decrease the spectral and angular filtering of downconverted photons, which is the method generally used to prevent the degradation of the purity. Moreover the SLM may be externally controlled, via software, and this makes our method more easily adjustable for the different implementations, compared to purification schemes that involve the use of suitably prepared crystals along the path of the downconverted photons [25].

We take the expansion of the phase term in eq. (2.72), with the delay time $\Delta\tau$ removed as explained above (sec. 5.1.1) and we neglect for instance the walk off contribution using a configuration with large pump beam waist ($550\,\mu m$). This configuration simplify the treatment since the function $g(\omega_s, \theta, \theta') \approx \delta(\omega_s, \theta, \theta')$ and the three parameters are no more independent but linked by the relation $\theta' = -\theta + \gamma\omega_s$. The consequence is that we remove one of them from the analysis. For the sake of simplicity we remove ω_s. Furthermore we don't consider the second order spectral effect because it will be analysed in a following section. The phase term we consider is thus

$$\Phi(\theta, \theta') = \Phi_0 + \alpha\theta - \alpha\theta'. \tag{5.4}$$

Using the one dimensional Spatial Light Modulator (SLM) we insert the linear phase $\Phi_{SLM}(\theta, \theta') = \alpha_1\theta - \alpha_2\theta' + \beta$ acting on the horizontals photons, β is a constant phase. The state after the SLM is thus

$$|\psi\rangle = \frac{1}{\sqrt{2}} \int d\theta \int d\theta' f(\theta, \theta') \left[|H\rangle|H\rangle + e^{\imath[\Phi_0 + \alpha\theta - \alpha\theta' - \Phi_{SLM}(\theta,\theta')]} |V\rangle|V\rangle \right], \tag{5.5}$$

and the Visibility reads

$$Vis(\alpha_1, \alpha_2) = \mathcal{R}e \left[\int_{\Delta\theta} d\theta \int_{\Delta\theta'} d\theta' |f(\theta, \theta')|^2 \, e^{\imath[(\alpha - \alpha_1)\theta + (\alpha_2 - \alpha)\theta' + \Phi_0 - \beta]} \right], \tag{5.6}$$

where $\Delta\theta$ and $\Delta\theta'$ are the slit apertures. We rewrite the Φ_{SLM} as a function of the SLM pixel number n; it reads

$$\Phi_{SLM}(n) = a_1 \cdot (n - n1) + b_1 + a_2 \cdot (n - n2) + b_2, \tag{5.7}$$

where n_1 and n_2 are respectively the pixels on corresponding the center of signal and idler angular distributions and b_1, b_2 are constant phases on the two channels. The constant phase could be introduced only on one of the two channels at will. The SLM slope parameters are $a_i = \frac{h}{D}\alpha_i$ $(i = 1, 2)$, with $h = 0.1\,mm$ the pixel total width and $D = 310\,mm$ the SLM distance from the crystals. The optimal slope is predicted from eq. (2.75) and is $a_2 = -a_1 = a = 0.096\,rad/pixel$.

We measure the state visibility for different slopes $a_2 = -a_1 = a$. The sum $b_1 + b_2 = b$ is set equal to Φ_0. It is found by measuring coincidence with polarizers set at 45° and −45° and searching the minimum counts by scanning different b_i values ($i = 1\,or\,2$) with the other set at a fixed value. In the fig. 5.3 we report the result together with a theoretical prediction V_{th}

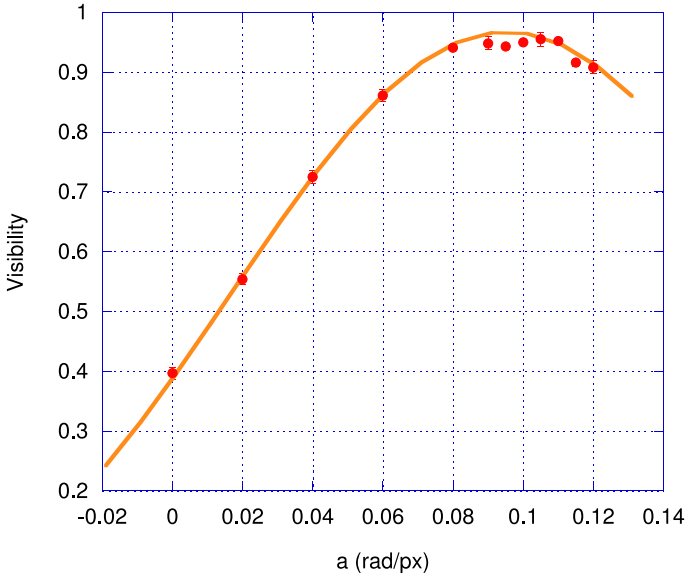

Figure 5.3: *Visibility as a function of the angular compensation paramenter a. We introduce with the SLM the functions $\Phi_{SLM}(n) = -a \cdot (n - n1) + a \cdot (n - n2) + b$. Red points are the experimental data while the red curve is the theoretical prediction calculated from eq. (5.6) and corrected including the residual delay time and the effect of the pixel gaps. The pump beam waist is $870\,\mu m$, the angular and spectral selection are $\Delta\theta = 10\,mrad$ and $\Delta\lambda = 10\,nm$.*

calculated from eq. (5.6) and corrected as follow. The maximum value of the theoretical prediction is lowered by the residual delay time (about 1 %) and by the effect of the pixel gaps. As described above the SLM pixels are large $97\,\mu m$ and are separated by a small gap ($3\,\mu m$); thus we compensate the angular phase just to the 97 % of the photons, while the residual 3 %

are not compensated. The theoretical prediction V_{th} is then modified in the following way

$$V_{th}^{SLM}(a) = 0.97 \cdot V_{th}(a) + 0.03 \cdot V_{th}(a = 0);$$

where $V_{th}(a = 0)$ is the uncompensated value.

5.3 Second order spectral effect

As calculated in sec. 2.3.1 the spectral contribution to the total relative phase (in absence of walkoff) is just at the second order. Since signal and idler have the same group velocities, the first order term in ω_s is the same, but opposite in sign, and thus naturally compensated. In general the presence of a large spectrum results in a global reduction of the state purity. In the case of transverse momentum conserved it holds the first order relation $\omega_s \propto \theta + \theta'$ and thus the term $\omega_s^2 \propto \theta^2 + \theta'^2 + 2\theta\theta'$ could be partially compensated by quadratic angular phase term. The compensation is only partial since the cross term $\theta\theta'$ could not be introduced by the SLM.

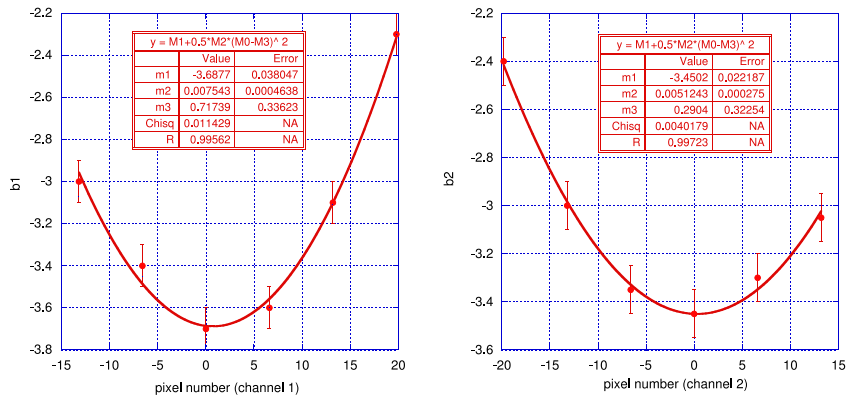

Figure 5.4: *Residual quadratic phase due to the large spectrum coupled. We close the slits at $\Delta\theta = 2\,mrad$ and keeping fixed one of them at the central angle θ_0 we translate the other slit in the transverse direction. With the polarizers at 45°, −45° we measure the coincidences scanning the constant phase parameter b_1. For each position of the slit we register the b_1 value corresponding to the minimum value of the coincidences. The slit position is reported in pixel number at the SLM position. The solid lines are the quadratic fits.*

To show the presence of such second order phase we measure the residual phase profile along SPDC angular distribution once the linear term has been compensated. The pump beam radius on the crystal is $565\,\mu m$, the

spectral filtering on both channel is done by long pass filters with cut-on wavelength at $715\,nm$. We close the slits at $\Delta\theta = 2\,mrad$ and keeping fixed one of them (say 2) at the central angle θ_0 we translate the other slit (1) in the transverse direction. With the polarizers at $45°$, $-45°$ we measure the coincidences scanning the constant phase parameter b_1. For each position of the slit we register the b_1 value corresponding to the minimum value of the coincidences. We do the same with the other arm. The results are plotted in fig. (5.4) together with a quadratic fit; slit position is reported in pixel number at the SLM position. We can see that, with large spectrum coupled, in both arms there is a residual quadratic angular phase. Then opening the slits at $\Delta\theta = 10\,mrad$ we measure the state purity. Linear compensation gives a purity of 0.855 ± 0.005, while introducing the quadratic angular compensations with the parameters found by the fits we obtain a purity of 0.885 ± 0.003.

5.4 Symmetric and Asymmetric linear phase

In this section we will show how the spatial profile of the pump affects the purity of the entangled state. Using the SLM we have the possibility of study separately the effects of the functions f and g described in sec. 2.2.

Consider the equations (2.64) and the convention of positive angles in the anti-clockwise direction so that $\theta_0' = -\theta_0$. A first order expansion in the angles gives:

$$\Delta k_{\parallel} \simeq C + D\,(\theta - \theta') = C + D\,\theta_-; \tag{5.8}$$

$$\Delta k_{\perp} \simeq A + B\,(\theta + \theta') = A + B\,\theta_+, \tag{5.9}$$

where the terms A and C hide the spectral dependence, while B and D are constants, and we have called $\theta_\pm = \theta \pm \theta'$.

With these notation one can show that the visibility factorizes in the form

$$Vis = \mathcal{R}e \int d\theta_- |f(\theta_-)|^2\, e^{\imath[\alpha\theta_- + \phi^-_{SLM}(\theta_-)]} \cdot \int d\theta_+ |g(\theta_+)|^2\, e^{\imath[\delta x\,(A + B\,\theta_+) + \phi^+_{SLM}(\theta_+)]} = \tag{5.10}$$

$$= \mathcal{P} \cdot \mathcal{R}e \int d\theta_+ |g(\theta_+)|^2\, e^{\imath[\delta x\,(A + B\,\theta_+) + \beta_+\,\theta_+]}, \tag{5.11}$$

where $f(\theta_-) = sinc(\Delta k_{\parallel})$ and $g(\theta_+) = g(\Delta k_{\perp})$ are explicited in eqs. (2.59) and (2.60). The integral in θ_- has been threated previously in section 5.2; α is the natural linear slope to be compensated by the SLM. Here we consider it as a number $\mathcal{P}$ giving the maximal purity after SLM compensation. We remember that the function g is the fourier transform of the transverse profile of the pump electric field. In the case of null walk off ($\delta x = 0$) the

visibility as a function of β_+ is the fourier transform of the square modulus of g. We remark that with the SLM we can study separately the two integrals in θ_- and θ_+ by measuring the visibility as a function of a linear slope β introduced simmetrically ($\phi^+_{SLM}(\theta_+) = \beta_+\theta_+$) or anti-symmetrically ($\phi^-_{SLM}(\theta_-) = \beta_-\theta_-$). The anti-symmetric case is already threated above and the visibility is plotted as a function of the slope in figure (5.3) and its behaviour depend only on the *sinc* function.

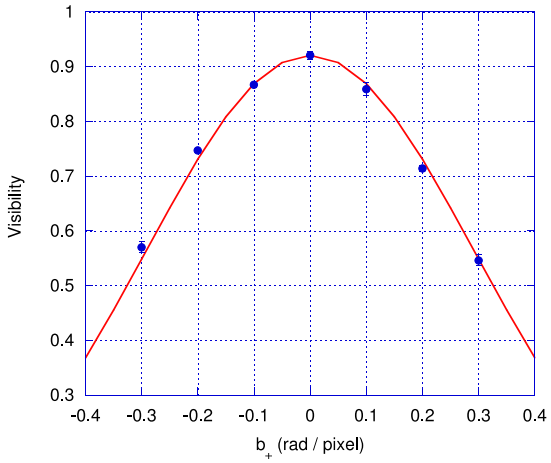

Figure 5.5: *Visibility as a function of the symmetric slope b_+. After linear compensation we add on both channels the value b_+. The red line is the theoretical prediction calculated with the $|g(\Delta k_\perp)|^2$ measured with the method of the lens explained in the text.*

Here we consider more in details the function $g(\Delta k_\perp)$ defined in eq. 2.60. Till now we have neglected the phase profile of the gaussian pump field due to the radius of curvature. Considering for instance only the variable x, we write the pump field profile as

$$B(x) = e^{-\frac{x^2}{w^2}} e^{-\imath\frac{k}{2R}x^2},$$

with w the beam radius on the crystals and R the radius of curvature of the phase profile in the same position. The function g become

$$g(\Delta k_\perp) = \int dx B(x) e^{\imath\Delta k_\perp x} = e^{-\frac{w_{eff}^2}{4}\Delta k_\perp^2} e^{\imath\frac{k}{2R_{eff}}\Delta k_\perp^2}, \tag{5.12}$$

where $w_{eff} = w/\sqrt{1+\frac{k^2 w^2}{4R^2}}$ and $R_{eff} = R\cdot\left(\frac{4}{w^4}+\frac{k^2}{R^2}\right)$. The phase term is less important since for the visibility calculation we need only $|g(\Delta k_\perp)|^2$. In order to avoid approximations we experimentally measure the effective waist

w_{eff}. We set a cilindrical lens with focal length $f = 1000\,mm$ at crystals output and we acquire with a camera the intensity profile in the focal plane $|g(x_f)|^2$ and, by the measure of its width, we calculate the effective waist w_{eff} using the relation $\frac{k\,x_f}{f} = \Delta k_\perp$. Considering the effective and the real waist on the crystals (w_{eff} and w) one can calculate the radius of curvature of the incident pump beam.

We now consider the case without a walk off. To obtain this configuration we insert on the pump path two $0.5\,mm$ crystals with optical axes in perpendicular planes and opposite orientation respect to the generating crystals. The pump beam radius is set at $w = 215\mu m$ using a telescopic system. We filter $10\,nm$ of the spectral distribution and $10\,mrad$ of the angular one. Using the SLM we insert on signal and idler beams the phase functions

$$\phi_{SLM}(\theta, \theta') = (-\alpha_{opt} + \beta_+)\theta + (\alpha_{opt} + \beta_+)\theta'$$

and we measure the visibility as a function of $b_+ = \beta_+ \frac{h}{D}$, with $h = 0.1\,mm$ the pixel width and $D = 310\,mm$ the SLM distance from the crystals. Here α_{opt} is the optimal value of the slope for angular compensation. Notice that it is introduced with opposite signs on the two channels. The result is plotted in figure (5.5). The red line is the theoretical prediction calculated with the $|g(\Delta k_\perp)|^2$ measured with the method of the lens explained above.

In future our purpose is to use this method to analyse other configuration of the pump transverse profiles and also to study the effect of the walk off between $|HH\rangle$ and $|VV\rangle$ pairs which is related with the same integral.

Part II

Quantum Information applications

Chapter 6

Demonstration of a programmable source of two-photon multiqubit entangled states

We suggest and demonstrate a novel source of two-photon multipartite entangled states which exploits the transverse spatial structure of spontaneous parametric down-conversion together with a programmable spatial light modulator (SLM). The one-dimensional SLM is used to perform polarization entanglement purification and to realize arbitrary phase gates between polarization and momentum degrees of freedom of photons. We experimentally demonstrate our scheme by generating two-photon three-qubit linear cluster states with high fidelity using a diode laser pump with a limited coherence time and power on the crystal as low as $\sim 2.5\,mW$*. Such a work has been published on Physical Review A [27].*

6.1 Introduction

Multiqubit entangled states, e.g. cluster states, are key resources to realize several protocols of quantum information processing, including measurement based quantum computation [49, 50, 51], quantum communication [52] and quantum error correction [53]. Besides, they found applications in advanced fundamental tests of quantum nonlocality [54, 55, 56, 57]. Basically, there are two ways to generate multiqubit entangled states, e.g. cluster states. On one hand, one may increase the number of entangled photons [58, 59, 60, 61]. On the other hand one may use different degrees of freedom of the same pair of photons [62, 63, 51, 64] achieving so-called hyperentanglement. The second method offers a larger robustness against decoherence

and nonunit detector efficiency. Four and six multiphoton cluster states have been experimentally created [58, 59, 60] as well as two-photon four- [63, 62, 51, 65, 66, 67, 68, 69, 70, 71, 72, 73] and six-qubit cluster states [74].

In this chapter we suggest and demonstrate a novel scheme to generate two-photon multipartite entangled states which exploits the transverse spatial structure of spontaneous parametric downconversion and the programmable spatial light modulator (SLM) described in sec. 3.4. This kind of devices have been already used as pulse shaper for Bell state generation [75], as amplitude modulators for momentum imaging and qudit generation [76] as well as diffractive elements to operate on orbital angular momentum [77]. Here we employ SLM in an innovative way to realize two-photon multiqubit/qudit entangled states and demonstrate its use in the generation of two-photon three-qubit linear cluster states with high fidelity.

The novelty of our setup is twofold. On the one hand, we use the SLM for purification as explained in sec. 5.2. On the other hand, we fully exploit the properties of the SLM to realize arbitrary phase-gates between polarization and momentum degrees of freedom. In this way, we obtain an effective, low cost, source of two-photon multipartite entanglement using a pump with low power and a limited coherence time.

In the next Section 6.2 we address the generation of two-photon multiqubit/qudit entangled states and describe our experimental setup, used to demonstrate the generation of two-photon three-qubit linear cluster states with high fidelity. Section 6.3 closes the paper with some concluding remarks.

6.2 Our source of two-photon multiqubit entanglement

For this application we use the following experimental condition: multimode pump beam (without spatial filtering), the SLM is set at a distance $D = 500\,mm$ from the crystals while the couplers at a distance of $700\,mm$. Our experimental setup allows us to collect the downconverted photons within a wide spectrum and angular distribution. In order to underline this fact the pump power on the crystals has been intentionally left very low ($2.5\,mW$) by using an amplitude modulator. To collect as many photons as possible we make the imaging of the pump spot on the crystals ($\simeq 1.5mm$) into the optical fibers core (diameter of $62.5\,\mu m$) using the coupler lenses. the spectral filters are longpass with a cut on wavelength of $715\,nm$. Setting the slits at $\Delta\theta \simeq 6.5mrad$ and the iris with a diameter of $13\,mrad$ we collect up to 100 coincidence counts per second. In turn, the purification of the state works as follows: starting from a visibility equal to 0.423 ± 0.016 we achieve 0.616 ± 0.012 after the delay compensation with the crystals and 0.886 ± 0.012 after the spatial compensation with the SLM. Finally, by closing the iris at

the same width of the slits we obtain 0.899 ± 0.008. Actually, we verified experimentally that variations of the phase in the azimuthal direction have only a minor effect. The residual lack of visibility is in turn due to the low spatial coherence of the pump, which is spatially multimode. After purification we obtain a polarization entangled state (here called $|\Phi\rangle$) over a large angle ($6.5\, mrad$) and spectral distribution ($\sim 70\, nm$).

In order to generate multipartite entangled states, and in particular cluster states, purification is just the first step. Here we suggest a new technique based on the use of the SLM. We consider the signal and the idler beams divided in N and M subdivisions (see Fig. 6.1(d)), which individuate different momentum qudits, and write the signal and idler momentum state as

$$|s\rangle = \sum_{n}^{N} a_n |n\rangle_s \,, \quad |i\rangle = \sum_{m}^{M} a_m |m\rangle_i$$

with $n = 0, 1, ..., N-1$ and $m = 0, 1, ..., M-1$. The total momentum state is $|\Psi\rangle = |s\rangle \otimes |i\rangle$. This is not an entangled state in the momentum since for a certain signal angle θ, the idler sweeps a wide interval of θ', actually covering all the angular acceptance $\Delta\theta$ due to the broad down conversion spectrum. This situation corresponds to the one depicted in the left panel of fig. (4.5). The global state is thus given by $|\Phi\rangle \otimes |\Psi\rangle$, where polarization provides two qubits, and the rest of information is encoded onto the momentum degrees of freedom [78, 79, 80].

The action of the SLM corresponds to impose a phase shift only on the horizontal component of polarization, leaving the vertical part undisturbed. We exploit this property to add a different constant phase, besides the purification ones, for each portion of signal and idler. This corresponds to the action of a set of controlled phase-gates $C_{\boldsymbol{\phi}}$, $\boldsymbol{\phi} = \{\phi_{0i}, ..., \phi_{M-1i}, \phi_{0s}, ..., \phi_{N-1s}\}$ to the state $|\Phi\rangle \otimes |\Psi\rangle$. Using a suitable number of sectors (power of two) one may generate multiqubit entangled states of the form $|\Xi\rangle = C_{\boldsymbol{\phi}} |\Phi\rangle \otimes |\Psi\rangle$.

The simplest example, which we implemented experimentally, is obtained using $M = 1$ and $N = 2$, i.e. by dividing the signal beams in two parts exploiting the SLM to apply a phase ϕ to only one of them (see Fig. 6.1(a) and (b)). This leads to the generation of a two-photons three-qubit entangled state of the form $\frac{1}{2}[|000\rangle + |110\rangle + e^{\imath\phi}|001\rangle + |111\rangle]$ where, for the first two qubits, $|0\rangle \equiv |H\rangle$ and $|1\rangle \equiv |V\rangle$ whereas the third qubit is the signal momentum. For $\phi = \pi$ one obtains a two-photons three-qubit linear cluster state

$$|C_3\rangle = \frac{1}{\sqrt{2}}[|\Phi^+\rangle|0\rangle - |\Phi^-\rangle|1\rangle] \,,$$

where $|\Phi^{\pm}\rangle$ are standard Bell states. In order to highlight the power of our method let us consider another example, with four qubits: for $M = N = 2$ (see Fig. 6.1(c)) and applying $\phi_{0s} = -\phi_{0i}$, $\phi_{1i} = \pi - \phi_{1s}$ we achieve the

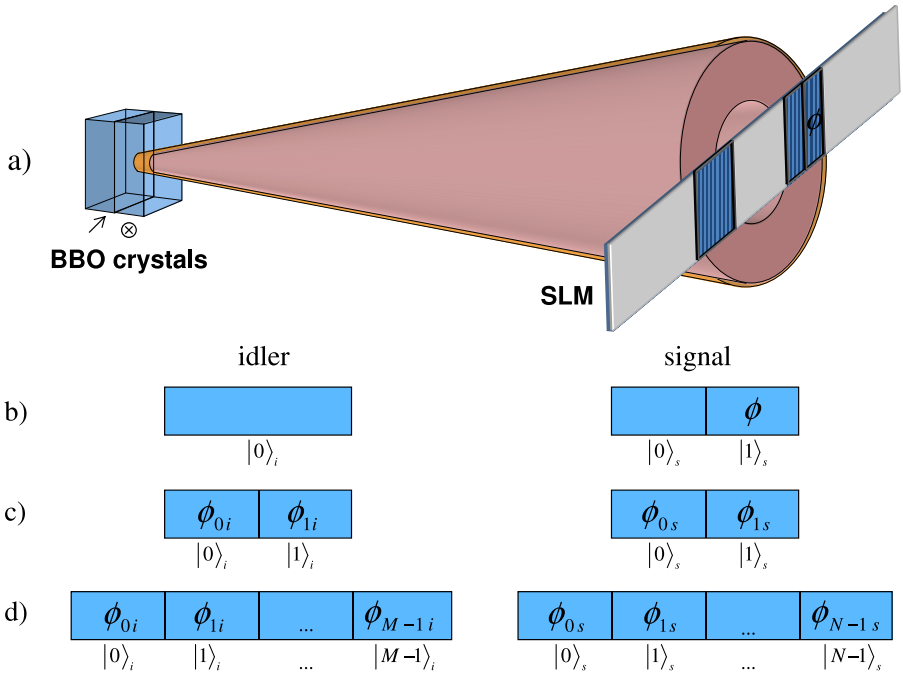

Figure 6.1: *Generation of multipartite entangled/cluster states by the use of SLM. The overall output from SPDC is divided in spatial sections, and a different phase may be imposed to each portion in a programmable way, corresponding to the application of controlled phase-gates. Each spatial section includes several pixels. In (b) we report the momentum state in our experimental implementation* $|\Psi\rangle = \frac{1}{\sqrt{2}}|0\rangle_i(|0\rangle_s + |1\rangle_s)$*; in (c) the state configuration to achieve* $|\Psi\rangle = \frac{1}{2}(|0\rangle_i + |1\rangle_i)(|0\rangle_s + |1\rangle_s)$ *(which may become* $|\Psi\rangle = \frac{1}{\sqrt{2}}(|0\rangle|1\rangle + |1\rangle|0\rangle)$*) upon the use of a spectral filter, bandpass of* $10nm$*). In (d) the generic configuration leading to the momentum state* $|\Psi\rangle = |s\rangle \otimes |i\rangle$*.*

four-qubit entangled state

$$|\Xi_4\rangle = \frac{1}{2}\big[|\Phi^+\rangle|00\rangle - |\Phi^-\rangle|11\rangle + |\Delta^+(\phi_t)\rangle|01\rangle - |\Delta^-(\phi_t)\rangle|10\rangle\big]\,,$$

where $\phi_t = \phi_{0i} + \phi_{1s}$ and $|\Delta^{\pm}(\phi_t)\rangle = \frac{1}{\sqrt{2}}[|00\rangle \pm e^{\mp\imath\phi_t}|11\rangle]$. We foresee that using a narrower spectral filter for the downconverted photons it is possible to select different regions of the angular distribution in a way that allow us to engineer entanglement also for the momentum degrees of freedom. Using a $10nm$ bandpass filter and coupling $\Delta\theta \simeq 1.6mrad$ on the momentum channels $|n\rangle_s, |m\rangle_i$, for $N, M = 2$, we would have $|\Psi\rangle = \frac{1}{\sqrt{2}}(|0\rangle|1\rangle + |1\rangle|0\rangle)$. In such a way the total state would be the two-photon four-qubit cluster state reported in [62, 63].

6.2.1 State reconstruction

Upon properly programming the SLM, i.e. by setting $M = 1$, $N = 2$, and $\phi = \pi$ as in Fig. 6.1(b), our scheme may be set to generate, in ideal conditions, the cluster state $|C_3\rangle$. In order to characterize the output state, denoted by R_3, and to check the effects of the decoherence processes, we have performed state reconstruction by (polarization) quantum tomography [32, 33] as largely explained in sections 1.4 and 4.2.

At first we reconstruct the purified state prior the action of the SLM phase-gate, i.e. without addressing the momentum qubit. Then, we reconstruct the two reduced states $\varrho_j = \frac{1}{p_j}\mathrm{Tr}_3[|j\rangle_{ss}\langle j|\, R_3]$ obtained by measuring the momentum qubit after the phase-gate. This is obtained by moving the slit on the signal to select the corresponding portion of the beam. Results are summarized in Fig. 6.2.

As it is apparent from the plots our scheme provide a reliable generation of the target states. Fidelity of the purified polarization state is about $F \simeq 0.90 \pm 0.01$, whereas fidelities of the conditional states $F_0 = \langle\Phi^+|\varrho_0|\Phi^+\rangle$ and $F_1 = \langle\Phi^-|\varrho_1|\Phi^-\rangle$ are given by $F_0 = 0.92 \pm 0.01$ and $F_1 = 0.90 \pm 0.01$ respectively. In order to achieve this precision we have employed a long acquisition time ($\sim 60s$) thus also demonstrating the overall stability of our scheme. We also report the visibility of the state prior the action of the SLM phase-gate, which confirms the entanglement purification process [81].

6.3 Conclusions

We have suggested and implemented a novel scheme for the generation of two-photon multipartite entangled states. In our device a programmable spatial light modulator acts on different spatial sections of the overall down-conversion output and provides polarization entanglement purification as well as arbitrary phase-gates between polarization and momentum qubits. It should be mentioned that also measurements on the momentum qubits benefits from our configuration. In fact, addressing momentum is equivalent to select portions of the signal (idler) beam and then make them interacting, say by a beam splitter and other linear optical elements, to perform arbitrary momentum measurements. In our scheme this may be implemented in a compact form since the portions of the beam are quite close each other, and we may work with beam splitter at non normal incidence. Overall, our scheme represents an effective, low cost, source of two-photon multi-qubit/qudit entanglement. We foresee applications in one-way quantum computation and quantum error correction.

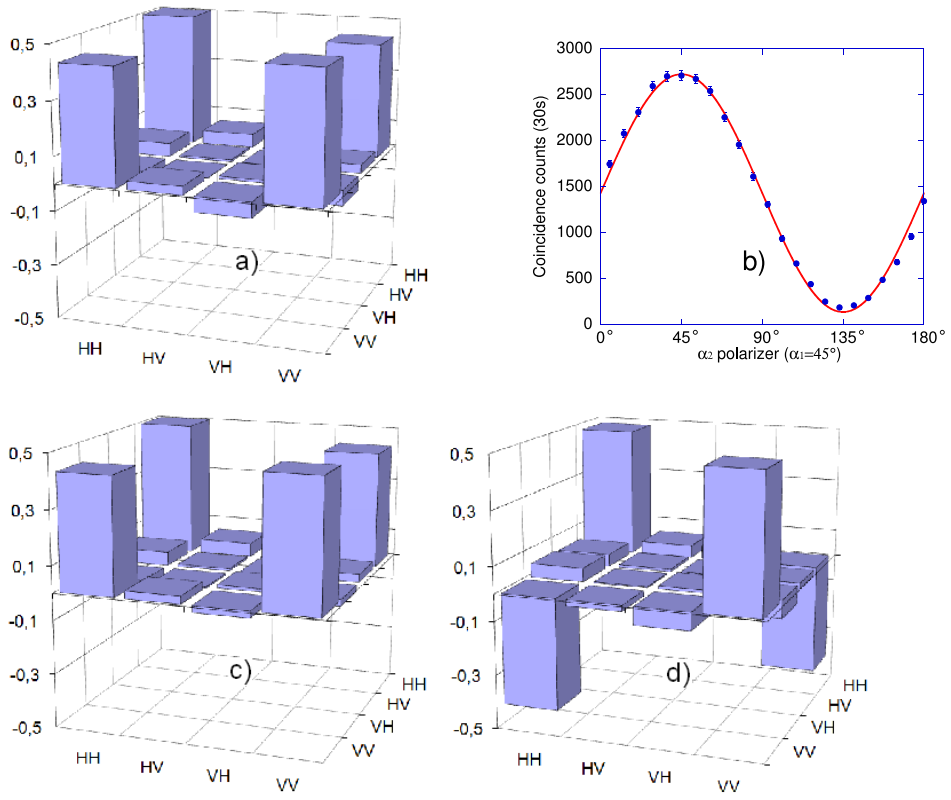

Figure 6.2: *Characterization of the output state. In (a) we report the tomographic reconstruction (real part) of the global purified polarization entangled state prior the action of the phase-gate, whereas in (b) we show the corresponding visibility curve and the fit with the curve* $\cos^2(\alpha_2 - 45°)$ *(solid line). In (c) and (d) we report the tomographic reconstructions (real part) of the reduced states* ϱ_0 *and* ϱ_1*.*

Chapter 7

Nonlocal compensation of pure phase objects with entangled photons

We suggest and demonstrate a scheme for coherent nonlocal compensation of pure phase objects based on two-photon polarization and momentum entangled states. The insertion of a single phase object on one of the beams reduces the purity of the overall detected state and the amount of shared entanglement, whereas the original entanglement can be retrieved by adding a suitable phase object on the other beam. In our setup polarization and momentum entangled states are generated by spontaneous parametric down-conversion and then purified using a programmable spatial light modulator, which may be also used to impose arbitrary space dependent phase functions to the beams. As a possible application, we suggest and demonstrate a quantum key distribution protocol based on nonlocal phase compensation. Such a work has been published on Physical Review A [28].

7.1 Introduction

In what is usually referred to as *ghost imaging* the coherent imaging of an object is achieved with incoherent light upon exploiting the spatial correlations between two light beams [82]. The object interacts with one of the beams and an image of the object is built up by scanning the other beam (see Fig. (7.1)). Ghost imaging may be obtained either with classically correlated beams [83, 84, 85], as those obtained by splitting the light from a (pseudo) thermal source, or with entangled beams [86, 87, 88], as those obtained by parametric downconversion. In the latter case one may achieve in principle higher visibility.

For objects which modify only the amplitude of light an image may be obtained with a single spatially incoherent beam upon measuring the

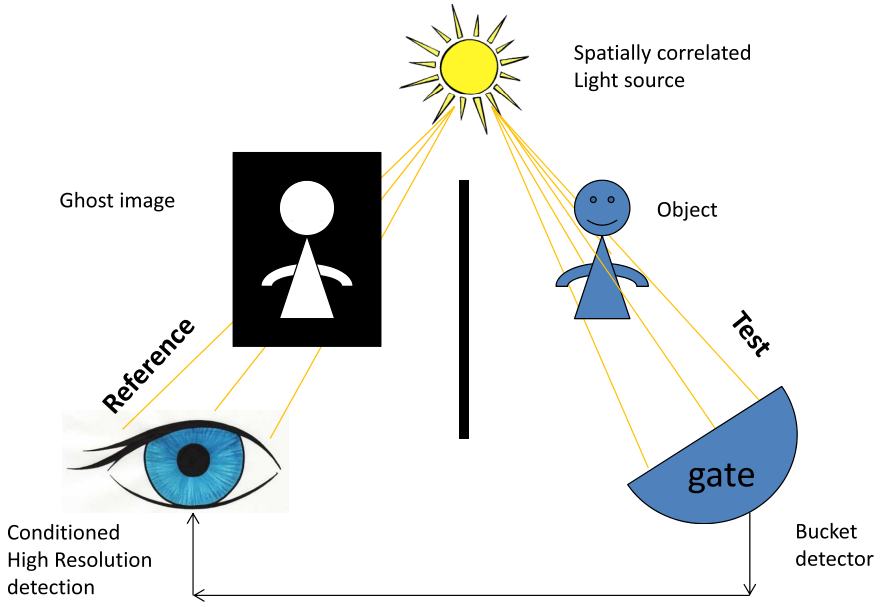

Figure 7.1: *Ghost Imaging idea. An object is shined by a light beam, the test beam; its image is reconstructed observing the reference beam. The detector set on the test arm is a bucket detector, i.e. it reveals only the presence or not of a photon. The detector on the reference beam is an high resolution one (a CCD camera) and it is configured for conditioned detection with the test. The heart of the technique is the use of spatially correlated light source such as entangled beam or classical correlated beams like (pseudo) thermal light at the output ports of a beam splitter.*

autocorrelation function in the far field, without the need of ghost imaging. This is no longer possible when the object is also modifying the phase of the beam. In particular, it is of interest to investigate ghost imaging in the extreme case of pure phase objects, i.e. objects altering only the phase information carried by the beam. Phase objects are also of intrinsic interest in quantum information processing, since they introduce reversible unitary operations.

Ghost imaging of pure phase objects has been extensively analyzed theoretically and experimentally using both classically or quantum correlated beams [83, 84, 85, 86, 87, 88, 89, 90, 91, 92, 93]. Related effects connected with (nonlocal) dispersion cancellation have been investigated as well, both in the temporal and the spatial domains [94, 95, 96, 97, 98, 99]. In this paper we suggest and demonstrate experimentally a scheme to achieve coherent nonlocal compensation/superposition of pure phase objects, also paving the

way for the reconstruction of the overall phase function imposed to the two beams. Our scheme is based on two-photon polarization and momentum entangled states, which are generated by spontaneous parametric downconversion and purified using a spatial light modulator. The same device is also used to introduce arbitrary phase functions on the two beams, which represent arbitrary phase objects. In our setup the insertion of a single phase object on one of the beams reduces the purity of the overall detected state and the amount of shared entanglement, since the detector traces out the angular degree of freedom. The original entanglement can be retrieved by adding a suitable phase object on the other beam, also proving the unitariety of the operation. The image of both single or double phase objects can be thus obtained by scanning the coincidence counts on one of the two beams. As a possible application, we also suggest and demonstrate a protocol for quantum key distribution based on nonlocal phase compensation.

The paper is structured as follows. In the next Section 7.2 we analyze in some details phase imaging and nonlocal phase compensation of phase objects. Finally, in Section 7.3, we suggest a quantum key distribution protocol based on phase compensation and report about its experimental implementation. Section 7.4 closes the paper with some concluding remarks.

7.2 Phase imaging and nonlocal phase compensation

For this application we use a multimode pump beam (without spatial filtering); after generation the photons travels for a distance $D = 310\,mm$ before traversing the SLM while the couplers are set at a distance of $570\,mm$. Beam radius on the generating crystals is about $500\,\mu m$. Upon expanding the transverse momentum conservation condition to the first order, it can be shown that the angular and the spectral degrees of freedom are connected by the relation

$$\theta' = -\theta + \gamma\omega \,, \tag{7.1}$$

where θ, θ' are the signal and idler shifts from the central emission angles ($\Theta_0 \simeq \Theta_0' \simeq 3^\circ$ in our case), ω is the signal shift from the central frequency of the downconverted beams, and γ is a constant depending only on the signal central frequency and angle (see sec. 2.2.1). The state at the output of the crystals may be written as

$$|\psi\rangle \propto \iint d\theta d\theta' F(\theta,\theta') \left[|H\theta\rangle|H\theta'\rangle + e^{\imath\Phi(\theta,\theta')}|V\theta\rangle|V\theta'\rangle \right] \tag{7.2}$$

where the overall angular distribution

$$F(\theta,\theta') = f(\theta,\theta')\, T[\omega(\theta,\theta')] \,,$$

contains the angular distribution $f(\theta, \theta')$ due to the phase-matching conditions and the transmissivity $T[\omega] \equiv T[\omega(\theta, \theta')]$ of an interference filter set on the signal arm.

In our setup, the purification provided by the SLM allows us to generate good polarization-entangled states with visibility up to $V = 0.912 \pm 0.007$, which may be further increase by spatially filtering the pump to achieve a Gaussian profile. However, ghost imaging also require spatial entanglement and this can be obtained upon exploiting Eq. (7.1), i.e. by narrowing the output spectral range. We use an interference filter, whose action is denoted by $T[\omega]$ in Eq. (7.2), which selects a range of about 10 nm around the central wavelenght 810 nm within the overall downconversion spectrum (~ 100 nm). In such a regime a strong angular correlation (momentum entanglement) is predicted as reported in Fig. (2.8(upper left panel)) and the experimentally measured as reported in fig. (4.5 (right)).

The relative phase in Eq. (7.2) can be written after purification as

$$\Phi(\theta, \theta') = \phi^{(s)}(\theta) + \phi^{(i)}(\theta') \,,$$

where $\phi^{(s)}$ and $\phi^{(i)}$ are phase objects inserted respectively on signal and idler beams by the SLM. Single phase-object imaging consists in setting $\phi^{(i)} = 0$ and reconstruct the phase function $\phi^{(s)}(\theta)$ inserted along the signal arm by scanning the coincidences for different emission angles θ' on the idler arm [93]. Experimentally, we insert the phase function

$$\phi^{(s)}(\theta) = a \sin(k\theta)$$

using the SLM, with $a = 1.35\,\text{rad}$ and $k \simeq 0.57\,\text{mrad}^{-1}$. In Fig. 7.2 we present the results for the ghost imaging: polarizers are set to $\alpha = \pi/4$ on the signal and $\beta = 3\pi/4$ on the idler, the slits aperture are $\Delta = 10\,\text{mrad}$ for the signal and $\delta = 1\,\text{mrad}$ for the idler. The signal slit is centered on $\theta_0 = 0$, while the idler slit varies over different values of θ_0'. The experimental data, already subtracted of the accidental coincidences (coincidence window equal to 50ns, acquisition time 120s) are the red circles, whereas the red solid line is the theoretical prediction as obtained from the following equation

$$C_{\alpha\beta}^{\Delta\delta}(0, \theta_0') = \int_{\theta_0' - \frac{\delta}{2}}^{\theta_0' + \frac{\delta}{2}} d\theta' \int_{-\frac{\Delta}{2}}^{+\frac{\Delta}{2}} d\theta \, |F(\theta, \theta')|^2 \sin^2 \left[\frac{1}{2} \phi^{(s)}(\theta) \right] .$$

For comparison we also report the measured value of the direct counts (blue squares, acquisition time 10s) with the corresponding theoretical prediction (solid blue line), i.e.

$$C_{\alpha\beta}^{\Delta\delta}(0, \theta_0') = \int_{\theta_0' - \frac{\delta}{2}}^{\theta_0' + \frac{\delta}{2}} d\theta' \int_{-\frac{\Delta}{2}}^{+\frac{\Delta}{2}} d\theta \, |F(\theta, \theta')|^2 \,.$$

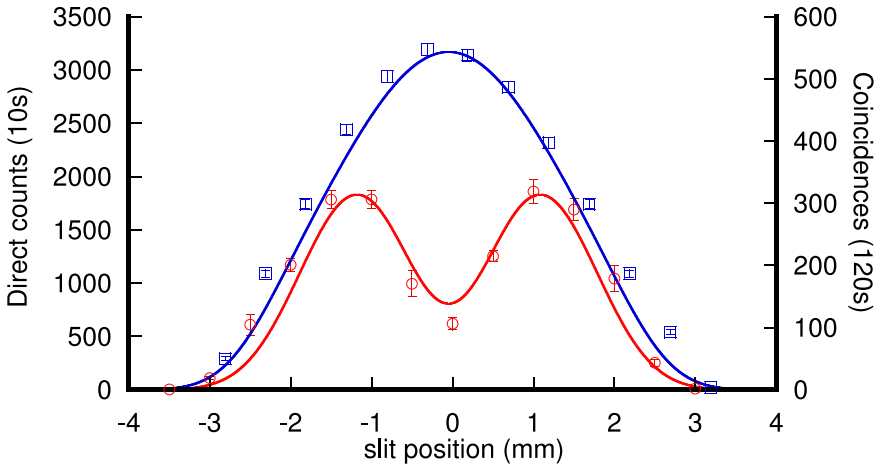

Figure 7.2: *Phase imaging after inserting the phase function* $\phi^{(s)}(\theta) = a\sin(k\theta)$ *on the signal beam, with* $a = 1.35\,rad$ *and* $k \simeq 0.57\,mrad^{-1}$. *Blue squares are the direct counts whereas red circles are the coincidences (red circles). Solid lines are the corresponding theoretical predictions (blue and red lines respectively) as a function of the idler slit position. From the coincidence counts observed by scanning the idler beam, one can reconstruct the phase function along the signal beam.*

As a matter of fact, the insertion of a single phase-object leads to the generation of a set of maximally entangled states at different angles, each one with a different phase term $\phi^{(s)}(\theta)$. The entanglement of the state over a broad angular region is thus reduced to $V = 0.531 \pm 0.008$ due to the integration over many θ and θ'.

Once we have reconstructed the signal phase $\phi^{(s)}(\theta)$ we may further tune entanglement by imposing the phase functions $\phi^{(i)} = \pm\phi^{(s)}$ on the idler beam. In this way we nonlocally superimpose two phase object. We remark that, given the correlation condition $\theta' \simeq -\theta$ (see Fig. (4.5 (right)), the overall phase function inserted by the SLM is given by

$$\begin{aligned} &\phi^{(s)}(\theta) + \phi^{(i)}(\theta') \simeq 2a\sin(k\theta) \qquad \text{if} \quad \phi^{(i)} = -\phi^{(s)}\,, \\ &\phi^{(s)}(\theta) + \phi^{(i)}(\theta') \simeq 0 \qquad\qquad\quad \text{if} \quad \phi^{(i)} = \phi^{(s)}\,. \end{aligned}$$

The corresponding visibility values are $V = 0.057 \pm 0.014$ and $V = 0.888 \pm 0.003$, respectively. The visibility of the entangled state is sligthly lower than the original value $V = 0.912 \pm 0.007$ since the two beams, though showing high angular correlations, are not delta-correlated.

In order to fully characterize the output state, and confirm that visibility is a good figure of merit to discriminate phase functions, we have also per-

formed state reconstruction by polarization qubit tomography for the two different output states. In Fig. 7.3 we present the tomographic reconstruc-

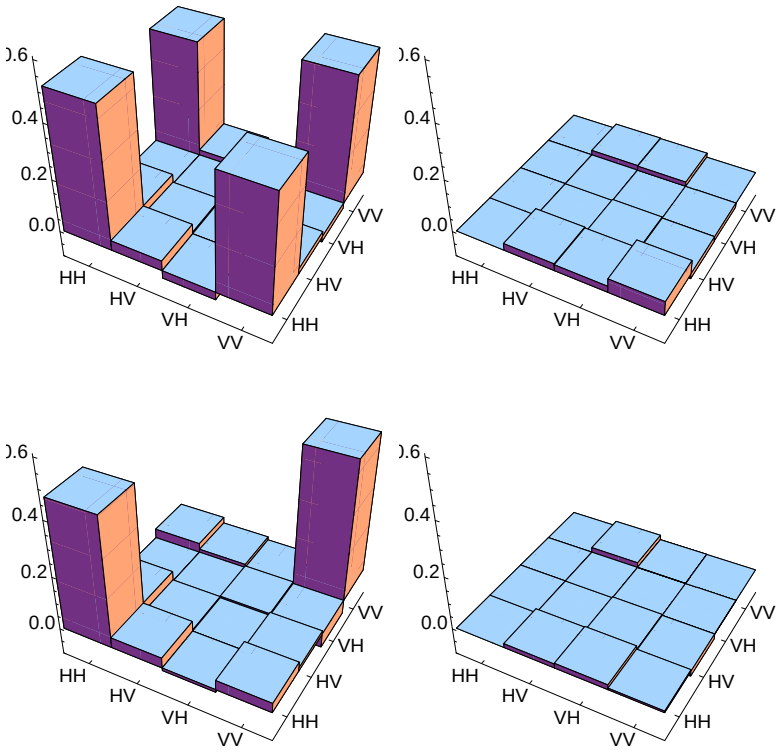

Figure 7.3: *Tomographic reconstruction (the real part of the density matrix on the left and the imaginary one on the right) of the state in which we insert* $\phi^{(i)} = \phi^{(s)} = a\sin(k\theta)$*, with* $a = 1.35\,rad$ *and* $k \simeq 0.57\,mrad^{-1}$ *(upper panels) and of the state obtained with* $\phi^{(i)} = -\phi^{(s)}$ *(lower panels). The corresponding visibilities are given by* 0.888 ± 0.003 *and* 0.057 ± 0.014*, while the measured CHSH-Bell parameters are* $B = 2.658 \pm 0.011$ *and* $B = 1.854 \pm 0.012$ *respectively.*

tions of the density matrix of the two output states: the reconstruction of the state resulting from the overall phase function $\phi^{(i)} = \phi^{(s)}$ is reported in the upper panel (real part on the left, and imaginary part on the right). In the lower panel we show the tomographic reconstruction of the density matrix for the state obtained with $\phi^{(i)} = -\phi^{(s)}$ (real part on the left, and imaginary part on the right). In order to detect the presence of nonlocal

correlations we also measured the Bell-CHSH parameter S. We found

$$S = 1.854 \pm 0.012 \qquad \text{if} \quad \phi^{(i)} = -\phi^{(s)}\,,$$
$$S = 2.658 \pm 0.011 \qquad \text{if} \quad \phi^{(i)} = \phi^{(s)}\,,$$

i.e. we have violation of CHSH-Bell inequality [34] by more than 57 standard deviations for $\phi^{(i)} = \phi^{(s)}$, whereas no violation of the CHSH-Bell inequality is found for $\phi^{(i)} = -\phi^{(s)}$, for which the measures S is less than the threshold $S = 2$ by 12 standard deviations.

7.3 A QKD protocol based on nonlocal phase compensation

As a possible application of nonlocal phase compensation, we suggest to exploit the switch between entangled and mixed states for quantum key distribution. Our proposal is based on the fact that Alice and Bob control the signal and the idler arm respectively of the downconversion output. They are thus able to insert independently, and in a random sequence, the phase functions $\phi^{(A)}$ and $\phi^{(B)}$, where $\phi^{(A,B)} = \pm a \sin(k\theta)$. In turn, this may be used to establish a QKD protocol as the analogue of the random choice of the signal basis or of the measurement basis. Alice then encodes the key $(0, 1)$ by adding a constant phase ($\varphi_A = 0, \pi$) to $\phi^{(A)}$. Upon setting the detection polarizers to $\alpha = \pi/4$ and $\beta = 3\pi/4$ we have that for $\phi^{(B)} = \phi^{(A)}$ a highly entangled state is shared, and thus we have a maximum in the coincidence counting rate when $\varphi_A = \pi$ and a minimum when $\varphi_A = 0$. On the other hand, if $\phi^{(B)} = -\phi^{(A)}$ (or if an eavesdropper tries to acquire knowledge about the key), then Alice and Bob share a mixed (or partially mixed) state, and an intermediate counting rate is detected.

In Fig. 7.4 we present the experimental results for the coincidence counting rate in the four possible configurations, which are summarized in Table 7.1, and labelled as follows: $[++/1]$ denotes the case $\phi^{(A)} = \phi^{(B)} = a \sin(k\theta)$ and $\varphi_A = \pi$, corresponding to the faithful transmission of the symbol "1"; analogously $[+ + /0]$ denotes the case $\phi^{(A)} = \phi^{(B)} = a \sin(k\theta)$ and $\varphi_A = 0$, leading to the faithful transmission of the symbol "0". The events that Alice and Bob are rejecting in the sifting stage are $[+ - /0]$ and $[+ - /1]$ corresponding to $\phi^{(A)} = -\phi^{(B)} = a \sin(k\theta)$ and $\varphi_A = 0, \pi$ respectively.

Notice that the purification procedure allows us to generate high-quality entanglement states even when broad angular regions are coupled. Indeed, the measurements used for quantum key distribution has been performed with a larger aperture, in order to compensate the low quantum efficiency of photodetectors and to increase the measurement rate.

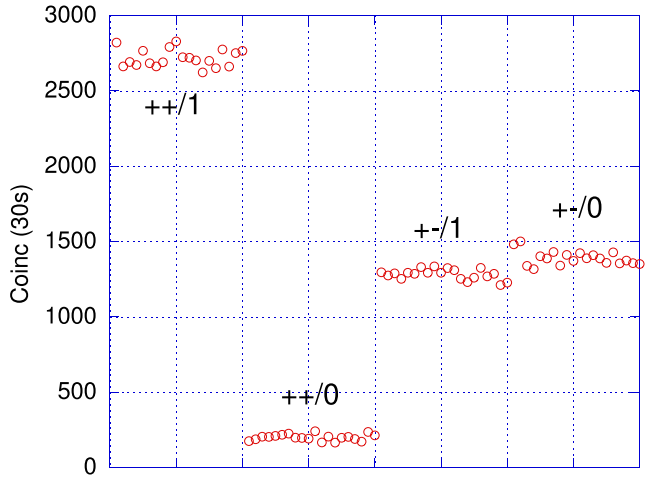

Figure 7.4: *Quantum key distribution by nonlocal phase compensation. The four blocks of data in the plot are the coincidence counting rates in the four different configurations* $[++/1]$, $[++/0]$, $[+-/1]$, *and* $[+-/0]$ *respectively The first two configurations correspond to the faithful transmission of the key, whereas the two others cases are the events that Alice and Bob are going to reject in the sifting stage of the protocol.*

Table 7.1: *A QKD protocol based on nonlocal phase compensation: the phase functions* $\phi^{(A)}$ *and* $\phi^{(B)}$ *play the role of the random choice of the signal basis, whereas the key* $(0,1)$ *is encoded by adding a constant phase* $\varphi_A = 0, \pi$ *to* $\phi^{(A)}$*. When the phase functions are matched,* $\phi^{(A)} = \phi^{(B)}$*, we have the transmission of the key symbols.*

configuration	$\phi^{(A)}$	$\phi^{(B)}$	φ_A	transmitted key
$[++/1]$	$a\sin(k\theta)$	$a\sin(k\theta)$	π	"1"
$[++/0]$	$a\sin(k\theta)$	$a\sin(k\theta)$	0	"0"
$[+-/1]$	$a\sin(k\theta)$	$-a\sin(k\theta)$	π	none
$[+-/0]$	$a\sin(k\theta)$	$-a\sin(k\theta)$	0	none

7.4 Conclusions

In conclusion, we have suggested and demonstrated experimentally an entanglement based scheme to achieve coherent nonlocal compensation of pure phase objects. Our scheme is based on creating two-photon polarization and momentum entangled states where the insertion of a single phase object on one of the beams reduces both the purity of the state and the amount of

shared entanglement, and where the original entanglement can be retrieved by adding a suitable phase object on the other beam. In our setup polarization and momentum entangled states are generated by spontaneous parametric downconversion and then purified using a programmable spatial light modulator. The same device is also used to impose arbitrary space dependent phase functions to the beams, which play the role of arbitrary pure phase objects. Finally, we have suggested a novel quantum key distribution protocol exploiting the effect of nonlocal phase compensation and we have provided its experimental verification. Our results prove experimentally the feasiblity of coherent nonlocal compensation/superposition of pure phase objects and pave the way for further developments, as the reconstruction of the overall phase function imposed to the two beams.

Chapter 8

Programmable entanglement oscillations in a non-Markovian channel

We suggest and demonstrate an all-optical experimental setup to observe and engineer entanglement oscillations of a pair of polarization qubits in an effective non-Markovian channel. We generate entangled photon pairs by spontaneous parametric downconversion (SPDC), and then insert a programmable spatial light modulator in order to impose a polarization dependent phase-shift on the spatial domain of the SPDC output. This creates an effective programmable non-Markovian environment where modulation of the enviroment spectrum is obtained by inserting a spatial grating on the signal arm. In our experiment, programmable oscillations of entanglement are achieved, where the entangled state obtained at the maximum of the revival after sudden death violates Bell's inequality by 17 *standard deviations. The results has been published on Physical Review A [29]*

8.1 Introduction

Entanglement of a bipartite system is usually degraded by the interaction of each subsystem with the environment, which induces decoherence, i.e. an irreversibile loss of information from the system to the rest of the universe [105, 106]. If the interaction is Markovian, i.e. the loss of information is unidirectional, from the system to the environment, then entanglement monotonically decreases and may be also destroyed in a finite time [107, 108, 109, 110, 111]. On the other hand, when some memory effect is present in the interaction between the system and the environment, i.e. when the noisy channel is non-Markovian [112, 113], then a non monotone behaviour of entanglement and, more generally, of quantum correlations may be observed [114, 115, 116, 117, 118, 119, 120, 121]. In fact, entanglement oscillations are

expected in continuous variable systems [122, 123, 124], whereas collapses and revivals of entanglement have been observed with polarization qubits [125].

In this paper we suggest and demonstrate an experimental setup to observe and engineer entanglement oscillations in a programmable way. We address the spatial domain of spontaneous parametric downconversion, and exploit a programmable spatial light modulator to impose a polarization- and position-dependent phase-shift. Since the polarization qubits are obtained by tracing out the spatial degrees of freedom, our apparatus allow us to analize the entanglement dynamics within the "coherence time" of the effective non-Markovian channel. In this framework an effective environment spectrum may be obtained by acting on the spatial profile of the SPDC and, in particular, by a suitable modulation of the angular distribution. In turn, in order to investigate entanglement oscillations we insert a spatial grating on the signal arm to achieve a modulation of the environment spectrum. Besides fundamental interest, our scheme may found applications in engineering decoherence for polarization qubit, e.g. in quantum process tomography.

The paper is structured as follows. In the next Section we describe our scheme for entanglement generation and purification with a detailed analysis of the structure of the angular function. In Section 8.2 we describe how a periodic structure of the angular distribution may be used to induce entanglement oscillations in a programmable way, whereas entanglement decrease and then death may be expected for a non periodical angular distribution. Experimental results are described in details in Section 8.3, with the full characterization of the involved states by quantum tomography reported in Section 8.4. Section 8.5 closes the paper with some concluding remarks.

8.2 Entanglement oscillations in a non-Markovian enviroment

The experimental conditions used for this application of our source are depicted in figure (8.1). The gaussian pump beam on the crystals is quite large (radius of $\sim 500\,\mu m$) and the SPDC spectral filtering is null (a long pass filter with cut on wavelength at $715\,nm$ on both channels). In this situation the angular correlation are washed out and we can consider in a good approximation the function $f(\theta, \theta')$ in the factorable form $G(\theta)G'(\theta')$ as demonstrated in sec. 4.5. Angular selection is done by the slits and is fixed to $10\,mrad$ on both channels. A hand-made grating can be inserted on the signal arm.

Once the state has been purified we impose an the additional phase $\phi_s(\theta) = \alpha\theta$ to the signal photon; the dependence on θ' is traced out, and

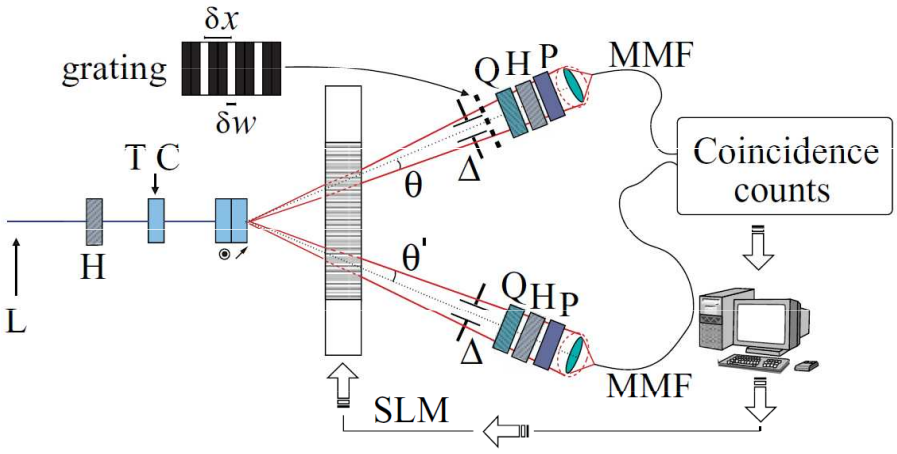

Figure 8.1: *Schematic diagram of experimental setup. Signal and idler cones travel through the SLM and are spatially selected by two irises and two slits set at* $D = 500\,mm$ *with* $\Delta x = 5\,mm$ *(*$\Delta = 10\,mrad$*). Two long-pass filters cut-on wavelength* $715\,nm$ *are used to reduce the background. Thus there is not angular correlation between signal and idler (situation depicted in the left panel of figure (4.5)). Pump beam radius on the crystal is large. A hand-made grating can be inserted on the signal arm. Photons are focused in two multi-mode fibers (MMF) and sent to single-photon counting modules.*

thus no terms containing $G'(\theta')$ appear in the polarization density matrix

$$\varrho = \mathrm{Tr}_{\theta,\theta'}\left[|\psi\rangle\langle\psi|\right] = \frac{1}{2}\Big(|\mathrm{HH}\rangle\langle\mathrm{HH}| + \varepsilon|\mathrm{VV}\rangle\langle\mathrm{HH}| + \varepsilon^*|\mathrm{HH}\rangle\langle\mathrm{VV}| + |\mathrm{VV}\rangle\langle\mathrm{VV}|\Big) \tag{8.1}$$

where

$$\varepsilon(\alpha) = \int d\theta\, |G(\theta)|^2\, e^{\imath\alpha\theta}$$

is the decoherence factor.

In general, the angular distribution may be assumed to be peaked at some central value with a finite width. In this case, the photons coming from different directions (i.e. angles) will experience different relative phase between the horizontal and vertical polarization components. As a consequence, in absence of any purification mechanism, the off-diagonal elements of the polarization density matrix decrease exponentially and the state is driven towards the unentangled mixture.

The situation changes dramatically if the angular distribution is amplitude modulated. In this case the decoherence factor ε may oscillate, i.e. the overall relative phase may refocus and the off-diagonal elements reappear, as

well as entanglement. Since we address the spatial domain, it is straightforward to insert an amplitude modulation on $G(\theta)$, e.g. by inserting a physical obstacle along the signal optical path. As noted above, from the expression of the visibility $Vis(\alpha) = \mathcal{R}e[\varepsilon]$, we see that a periodic structure of the angular distribution would induce oscillations, whereas entanglement decrease and then death may be expected for a non periodical angular distribution. In this framework α may be considered as the evolution parameter of the dynamics of the (noisy) channel, and the periodic structure of the angular distribution as the (spatial) enviroment spectrum. Moreover, the periodic structure implies that in tracing out the spatial degrees of freedom any two-point correlation function of the environment is not single peaked and this is a sign of the non-Markovian character of the channel.

In our apparatus, the amplitude modulation is implemented by means of a hand-made grating with a period δx and a transparent region width δw centered along the signal arm (see Fig. 8.1). As we will see, the narrower are the transparent regions the higher entanglement oscillations are expected. Formally, the insertion of the grating is equivalent to the substitution

$$G(\theta) \to G(\theta) \cdot m(\theta)$$

in the visibility, up to the normalization $\int d\theta \, |G(\theta)m(\theta)|^2 = 1$, where $m(\theta)$ is the periodical unitary step function imposed by the grating. By simply inserting or removing the grating it is possible to compare the different dynamics imposed by a periodical or non-periodical angular distribution.

8.3 Experimental results

After purification we study the behaviour of the visibility as a function of the dimensionless evolution parameter α, governing the linear phase function $\phi_s(\theta) = \alpha\theta$ imposed to the signal by the SLM. As previously discussed, oscillations of entanglement are expected when the grating is inserted. Because of the pixel discretization a step-function with an angular resolution $\zeta = 0.3\,\text{mrad}$ is physically inserted by the SLM in order to approximate the linear functions $\phi_{SLM}(\theta), \phi'_{SLM}(\theta')$. Experimentally, using the SLM, we impose the phase functions

$$\begin{aligned} \phi^e_{SLM}(n) &= -a_{opt}n + b \qquad \text{on idler} \\ \phi^e_{SLM}(n) &= a_{opt}n + \phi^e_s(n) \qquad \text{on signal}\,, \end{aligned}$$

where n is the distance in pixels from the center of the signal beam ($n = 0$ for $\theta = 0$), $a_{opt} = 0.12\,\text{rad/pixel}$ is the optimal slope which allows us to achieve a complete purification, and $b = -\Phi_0$. The linear function $\phi^e_s(n) = a\,n$ is also inserted to study the dynamics, where the experimental evolution parameter is given by $a = \alpha h/L\,\text{rad/pixel}$, $h = 100\mu\text{m}$ being the pixel

width and $L \simeq 330$mm the distance between the SLM and the generating crystals. Since the pixel discretization of the SLM imposes the condition $a \ll 2\pi/\text{pixel}$, high values of a must be neglected in our analysis. We experimentally verified that the curve $V(a)$ saturates to the uncompensated value when $(a + a_{opt}) \to 2\pi$. The revival is expected at

$$a_{rev} = \frac{2\pi D}{\delta x}\frac{h}{L}$$

or, in terms of the angular grating period $\delta\theta$, $\alpha_{rev} = \frac{2\pi}{\delta\theta}$. We choose $\delta x = 2$mm, which leads at $a_{rev} = 0.476\,\text{rad/pixel}$, in order to avoid high values of the evolution parameter, and we set $\delta w = 0.4\delta x$.

In Fig. (8.2) we present the experimental results, together with the theoretical prediction calculated from the expression of the visibility, as a function of the experimental evolution parameter a. Notice that the area under the increasing part of the visibility curve provides an experimental lower bound to the amount of non-Markoviamity of the channels [112].

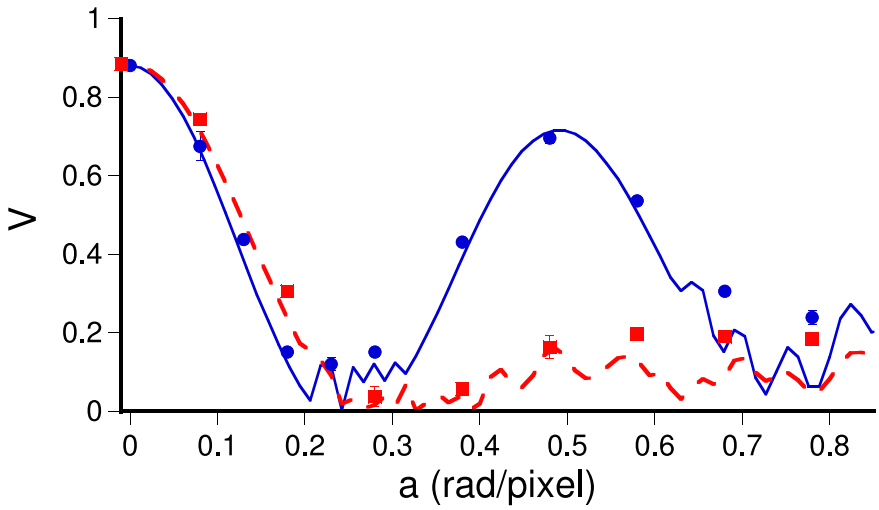

Figure 8.2: *Visibility as a function of the evolution parameter a. Blue circles and red square are the experimental data obtained with and without grating (errors within the symbols). Blue solid line and red dashed line denote the corresponding theoretical predictions.*

Comparing the curve with the one obtained without the grating we see that in the latter case no revival occurs after the degradation of entanglement. We also notice that the minimum occurs for lower values of a compared to the case with the grating.

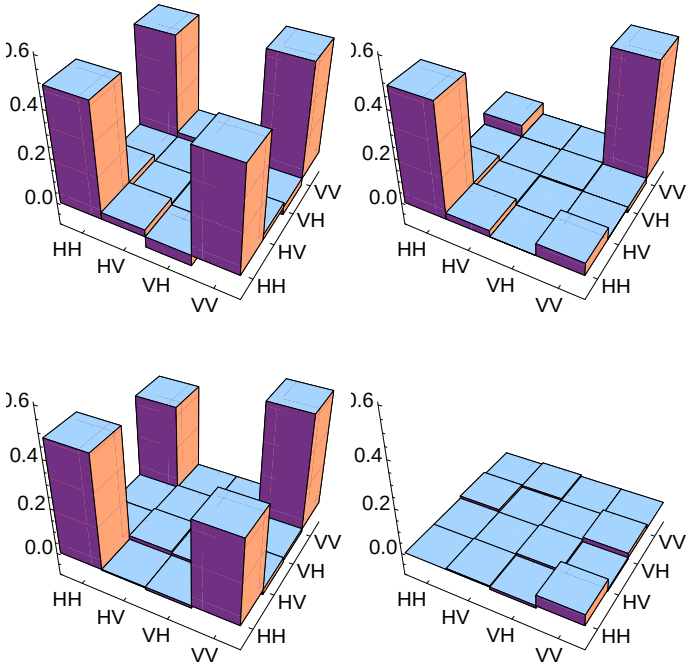

Figure 8.3: *Tomographic reconstruction of a state evolving in the effective non-Markovian channel. In the upper left plot the two-qubit density matrix just after the purification, with visibility* $V = 0.881 \pm 0.004$. *Upon increasing the evolution parameter to* $a = 0.23$ *we achieve the minimum of entanglement oscillations: the density matrix is shown in the upper right plot, the corresponding visibility is* $V = 0.120 \pm 0.016$. *In the lower panels, we show the real and the imaginary part of the reconstructed density matrix at the maximum of entanglement oscillations, which occurs for* $a = 0.48$. *The corresponding visibility is* $V = 0.696 \pm 0.013$, *and the Bell parameter* $B = 2.341 \pm 0.019$.

8.4 State characterization

In order to fully characterize the output state we have also performed state reconstruction by polarization qubit tomography for different values of the evolution parameter a. The purification procedure with the grating inserted leads to a visibility $V = 0.881 \pm 0.004$, the density matrix is graphically represented in the upper left panel of Fig. 8.3. Increasing the evolution parameter to $a = 0.23$, the visibility decreases to $V = 0.120 \pm 0.016$. The corresponding tomographic reconstruction, depicted in the upper right panel of Fig. 8.3, well illustrate the degradation of entanglement. However, we found a consistent revival after a further increasing of the evolution parameter to

$a = 0.48$, where we have $V = 0.696 \pm 0.013$. The corresponding tomographic reconstruction (real and imaginary parts) are reported in the lower panels of Fig. 8.3.

In order to show the revival of the nonlocal correlations we have also measured the Bell parameter S. We found $S = 2.341 \pm 0.019$, which violates CHSH-Bell inequality [34] by more than 17 standard deviations.

8.5 Conclusions

In conclusion, we have suggested and demonstrated an experimental setup to observe oscillations of polarization entanglement in a programmable way. Our scheme is based on a spatial light modulator, which is inserted on the spatial domain of the downconversion output in order to impose a polarization dependent phase-shift on the spatial domain of the SPDC output. An effective programmable non-Markovian environment is then obtained by inserting a spatial grating on the signal arm. This results in a periodic structure of the angular distribution, which corresponds to modulation of the enviroment spectrum, and induces oscillations of entanglement, whereas entanglement decrease and then death is observed for a non periodical angular distribution.

In our experiment, programmable oscillations of entanglement are achieved by varying the linear phase function imposed to the signal by the SLM and verified both by visibility measurements and full polarization state tomography. The entangled state obtained at the maximum of the revival after sudden death violates Bell's inequality by 17 standard deviations.

Our scheme is all-optical and allows us to generate and detect revivals of entanglement and nonlocality, thus paving the way for engineering of decoherence for polarization qubits.

Chapter 9

Experimental investigation of initial system-environment correlations via trace-distance evolution

The trace distance between two states of an open quantum system quantifies their distinguishability, and for a fixed environmental state can increase above its initial value only in the presence of initial system-environment correlations. We provide experimental evidence of such a behavior. In our all-optical apparatus we exploit spontaneous parametric down conversion as a source of polarization entangled states, and a spatial light modulator to introduce in a general fashion correlations between the polarization and the momentum degrees of freedom, which act as environment. Such work, proposed by A. Smirne, has been realized with our source. The results has been published on Physical Review A [30].

9.1 Introduction

The dynamics of an open quantum system S interacting with an environment E is usually described by means of a completely positive trace preserving (CPT) map on the state space of the open system [127]. The very existence of such a map generally requires that the initial correlations between the open system and the environment can be neglected, i.e. $\rho_{SE}(0) = \rho_S(0) \otimes \rho_E(0)$ where $\rho_S(0) = \mathrm{Tr}_E \{\rho_{SE}(0)\}$ and $\rho_E(0) = \mathrm{Tr}_S \{\rho_{SE}(0)\}$. However, this assumption is not always physically justified, especially outside the weak coupling regime [128]. Therefore, different approaches to the description of the reduced system dynamics in the presence of initial correlations have been developed in recent years [129, 131, 130, 132, 133, 134].

An approach for the study of initial correlations which is based on the use of the trace distance and which does not rely on the determination of any reduced dynamical map has been introduced in [135]. In particular, one can find a clear signature of initial system-environment correlations as follows: if the environmental state is fixed, the trace distance between any two reduced states can increase over its initial value only in the presence of initial correlations.

Recently the open system dynamics of two qubits has been experimentally investigated in all-optical settings, where the system is represented by the polarization degrees of freedom, and the environment by the spectral [126] or by the momentum [29] degrees of freedom. Here we report an experimental proof of the feasibility and effectiveness of the abovementioned theoretical scheme [135] for the detection of correlations, observing the effect of initial system-environment correlations in the subsequent open system dynamics by means of the trace distance. In particular, we show an increase of the trace distance between two reduced states, sharing the same initial environmental state, over its initial value on both short and long time scales. Despite the fact that a full tomographic analysis can be performed, thus showing that the experimental setup can cope with the most general situation, the growth of the trace distance can here be detected simply by exploiting visibility data, thus showing that the theoretical analysis can really lead to efficient detection schemes.

The paper is structured as follows: In Section 9.2 we briefly present the general theoretical scheme. In Section 9.3 we describe the important features of the experimental apparatus, whereas in Section 9.4 we describe the use of the spatial light modulator to introduce system-environment correlations, and analyze the evolution of the trace distance. In Section 9.5 we provide the full tomographic reconstruction of the state under investigation. Section 9.6 closes the paper with some concluding remarks.

9.2 Upper bound on trace distance evolution

The trace distance between two quantum states ρ^1 and ρ^2 is defined as

$$D(\rho^1, \rho^2) = \frac{1}{2}\mathrm{Tr}\left|\rho^1 - \rho^2\right| = \frac{1}{2}\sum_k |x_k|, \tag{9.1}$$

with x_k eigenvalues of the traceless operator $\rho^1 - \rho^2$, and its physical meaning lies in the fact that it provides a measure for the distinguishability between two quantum states [136]. It is a metric on the space of physical states, so that for any pair of states ρ^1 and ρ^2 it holds $0 \leq D(\rho^1, \rho^2) \leq 1$. Every CPT map Λ is a contraction for this metric: $D(\Lambda\rho^1, \Lambda\rho^2) \leq D(\rho^1, \rho^2)$, a property which will be crucial in the following analysis.

The dynamics of an open quantum system can be characterized by investigating the dynamics of the trace distance between a pair of reduced states $\rho_S^1(t)$ and $\rho_S^2(t)$, which evolve from two different initial total states $\rho_{SE}^1(0)$ and $\rho_{SE}^2(0)$. The change in the distinguishability between two reduced states can be interpreted as an information flow between the open system and the environment [112, 137]. Indeed, since the reduced states $\rho_S^k(t)$ are obtained from the corresponding initial total states $\rho_{SE}^k(0)$ $k = 1, 2$ through the composition of a unitary operation and the partial trace, the contractivity under CPT maps implies that

$$D(\rho_S^1(t), \rho_S^2(t)) - D(\rho_S^1(0), \rho_S^2(0)) \leq I_{12}(0)\,, \tag{9.2}$$

where

$$I_{12}(0) \equiv D(\rho_{SE}^1(0), \rho_{SE}^2(0)) - D(\rho_S^1(0), \rho_S^2(0))\,. \tag{9.3}$$

That is, the increase of the trace distance during the time evolution is

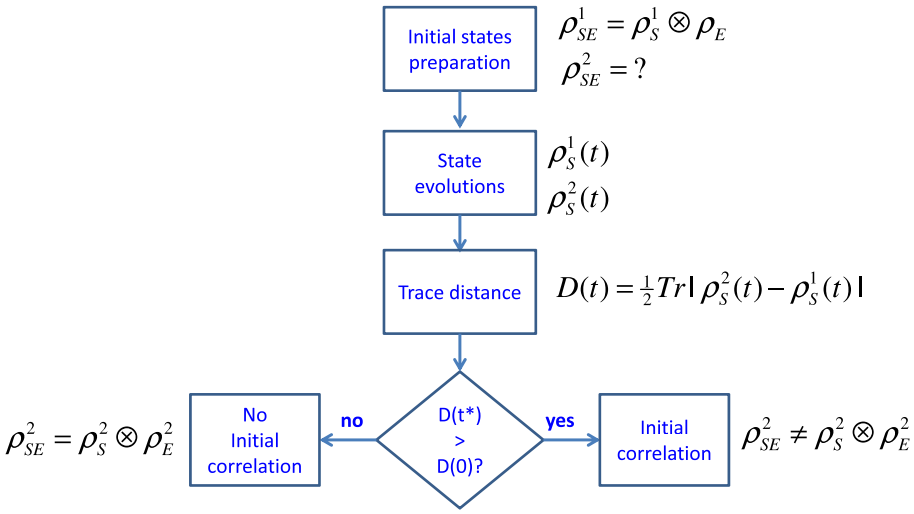

Figure 9.1: *Conceptual diagram of the measure. Two initial states are prepared with the same environment. Without losing generality we prepare system 1 without initial correlation with its environment. During the evolution we measure the trace distance between the reduced states. A growth of the trace distance above its initial value is the signature that the system 2 has initial correlation with its environment.*

bounded from above by the quantity $I_{12}(0)$, which represents the information initially residing outside the open system [135]. It is important to notice that

the bound $I_{12}(0)$ can also qualitatively reproduce non-trivial features of the trace distance dynamics even if it is far from being reached [138]. If the initial total states are uncorrelated and with the same environmental state, i.e. $\rho^1_{SE}(0) = \rho^1_S(0) \otimes \rho_E(0)$ and $\rho^2_{SE}(0) = \rho^2_S(0) \otimes \rho_E(0)$, then $I_{12}(0) = 0$. Thus, for identical environmental states, one can find an increase of the trace distance

$$D(\rho^1_S(t), \rho^2_S(t)) > D(\rho^1_S(0), \rho^2_S(0))$$

at a time t only if some correlations are present in at least one of the two initial total states.

9.3 Experimental setup

In our all-optical experimental setup the total system under investigation consists in a two-photon state produced by spontaneous parametric down-conversion. We look at the evolution of the two-qubit polarization entangled state, which represents the reduced system, and trace out the momentum degrees of freedom, which are not observed and represent the environment. We exploit a programmable spatial light modulator (SLM) to impose an arbitrary polarization- and position-dependent phase-shift to the total state. A linear phase is set both on signal and idler beams in order to purify the state, whereas an additional, generic, phase function may be imposed to introduce initial correlations between the polarization and the momentum degrees of freedom in a very general way. A further linear phase is then used as a time evolution parameter for the two-qubit state (see ch. 8).

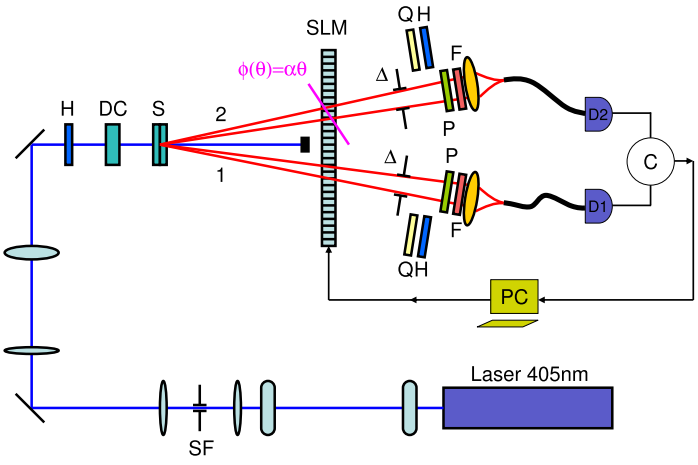

Figure 9.2: Diagram of the experimental setup.

The experimental setup is shown in Fig. 9.2. A linearly polarized CW, 405 nm, diode laser (Newport LQC405-40P) passes through two cylindrical

lenses which compensate beam astigmatism, then a spatial filter (SF) selects a Gaussian spatial profile and a telescopic system prepares a collimated beam with beam radius of 550 μm. A couple of 1mm Beta Barium Borate (S) crystals, cut for type-I down conversion, with optical axis aligned in perpendicular planes, are used as a source of couples of polarization and momentum entangled photons [8, 11]. The process preserves the total energy and the transverse momentum. The couples are generated around a central angle of $\pm 3^\circ$ and we select $\Delta = 10$ mrad with the two slits set at 500 mm from the generating crystals. Two long-pass filter (F) with cut-on wavelength of 780 nm set behind the couplers are used to reduce the background and to select about 60 nm around the central wavelength 810 nm.

9.4 System-environment correlations and trace distance evolution

9.4.1 Theoretical description of the experiment

In our scheme the SLM performs two basic tasks. First, it allows us to engineer the initial state by the introduction of an arbitrary phase $\varphi(\theta)$. Besides, it provides the effective system-environment interaction term sensitive to both the polarization and the momentum degrees of freedom, through the introduction of a linear phase $\alpha\theta$, where α is the time evolution parameter. The total system-environment state is thus given by:

$$|\psi_{SE}(\alpha)\rangle = \frac{1}{\sqrt{2}} \int d\theta d\theta' G(\theta) G'(\theta') \times \left(|H\theta\rangle|H\theta'\rangle + e^{i(\alpha\theta+\varphi(\theta))}|V\theta\rangle|V\theta'\rangle \right). \tag{9.4}$$

The factorized form $G(\theta)G'(\theta')$ is justified by the large spectral distribution (see sec. 4.5). Moreover, $G(\theta)$ is a Gaussian-like shape function with FWHM of 6 mrad. Because of the phase $\varphi(\theta)$, the state in Eq. (9.4) is correlated, i.e.

$$\rho_{SE}(\alpha) = |\psi_{SE}(\alpha)\rangle\langle\psi_{SE}(\alpha)| \neq \rho_S(\alpha) \otimes \rho_E(\alpha)\,,$$

and this is true also for the initial total state, i.e. for $\alpha = 0$. Upon tracing out the momentum degrees of freedom (environment), the polarization state (open system) is given by

$$\begin{aligned} \rho_S(\alpha) \;=\; & \frac{1}{2}\left(|HH\rangle\langle HH| + \epsilon(\alpha)|VV\rangle\langle HH| \right. \\ & \left. + \epsilon^*(\alpha)|HH\rangle\langle VV| + |VV\rangle\langle VV|\right), \end{aligned} \tag{9.5}$$

where

$$\epsilon(\alpha) = \int d\theta |G(\theta)|^2 e^{i(\alpha\theta+\varphi(\theta))}\,.$$

Since the angular distribution $G(\theta)$ is symmetric and we use odd functions $\varphi(\theta)$, the quantity $\epsilon(\alpha)$ is real and it equals the interferometric visibility $V(\alpha) = \mathrm{Re}[\epsilon(\alpha)]$.

In order to characterize the effect of the initial system-environment correlations via the trace distance, we have to monitor the evolution of two different polarization states obtained from two different initial total states having the same environmental state. Please note that with respect to the evolutions reported in ch. 8, where we intentionally modify the environmental state, here it is crucial that the environment remains the same. We compare an initially uncorrelated state $\rho^1_{SE}(\alpha)$, corresponding to Eq. (9.4) for $\varphi(\theta) = 0$, with an initially correlated state $\rho^2_{SE}(\alpha)$ for a non-trivial function $\varphi(\theta)$. In this way, the reduced system states $\rho^k_S(\alpha)$ $k = 1, 2$ are both of the form given by Eq. (9.5), with different $\epsilon_k(\alpha)$. Note that the product state $\rho^1_{SE}(0)$ differs from $\rho^2_S(0) \otimes \rho^2_E(0)$ only for an overall phase term in the integration over θ, which has no observable consequences on the dynamics of the polarization degrees of freedom. The trace distance between the two reduced states under investigation is then given by

$$\begin{aligned} D\left(\rho^1_S(\alpha), \rho^2_S(\alpha)\right) &= \frac{1}{2}\left|\epsilon_1(\alpha) - \epsilon_2(\alpha)\right| \\ &= \frac{1}{2}\left|\int d\theta |G(\theta)|^2 e^{i\alpha\theta}\left(1 - e^{i\varphi(\theta)}\right)\right| . \end{aligned} \tag{9.6}$$

Different choices for the initial phase $\varphi(\theta)$ result in different dynamical behavior of the trace distance. We have exploited this fact to analyze in detail the effect of initial system-environment correlations on the subsequent evolution of the open system.

9.4.2 Experimental results

Experimentally, we have measured the quantity $\epsilon(\alpha)$ for $\varphi(\theta) = 0$ and $\varphi(\theta) = \sin(\lambda\theta)$, exploiting its equality with the visibility, obtained in the standard way by counting the coincidences with polarizers set at $45°, 45°$ and at $45°, -45°$ (see sec. 4.1 for further details). The functions of the variable θ are discretized by the SLM, and thus become functions of the pixel number n. The resolution is given by h/D, where $h = 100\,\mu$m is the pixel width and $D = 330\,$mm is the SLM distance from the source. In our experiment the SLM introduces the functions

$$\begin{aligned} \phi^1(n) &= -a_{opt}(n - n_1) + b \\ \phi^2(n, a) &= a_{opt}(n - n_2) + a(n - n_2) + \varphi(n - n_2) , \end{aligned} \tag{9.7}$$

on the two beams respectively, where $a_{opt} = 0.1$ rad/pixel is an optimal slope used to achieve the maximal purification of the polarization entangled state, and the constant b is used to offset the residual constant term. The

integers n_1 and n_2 are the central pixel numbers on the idler and on the signal beams. The experimental evolution parameter is then $a = \alpha h/D$ and is expressed in rad/pixel.

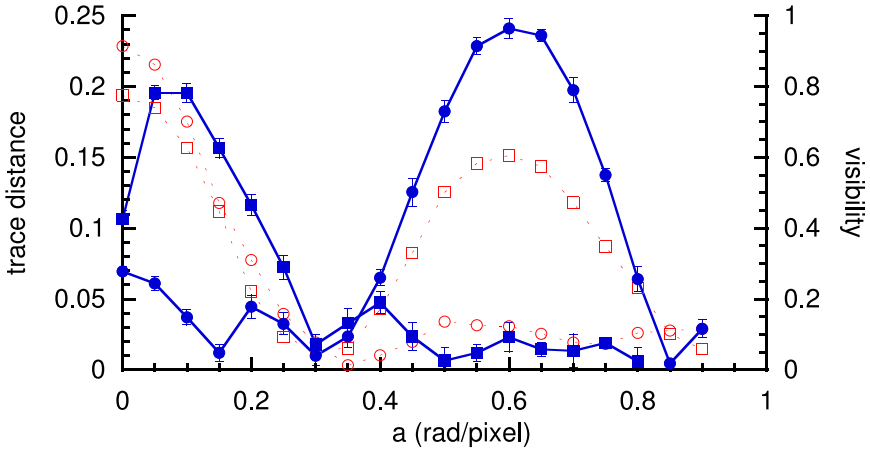

Figure 9.3: *Trace distance and visibility as a function of the experimental evolution parameter a, the two quantities are related through Eq. (9.6). Full circles describe the trace distance between* $\rho_S^1(a)$*, i.e.* $\varphi(n - n_2) = 0$*, and* $\rho_S^2(a)$ *with* $\varphi(n - n_2) = \sin(\lambda(n - n_2))$*,* $\lambda = -0.6$ *rad/pixel. Full squares describe the trace distance between* $\rho_S^1(a)$ *and* $\rho_S^2(a)$ *with* $\varphi(n - n_2) = \tau(n - n_2)$*,* $\tau = 0.1$ *rad/pixel. Lines are a guide for the eye. Empty circles refer to visibility with the choice* $\varphi(n - n_2) = 0$*, whereas empty squares refer to the case in which initial correlations are introduced through the phase function* $\varphi(n - n_2) = \sin[\lambda(n - n_2)]$*. For the visibility the uncertainties are within the symbols.*

The trace distance is the quantity which reveals the presence and the effects of initial correlations, and its behavior is reported in Fig. 9.3, together with the visibility which provides the raw data from which the trace distance can be extracted in the present case. In the figure full circles describe the trace distance, as a function of the evolution parameter a, between the reduced state $\rho_S^1(a)$ evolved from the initial total product state, i.e. $\varphi(n - n_2) = 0$, and the reduced state $\rho_S^2(a)$ related to the initial correlated state with $\varphi(n-n_2) = \sin(\lambda(n-n_2))$. The trace distance, after an initial decrease and a first small oscillation, presents a revival up to a value which is more than three times the initial one. As expected, the reduced system can access information which is initially outside it, related to its initial correlations with the environment. The trace distance reaches its maximum around $a = 0.6$ rad/pixel, towards the end of the monitored time interval. The maximum of the trace distance quantifies the total amount of information which can be accessed by means of measurements performed on the reduced system

only [138]. Note that it can be shifted to smaller values of the evolution parameter a by decreasing the absolute value of λ. Thus, by introducing a sinusoidal phase modulation via the SLM, we have obtained a behavior of the trace distance which highlights the presence of initial correlations and their effects in the subsequent evolution, also for long times [139].

The simplest choice for the phase $\varphi(n - n_2)$ in the initially correlated state $\rho^2_{SE}(\alpha)$ is a second linear phase besides that containing the evolution parameter a, i.e. $\varphi(n - n_2) = \tau(n - n_2)$. Indeed, this corresponds to shift the initially uncorrelated state $\rho^1_{SE}(\alpha)$ forward in time by τ. Then, from the visibility measurement, we can directly obtain the evolution of the trace distance between $\rho^1_S(a)$ and $\rho^2_S(a)$ with $\varphi(n - n_2) = \tau(n - n_2)$. This is represented by full squares in Fig. 9.3, for $\tau = 0.1$ rad/pixel. In this case the growth of the distinguishability between the two reduced states starts from the very beginning of the dynamics. As expected, the trace distance increases over its initial value, reaching its maximum value at $a = 0.1$ rad/pixel and decreasing afterwards. The subsequent oscillations can be traced back to the finite pixel size. Notice also that using a linear term we cannot obtain a revival of the trace distance (as in the previous case) over its initial value for high values of a. Since in this case $\rho^2_S(a) = \rho^1_S(a + \tau)$, the full squares in Fig. 9.3 also describe the evolution of the trace distance between a pair of reduced states occurring at two different points, separated by τ, of the same dynamics starting from the initial total product state given by $\rho^1_{SE}(0)$. From this point of view, the increase over the initial value of the trace distance indicates that the single evolution under investigation is not compatible with a description through a dynamical semigroup Λ_t, which could be introduced, e.g., on the basis of some phenomenological ansatz. Indeed, the semigroup property $\Lambda_{t+\tau} = \Lambda_t \Lambda_\tau$, together with the trace distance contractivity under CPT maps, would imply $D(\rho^1_S(t), \rho^2_S(t)) = D(\Lambda_t \rho^1_S(0), \Lambda_t \rho^1_S(\tau)) \leq D(\rho^1_S(0), \rho^1_S(\tau)) = D(\rho^1_S(0), \rho^2_S(0))$. However, in general one cannot discriminate in this way whether the deviations from the semigroup dynamics are due to correlations in the initial total state or to other sources of non-Markovianity [140].

9.5 State reconstruction

In order to reconstruct the trace distance evolution, we only had to perform visibility measurements to access the off-diagonal values $\epsilon_i(\alpha)$. However, in more general situations one could need a full tomographic reconstruction of the reduced states. This would be the case in the presence of non-real coefficients $\epsilon_k(\alpha)$ or when dealing with partially or fully unknown states. For this reason, we have also performed state reconstruction by polarization qubit tomography. In Fig. 9.4 (left) we show the tomographic reconstruction of the polarization state just after the purification and without any initial

correlation, i.e. for $\varphi(n-n_2)=0$ and $a=0$. The visibility is 0.914 ± 0.006 (not exactly one mostly because of the large spectrum detected). In Fig. 9.4 (right) we report the two-qubit tomography for the state characterizing the maximum revival of the visibility in the presence of initial correlations given by $\varphi(n-n_2)=\sin[\lambda(n-n_2)]$, i.e. at $a=0.6$ rad/pixel. The corresponding visibility is 0.605 ± 0.007.

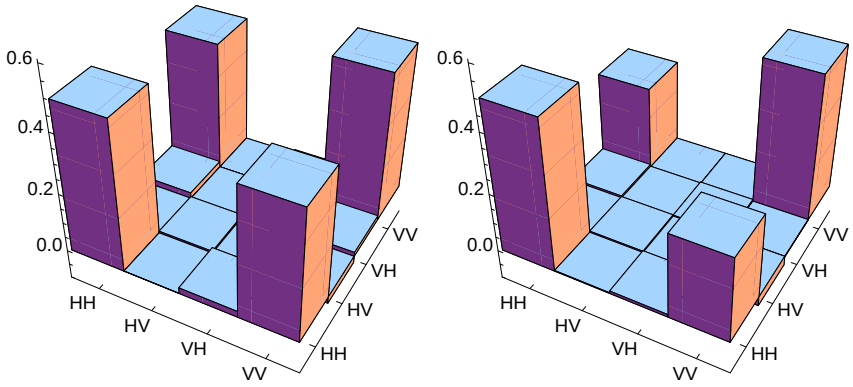

Figure 9.4: *Tomographic reconstruction of the two-qubit density matrix just after the purification (left), without any initial phase, i.e. for* $\varphi(n-n_2)=0$ *and* $a=0$. *The visibility is* 0.914 ± 0.006. *Tomographic reconstruction for* $\varphi(n-n_2)=\sin(\lambda(n-n_2))$ *at* $a=0.6$ *(right), i.e. at the maximum of the visibility revival [compare with Fig. 9.3]. The corresponding visibility is* 0.605 ± 0.007

9.6 Conclusions

We have reported an experimental observation of the effect of initial correlations between an open quantum system and its environment by means of the trace distance. In particular, we have shown the increase of the distinguishability between two reduced states, sharing the same reduced environmental state, over its initial value on both short and long time scales. Our all-optical scheme is based on the use of a spatial light modulator, which allows us to introduce initial correlations in a very general way. In particular, this setup allows to engineer different kinds of dynamical behavior of the trace distance, so that one can, e.g., tune the position and the amplitude of the revival points of the distinguishability.

After the completion of this work, we became aware of [141], where initial correlations between the polarization and the spectral degrees of freedom of single photon states are experimentally witnessed by means of the trace distance.

Conclusion and Perspectives

During my PhD I have addressed the problem of purification of the intrinsic phase term in a photonic entanglement source based on Spontaneous Parametric Down Conversion within a pair of type-I crystals. I have studied the different contribution to decoherence such as the delay time, the spectral and the angular phase difference between horizontal and vertical photon pairs. Then I have realized an optical system allowing the optimization of entanglement purity and brightness. The essential advantage of our source is the use of a very large angular and spectral distribution of the photons, allowing to obtain a bright source even with a very low laser pump power. A crucial role in this work has been played by a programmable Spatial Light Modulator. This device introduces position and polarization dependent phase shift allowing the addition of a relative angular phase function at will on the polarization entangled state. Besides the purification work we fully exploit the SLM properties studying how the polarization entanglement purity depends on the transverse profile of the pump beam. Our source can work in different regimes depending on the amount of spectrum selected; indeed when the pump beam waist is large enough, a narrow spectral selection causes a strong angular correlation between the photon in a pair. In other words signal and idler photons are entangled also in the momentum. Otherwise a very large spectral selection washed out this spatial correlation and the momentum entanglement disappear.

Once the purification has been obtained we exploit the properties of our source coupled with the SLM to realize multiqubit entanglement, ghost imaging and non-local superposition of pure phase objects also demonstrating the proof-of-principle of a new cryptographic scheme. Besides these, we study the open system dynamics of the polarization within the environment of the linear momentum degrees of freedom of the same two photons. In this framework we demonstrate two kind of dynamics for different environment spectrum, and we analyse the effect of initial correlation studying the evolution of the trace distance between two states.

In future this source could be used for the analysis of the walk off effect on the entangled states studying in deep the spatial properties of the pump. Another proposal is the realization of entanglement dynamics with correlated baths. In this framework we intend realize a study of the entan-

glement dynamics exploiting the spatial correlation between the two environments (angular distributions) in different regimes. I have also proposed the realization of the teleportation of a momentum state into a polarization one exploiting the large angular distribution and birefringent crystals. Alice generates a momentum qubit subdividing the spatial distribution in two different sections; then using a long birefringent crystal she mixes different polarization states that belong to different spatial sections. It is an operation on two qubit of the same photon. After a proper correction of the phase and the delay time, the initial momentum quantum state owned by Alice is teleported on Bob side but as a polarization qubit.

In conclusion our work contributed in the understanding of the physics behind entangled photons generation in type-I down conversion. Some application has already been realized but the power of our source is not yet exausted.

Acknowledgments

Giunto alla fine di questo percorso ritengo doverosi alcuni ringraziamenti. Al dott. Simone Cialdi, il mio supervisore, per quanto mi ha insegnato, per la pazienza e l'attenzione che ha avuto nel seguirmi in questo lavoro di tesi e non solo. Al prof. Matteo Paris per quanto mi ha insegnato e per avermi accolto facendomi sentire fin da subito parte del gruppo di ottica e informazione quantistica. A Stefano Vezzoli, Andrea Schiavi, Enrico Tesio e Andrea Tabacchini con i quali ho condiviso tante ore di laboratorio. Un ringraziamento particolare al prof. Ilario Boscolo per avermi trasmesso la passione per la fisica e la ricerca.

Ringrazio la mia famiglia senza la quale non avrei potuto fare niente. I miei genitori Ambrogio e Mirella e i miei fratelli Marta, Francesco, Annalisa e Gabriele per avermi sostenuto e accompagnato.

Mia moglie Giada, per questi tre anni di matrimonio e perché tutti i giorni mi sopporta e mi incoraggia. Sono felice di condividere la vita con te. Le mie due figlie, Rebecca e Michela, che nonostante la fatica e l'insonnia mi donano tanta gioia.

Ringrazio tutti gli amici che ho avuto vicino e che sempre mi ricordano quali sono le cose importanti.

Infine ringrazio Dio per il dono della vita e per la sua presenza forte e concreta nella mia storia. Grazie per aver condotto la mia vita fino a oggi; so che mi accompagnerai ovunque.

Bibliography

[1] A. Einstein, B. Podolsky, and N. Rosen, *Can Quantum-Mechanical Description of Physical Reality Be Considered Complete?*, Phys. Rev. **47**, 777 (1935).

[2] E. Schrödinger, M. Born, *Discussion of probability relations between separated systems*, Mathematical Proceedings of the Cambridge Philosophical Society **31**, 555 (1935).

[3] J. S. Bell, *On the Einstein Podolsky Rosen paradox*, Physics **1**, 195 (1964).

[4] S. J. Freedman and J. F. Clauser, *Experimental Test of Local Hidden-Variable Theories*, Phys. Rev. Lett **28**, 938 (1972).

[5] A. Aspect, P. Grangier and G. Roger, *Experimental Tests of Realistic Local Theories via Bell's Theorem*, Phys. Rev. Lett. **47**, 460 (1981); A. Aspect, P. Grangier and G. Roger, *Experimental Realization of Einstein-Podolsky-Rosen-Bohm Gedankenexperiment: A New Violation of Bell's Inequalities*, Phys. Rev. Lett. **49**, 91 (1982); A. Aspect, J. Dalibard and G. Roger, *Experimental Test of Bell's Inequalities Using Time-Varying Analyzers*, Phys. Rev. Lett. **49**, 1804 (1982).

[6] I. L. Chuang and M. A. Nielsen, *Quantum Information and Quantum Computation*, Cambridge University Press (Cambridge, UK, 2000).

[7] Y. H. Shih and C. O. Alley, Phys. Rev. Lett. **61**, 2921 (1988); Z. Y. Ou and L. Mandel, Phys. Rev. Lett. **61**, 50 (1988).

[8] L. Hardy, *Source of photons with correlated polarisations and correlated directions*, Phys. Lett. A **161**, 326 (1992).

[9] D. V. Strekalov, T. B. Pittman, A. V. Sergienko, Y. H. Shih, and P. G. Kwiat, *Postselection-free energy-time entanglement*, Phys. Rev. A **54**, R1 (1996).

[10] P. G. Kwiat, K. Mattle, H. Weinfurter, A. Zeilinger, A. V. Sergienko, and Y. H. Shih, *New high-intensity source of polarization-entangled photon pairs*, Phys. Rev. Lett. 75, 4337 (1995)

[11] P.G. Kwiat, E. Waks, A. G. White, I. Appelbaum, and P.G. Eberhard, *Ultrabright Source of Polarization-Entangled Photons*, Phys. Rev. A **60**, R773 (1999).

[12] N. Kiesel, C. Schmid, U. Weber, G. Toth, O. Guhne, R. Ursin, and H. Weinfurter, *Experimental analysis of a four-qubit photon cluster state* Phys. Rev. Lett. **95**, 210502 (2005).

[13] M. Barbieri, C. Cinelli, P. Mataloni, and F. De Martini, *Polarization-momentum hyperentangled states: Realization and characterization*, Phys. Rev. A **72**, 052110 (2005); G. Vallone, R. Ceccarelli, F. De Martini, and P. Mataloni, *Hyperentanglement of two photons in three degrees of freedom* Phys. Rev. A **79** 030301(R) (2009).

[14] A. Mair, A. Vaziri, G. Weihs and A. Zeilinger *Entanglement of the orbital angular momentum states of photons*, Nature **412**, 313 (2001).

[15] G. Brida, M. Chekhova, M. Genovese and L. Krivitsky, *Generation of different Bell states within the spontaneous parametric down-conversion phase-matching bandwidth*, Phys. Rev. A **76**, 053807 (2007).

[16] A. Gatti, E. Brambilla, L. Caspani, O. Jedrkiewicz, and L. A. Lugiato, *X entanglement: the nonfactorable spatiotemporal structure of biphoton correlation*, Phys. Rev. Lett. **102**, 223601 (2009).

[17] R. Rangarajan, A. B. U'Ren, and P. G. Kwiat, *Polarization dependence on downconversion emission angle: investigation of the "Migdall effect"*, J. Mod. Opt. **58**, 312 (2010).

[18] H. Wunderlich, G. Vallone, P. Mataloni and M. B. Plenio *Optimal verification of entanglement in a photonic cluster state experiment* New Journal of Physics **13**, 033033 (2011).

[19] J. T. Barreiro, Tzu-Chieh Wei and P. G. Kwiat *Beating the channel capacity limit for linear photonic superdense coding*, Nature Physics **4**, 282 (2008).

[20] D. Bouwmeester, Jian-Wei Pan, K. Mattle, M. Eibl, H. Weinfurter and A. Zeilinger, *Experimental quantum teleportation*, Nature **390**, 575 (1997); S. Giacomini, F. Sciarrino, E. Lombardi, and F. De Martini, *Active teleportation of a quantum bit* Phys. Rev. A, **66**, 030302(R) (2002); H. W. Lee and J. Kim, Phys. Rev. A **63**, 012305 (2000); E. Knill, R. Laflamme, and G. Milburn, Nature (London) **409**, 46 (2001); F. Sciarrino, E. Lombardi, S. Giacomini, and F. De Martini, *Active Teleportation and Entanglement swapping of a Vacuum-One Photon Qubit*, Fortschritte der Physik **51**, 331 (2003).

[21] L. Marrucci, E. Karimi, S. Slussarenko, B. Piccirillo, E. Santamato, E. Nagali, and F. Sciarrino, *Spin-to-orbital conversion of the angular momentum of light and its classical and quantum applications*, J. Opt. **13**, 064001 (2011); E. Nagali, F. Sciarrino, F. De Martini, L. Marrucci, B. Piccirillo, E. Karimi, and E. Santamato, *Quantum information transfer from spin to orbital angular momentum of photons*, Phys. Rev. Lett. **103**, 013601 (2009).

[22] M. P. Almeida, F.Melo, M. Hor-Meyll, A. Salles, S. P.Walborn, P. H. Souto Ribeiro, and L. Davidovich, *Environment-induced sudden death of entanglement*, Science **316**, 579 (2007).

[23] J.-S. Xu, C.-F. Li, M. Gong, X.-B. Zou, C.-H. Shi, G. Chen, and G.-C. Guo, *Experimental demonstration of photonic entanglement collapse and revival*, Phys. Rev. Lett. **104**, 100502 (2010).

[24] B.-H. Liu, L. Li, Y.-F. Huang, C.-F. Li, G.-C. Guo, E.-M.Laine, H.-P. Breuer and J. Piilo, *Experimental control of the transition from Markovian to non-Markovian dynamics of open quantum systems*, Nature Physics, advance online publication, DOI:10.1038/NPHYS2085.

[25] R. Rangarajan, M. Goggin, and P. Kwiat, *Optimizing type-I polarization-entangled photons*, Opt. Expr. **17**, 18920 (2009).

[26] S. Cialdi, Davide Brivio and M. G. A. Paris, *Programmable purification of type-I polarization-entanglement*, Appl. Phys. Lett. **97**, 041108 (2010).

[27] S. Cialdi, Davide Brivio and M. G. A. Paris, *Demonstration of a programmable source of two-photon multiqubit entangled states*, Phys. Rev. A **81**, 042322 (2010).

[28] S. Cialdi, Davide Brivio, E. Tesio and M. G. A. Paris *Nonlocal compensation of pure phase objects with entangled photons*, Phys. Rev. A **84**, 043817 (2011).

[29] S. Cialdi, Davide Brivio, E. Tesio and M. G. A. Paris, *Programmable entanglement oscillations in a non-Markovian channel*, Phys. Rev. A **83**, 042308 (2011).

[30] A. Smirne, Davide Brivio, S. Cialdi, B. Vacchini and M. G. A. Paris *Experimental investigation of initial system-environment correlations via trace-distance evolution*, Phys. Rev. A **84**, 032112 (2011).

[31] W. K. Wootters, *Entanglement of Formation of an Arbitrary State of Two Qubits*, Phys. Rev. Lett. 80, 2245 (1998).

[32] K. Banaszek, G. M. D'Ariano, M. G. A. Paris and M. F. Sacchi, *Maximum-likelihood estimation of the density matrix*, Phys. Rev. A **61**, 010304(R) (1999).

[33] D. F. V. James, P. G. Kwiat,W. J.Munro and A. G.White, *Measurement of qubits*, Phys. Rev. A **64**, 052312 (2001).

[34] J.F. Clauser, M.A. Horne, A. Shimony, and R.A. Holt, *Proposed Experiment to Test Local Hidden-Variable Theories* Phys. Rev. Lett. **23**, 880 (1969).

[35] A. Yariv and P. Yeh, *Optical Waves in crystals*, Wiley Classics Library (2003).

[36] J. B. Altepeter, E. R. Jeffrey and P. G. Kwiat, *Phase-compensated ultra-bright source of entangled photons*, Opt. Expr. **13**, 8951 (2005).

[37] A. Migdall, *Polarization directions of noncollinear phase-matched optical parametric downconversion output*, J. Opt. Soc. Am. B **14**, 1093 (1997).

[38] E. C. Cheung, K. Koch, G. T. Moore and J. M. Liu, *Measurements of second-order nonlinear optical coefficients from the spectral brightness of parametric fluorescence*, Opt. Lett. **19**, 168 (1994).

[39] G. Brida, M. Genovese and C. Novero, *On the measurement of photon flux in parametric down-conversion*, Eur. Phys. J. D **8**, 273 (2000).

[40] F. A. Bovino, P. Varisco, A. M. Colla, G. Castagnoli, G. Di Giuseppe and A. V. Sergienko, *Effective fiber-coupling of entangled photons for quantum communication*, Opt. Comm. **227**, 343 (2003).

[41] C. Kurtsiefer, M. Oberparleiter and H. Weinfurter, *High-efficiency entangled photon pair collection in type-II parametric fluorescence*, Phys. Rev. A **64**, 023802 (2001).

[42] C. Monken, P. Souto Ribeiro, and S. Padua, *Optimizing the photon pair collection efficiency: a step toward a loophole-free Bell's inequalities experiment*, Phys. Rev. A **57**, R2267 (1998); **57**, 3123 (1998).

[43] Y. Nambu, K. Usami, Y. Tsuda, K. Matsumoto, K. Nakamura, *Generation of polarization-entangled photon pairs in a cascade of two type-I crystals pumped by femtosecond pulse*, Phys. Rev. A **66**, 033816 (2002).

[44] C. Cinelli, G. Di Nepi, F. De Martini, M. Barbieri and P. Mataloni, *Parametric source of two-photon states with a tunable degree of entanglement and mixing: Experimental preparation of Werner states and maximally entangled mixed states*, Phys. Rev. A **70**, 022321 (2004).

[45] M. Barbieri, C. Cinelli, F. De Martini, and P. Mataloni, *Generation of polarization-entangled photon pairs by a single crystal interferometric source pumped by femtosecond laser pulses*, Las. Phys. **16**, 1439 (2006).

[46] Y.-H Kim, S. P. Kulik, Y. Shih, Phys. Rev. A **62**, 011802 (2000).

[47] S. Cialdi, F. Castelli, I. Boscolo, M. G. A. Paris, *Generation of entangled photon pairs using pump with small coherence time.*, Appl. Opt. **47**, 1832 (2008).

[48] S. Cialdi, F. Castelli, M. G. A. Paris, *Properties of entangled photon pairs generated by a CW laser with small coherence time: theory and experiment*, J. Mod. Opt. **56**, 215 (2009).

[49] R. Raussendorf and H. J. Briegel, *A One-Way Quantum Computer*, Phys. Rev. Lett. **86**, 5188 (2001).

[50] M. A. Nielsen, *Cluster-state quantum computation*,Rep. Math. Phys. **57**, 147 (2006).

[51] G. Vallone, E. Pomarico, F. De Martini and P. Mataloni, *Active One-Way Quantum Computation with Two-Photon Four-Qubit Cluster States*, Phys. Rev. Lett. **100**, 160502 (2008).

[52] R. Cleve, D. Gottesman and H. K. Lo, *How to Share a Quantum Secret*, Phys. Rev. Lett. **83**, 648 (1999).

[53] D. Schlingemann and R. F. Werner, *Quantum error-correcting codes associated with graphs*, Phys. Rev. A **65**, 012308 (2001).

[54] N. D. Mermin, *Extreme quantum entanglement in a superposition of macroscopically distinct states*, Phys. Rev. Lett. **65**, 1838 (1990).

[55] O. Gühne, G. Toth, P. Hyllus and H. J. Briegel, *Bell Inequalities for Graph States*, Phys. Rev. Lett. **95**, 120405 (2005); A. Cabello and P. Moreno, *Bipartite All-Versus-Nothing Proofs of Bell's Theorem with Single-Qubit Measurements*, Phys. Rev. Lett. **99**, 220402 (2007); A. Cabello, O. Guhne and D. Rodriguez, *Mermin inequalities for perfect correlations*,Phys. Rev. A **77**, 062106 (2008).

[56] P. Walther, M. Aspelmeyer, K. J. Resch and A. Zeilinger, *Experimental Violation of a Cluster State Bell Inequality*, Phys. Rev. Lett. **95**, 020403 (2005).

[57] M. Barbieri, F. De Martini, P. Mataloni, G. Vallone and A. Cabello, *Enhancing the Violation of the Einstein-Podolsky-Rosen Local Realism by Quantum Hyperentanglement*, Phys. Rev. Lett. **97**, 140407 (2006); R. Ceccarelli, G. Vallone, F. De Martini, P. Mataloni and A. Cabello,

Experimental Entanglement and Nonlocality of a Two-Photon Six-Qubit Cluster State,Phys. Rev. Lett. **103**, 160401 (2009).

[58] Z. Zhao, T. Yang, Y. A. Chen, A. N. Zhang, M. Zukowski and J. W. Pan, *Experimental Violation of Local Realism by Four-Photon Greenberger-Horne-Zeilinger Entanglement*, Phys. Rev. Lett. **91**, 180401 (2003).

[59] P. Walther, K. J. Resch, T. Rudolph, E. Schenck, H. Weinfurter, V. Vedral, M. Aspelmeyer and A. Zeilinger, *Experimental one-way quantum computing*, Nature **434**, 169 (2005).

[60] N. Kiesel, C. Schmid, U. Weber, G. Toth, O. Guhne, R. Ursin and H. Weinfurter, *Experimental Analysis of a Four-Qubit Photon Cluster State*, Phys. Rev. Lett.**95**, 210502 (2005).

[61] R. Prevedel, P.Walther, F. Tiefenbacher, P. B¨ohi, R. Kaltenbaek, T. Jennewein and A. Zeilinger, *High-speed linear optics quantum computing using active feed-forward*, Nature **445**, 65 (2007).

[62] K. Chen, C. M. Li, Q. Zhang, Y. A. Chen, A. Goebel, S. Chen, A. Mair and J. W. Pan, *Experimental Realization of One-Way Quantum Computing with Two-Photon Four-Qubit Cluster States*, Phys. Rev. Lett. **99**, 120503 (2007).

[63] G. Vallone, E. Pomarico, P. Mataloni, F. DeMartini and V. Berardi, *Realization and Characterization of a Two-Photon Four-Qubit Linear Cluster State*, Phys. Rev. Lett. **98**, 180502 (2007).

[64] L. Neves, G. Lima, A. Delgado and C. Saavedra, *Hybrid photonic entanglement: Realization, characterization, and applications*, Phys. Rev. A **80**, 042322 (2009).

[65] Y. Tokunaga, S. Kuwashiro, T. Yamamoto, M. Koashi and N. Imoto, *Generation of High-Fidelity Four-Photon Cluster State and Quantum-Domain Demonstration of One-Way Quantum Computing*, Phys. Rev. Lett. **100**, 210501 (2008).

[66] A. Mair, A. Vaziri, G.Weihs and A. Zeilinger, *Entanglement of the orbital angular momentum states of photons*, Nature **412**, 313 (2001).

[67] C. Cinelli, M. Barbieri, R. Perris, P. Mataloni and F. De Martini, *All-Versus-Nothing Nonlocality Test of Quantum Mechanics by Two-Photon Hyperentanglement*, Phys. Rev. Lett.**95**, 240405 (2005).

[68] M. Barbieri, C. Cinelli, P. Mataloni, and F. De Martini, *Polarization-momentum hyperentangled states: Realization and characterization*, Phys. Rev. A **72**, 052110 (2005).

[69] J. T. Barreiro, N. K. Langford, N. A. Peters and P. G. Kwiat, *Generation of Hyperentangled Photon Pairs*, Phys. Rev. Lett. **95** 260501 (2005).

[70] C. Schuck, G. Huber, C. Kurtsiefer and H. Weinfurter, *Complete Deterministic Linear Optics Bell State Analysis*, Phys. Rev. Lett. **96**, 190501 (2006).

[71] H. S. Park, J. Cho, J. Y. Lee, D. Lee and S. Choi, *Two-photon four-qubit cluster state generation based on a polarization-entangled photon pair*, Opt. Expr. **15**, 17960 (2007).

[72] B. P. Lanyon, M. Barbieri, M. P. Almeida, T. Jennewein, T. C. Ralph, K. J. Resch, G. J. Pryde, J. L. O'Brien, A. Gilchrist and A. G. White, *Simplifying quantum logic using higher-dimensional Hilbert spaces*, Nature Phys. **5**, 134 (2009).

[73] G. Vallone, R. Ceccarelli, F. De Martini and P. Mataloni, *Hyperentanglement of two photons in three degrees of freedom*, Phys. Rev. A **79** 030301(R) (2009).

[74] R. Ceccarelli, G. Vallone, F. De Martini, P. Mataloni and A. Cabello, *Experimental Entanglement and Nonlocality of a Two-Photon Six-Qubit Cluster State*, Phys. Rev. Lett. **103**, 160401 (2009).

[75] B. Dayan, Y. Bromberg, I. Afek and Y. Silberberg, , Phys. Rev. A 75, 043804 (2007)

[76] G. Lima, A. Vargas, L. Neves, R. Guzm´an, and C. Saavedra, *Spectral polarization and spectral phase control of time-energy entangled photons*, Opt. Expr. **17**, 10688 (2009).

[77] E. Yao, S. Franke-Arnold, J. Courtial, M. J. Padgett and S. M. Barnett, *Observation of quantum entanglement using spatial light modulators*, Opt. Expr. **14**, 13089 (2006).

[78] M. Franca Santos, P. Milman, A. Z. Khoury and P. H. SoutoRibeiro, *Measurement of the degree of polarization entanglement through position interference*, Phys. Rev A **64**, 023804 (2001).

[79] D. P. Caetano, P. H. Souto Ribeiro, J. T. C. Pardal and A. Z. Khoury, *Quantum image control through polarization entanglement in parametric down-conversion*, Phys. Rev A **68**, 023805 (2003).

[80] M. N. O'Sullivan-Hale, I. A. Khan, R. W. Boyd and J. C. Howell, *Pixel Entanglement: Experimental Realization of Optically Entangled* $d = 3$ *and* $d = 6$ *Qudits*, Phys. Rev. Lett. **94**, 220501 (2005).

[81] G. Brida, I. P. Degiovanni, A. Florio, M. Genovese, P. Giorda, A. Meda, M. G. A. Paris and A. Shurupov, *Experimental Estimation of Entanglement at the Quantum Limit*, Phys. Rev. Lett. **104**, 100501 (2010).

[82] A. Gatti, E. Brambilla, and L. A. Lugiato, *Chapter 5 Quantum imaging*, Progr. Opt. **51**, 251 (2008).

[83] R. S. Bennink, S. J. Bentley, and R. W. Boyd, *"Two-Photon" Coincidence Imaging with a Classical Source*, Phys. Rev. Lett. **89**, 113601 (2002).

[84] F. Ferri, D. Magatti, A. Gatti, M. Bache, E. Brambilla, and L.A. Lugiato, *High-Resolution Ghost Image and Ghost Diffraction Experiments with Thermal Light*, Phys. Rev. Lett. **94**, 183602 (2005).

[85] O. Katz, Y. Bromberg, and Y. Silberberg, *Compressive ghost imaging*, Appl. Phys. Lett. **95**, 131110 (2009).

[86] P. H. S. Ribeiro, S. Padua, J. C. Machado da Silva, and G. A. Barbosa, *Controlling the degree of visibility of Young's fringes with photon coincidence measurements*, Phys. Rev. A **49**, 4176 (1994).

[87] T. B. Pittmann, Y. H. Shih, D. V. Strekalov, and S. V. Sergienko, *Optical imaging by means of two-photon quantum entanglement*, Phys. Rev. A **52**, R3429 (1995); D. V. Strekalov, A. V. Sergienko, D. N. Klyshko, and Y. H. Shih, *Observation of Two-Photon "Ghost" Interference and Diffraction*, Phys. Rev. Lett. **74**, 3600 (1995).

[88] A. F. Abouraddy, B. E. A. Saleh, A. V. Sergienko, and M. C. Teich, *Role of Entanglement in Two-Photon Imaging*, Phys. Rev. Lett. **87**, 123602 (2001).

[89] B. Jack, J. Leach, J. Romero, S. Franke-Arnold, M. Ritsch-Marte, S. M. Barnett and M. J. Padgett, *Holographic Ghost Imaging and the Violation of a Bell Inequality*, Phys. Rev. Lett. **103**, 083602 (2009).

[90] Y. T. Zhang, C. J. He, H. G. Li, K. G. Wang, *Novel Ghost Imaging Method for a Pure Phase Object*, Chin. Phys. Lett. **25**, 2481 (2008).

[91] S. Gan, S.H. Zhang, T. Zhao, J. Xiong, X. D. Zhang, K. G. Wang, *Cloaking of a phase object in ghost imaging*, Appl. Phys. Lett. **98**, 111102 (2011)

[92] A. Gatti, E. Brambilla, and L. A. Lugiato, *Entangled Imaging and Wave-Particle Duality: From the Microscopic to the Macroscopic Realm*, Phys. Rev. Lett. **90**, 133603 (2003); A. Gatti, E. Brambilla, M. Bache and L. A. Lugiato, *Correlated imaging, quantum and classical*, Phys. Rev. A **70**, 013802 (2004).

[93] A. F. Abouraddy, P. R. Stone, A. V. Sergienko, B. E. A. Saleh and M. C. Teich, *Entangled-Photon Imaging of a Pure Phase Object*, Phys. Rev. Lett. **93**, 213903 (2004)

[94] A. M. Steinberg, P. G. Kwiat, and R. Y. Chiao, *Dispersion cancellation in a measurement of the single-photon propagation velocity in glass*, Phys. Rev. Lett. **68**, 2421 (1992).

[95] C. Bonato, A. V. Sergienko, B. E. A. Saleh, S. Bonora, P. Villoresi, *Even-Order Aberration Cancellation in Quantum Interferometry*, Phys. Rev. Lett. **101**, 233603 (2008).

[96] O. Minaeva, C. Bonato, B. E. A. Saleh, D. S. Simon, A. V. Sergienko, *Odd- and Even-Order Dispersion Cancellation in Quantum Interferometry*, Phys. Rev. Lett. **102**, 100504 (2009).

[97] T. Wasak, P. Szakowski, W. Wasilewski, K. Banaszek *Entanglement-based signature of nonlocal dispersion cancellation*, Phys. Rev. A **82**, 052120 (2010)

[98] J. D. Franson, *Nonlocal cancellation of dispersion*, Phys. Rev. A **45**, 31263132 (1992).

[99] S-Y. Baek, Y-W. Cho, Y-H. Kim, *Nonlocal dispersion cancellation using entangled photons*, Opt. Expr. **17**, 19241 (2009).

[100] M. Genovese, *Research on hidden variable theories: A review of recent progresses*, Phys. Rep. **413**, 319 (2005).

[101] Y. Bromberg, O. Katz, and Y. Silberberg, *Ghost imaging with a single detector*, Phys. Rev. A **79**, 053840 (2009).

[102] J. H. Shapiro, *Computational ghost imaging*, Phys. Rev. A **78**, 061802 (2008).

[103] P. Clemente, V. Duràn, V. Torres-Company, E. Tajahuerce, and J.Lancis, *Optical encryption based on computational ghost imaging*, Opt. Lett. **35**, 2391 (2010).

[104] Y.-H Kim, S. P. Kulik, Y. Shih, *High-intensity pulsed source of space-time and polarization double-entangled photon pairs*, Phys. Rev. A **62**, 011802 (2000).

[105] W. H. Zurek, *Decoherence, einselection, and the quantum origins of the classical*, Rev. Mod. Phys. **75**, 715 (2003).

[106] M. Schlosshauer, *Decoherence, the measurement problem, and interpretations of quantum mechanics*, Rev. Mod. Phys. **76**, 1267 (2005).

[107] K. Zyczkowski, P. Horodecki, M. Horodecki, R. Horodecki, *Dynamics of quantum entanglement*, Phys. Rev A **65**, 012101 (2001).

[108] T. Yu, J. H. Eberly, *Finite-Time Disentanglement Via Spontaneous Emission*, Phys. Rev. Lett. **93**, 140404 (2004); *Sudden Death of Entanglement*, Science **323**, 598 (2009).

[109] M. P. Almeida, F. Melo, M. Hor-Meyll, A. Salles, S. P. Walborn, P. H. Souto Ribeiro, and L. Davidovich, *Environment-Induced Sudden Death of Entanglement*, Science **316**, 579 (2007).

[110] J. Laurat, K. S. Choi, H. Deng, C. W. Chou, and H. J. Kimble, *Heralded Entanglement between Atomic Ensembles: Preparation, Decoherence, and Scaling*, Phys. Rev. Lett. **99**, 180504 (2007).

[111] J-S. Xu, X-Y. Xu, C-F. Li, C-J. Zhang, X-B. Zou, and G. Guo, *Experimental investigation of classical and quantum correlations under decoherence*, Nature Commun. **1**, 7 (2010).

[112] H-P. Breuer, E-M. Laine, J. Piilo, *Measure for the Degree of Non-Markovian Behavior of Quantum Processes in Open Systems*, Phys. Rev. Lett. **103**, 210401 (2009).

[113] A. Rivas, S. F. Huelga, M. B. Plenio, *Entanglement and Non-Markovianity of Quantum Evolutions*, Phys. Rev. Lett. **105**, 050403 (2010).

[114] M. Yonac, J. H. Eberly, *Qubit entanglement driven by remote optical fields*, Opt. Lett. **33**, 270 (2008).

[115] S. Maniscalco, F. Francica, R. L. Zaffino, N. Lo Gullo, and F. Plastina, *Protecting Entanglement via the Quantum Zeno Effect*, Phys. Rev. Lett. **100**, 090503 (2008).

[116] L. Mazzola, S. Maniscalco, J. Piilo, K.-A. Suominen, and B. M. Garraway, *Sudden death and sudden birth of entanglement in common structured reservoirs*, Phys. Rev. A **79**, 042302 (2009).

[117] B. Bellomo, R. Lo Franco, S. Maniscalco, and G. Compagno, *Entanglement trapping in structured environments*, Phys. Rev. A **78**, 060302(R) (2008).

[118] K. Härkönen, F. Plastina, and S. Maniscalco, *Dicke model and environment-induced entanglement in ion-cavity QED*, Phys. Rev. A **80**, 033841 (2009).

[119] B. Bellomo, R. Lo Franco, and G. Compagno, *Non-Markovian Effects on the Dynamics of Entanglement*, Phys. Rev. Lett. **99**, 160502 (2007); Adv. Sc. Lett. **2**, 459 (2009).

[120] Q-J. Tong, J-H. An, H-G. Luo, and C. H. Oh, *Mechanism of entanglement preservation*, Phys. Rev. A **81**, 052330 (2010).

[121] F. F. Fanchini, T. Werlang, C. A. Brasil, L. G. E. Arruda, A. O. Caldeira, *Non-Markovian dynamics of quantum discord*, Phys. Rev. A. **81**, 052107 (2010).

[122] S. Maniscalco, S. Olivares, M. G. A. Paris, *Entanglement oscillations in non-Markovian quantum channels*, Phys. Rev. A **75**, 062119 (2007).

[123] R. Vasile, S. Olivares, M. G. A. Paris, S. Maniscalco, *Continuous-variable-entanglement dynamics in structured reservoirs*, Phys. Rev. A **80**, 062324 (2009).

[124] R. Vasile, P. Giorda, S. Olivares, M. G. A. Paris, S. Maniscalco, *Non-classical correlations in non-Markovian continuous-variable systems*, Phys. Rev. A **82**, 012313 (2010).

[125] J.-S. Xu, C-F. Li, M. Gong, X-B. Zou, C-H. Shi, G. Chen, and G-C. Guo, *Experimental Demonstration of Photonic Entanglement Collapse and Revival*, Phys. Rev. Lett. **104**, 100502 (2010).

[126] Z-Q. Zhou, C-F Li, G. Chen, J-S. Tang, Y. Zou, M. Gong, G-C. Guo, *Phase compensation enhancement of photon pair entanglement generated from biexciton decay in quantum dots*, Phys. Rev. A. **81**, 064302 (2010).

[127] H.-P. Breuer and F. Petruccione, *The Theory of Open Quantum Systems* (Oxford University Press, Oxford, 2007).

[128] P. Pechukas, *Reduced Dynamics Need Not Be Completely Positive*, Phys. Rev. Lett. **73**, 1060 (1994); R. Alicki, *Comment on "Reduced Dynamics Need Not Be Completely Positive"*, *ibid.* **75**, 3020 (1995); P. Pechukas, *Pechukas Replies:*, *ibid.* **75**, 3021 (1995).

[129] A. Royer, *Reduced Dynamics with Initial Correlations, and Time-Dependent Environment and Hamiltonians*, Phys. Rev. Lett. **77**, 3272 (1996).

[130] P. Štelmachovič and V. Bužek, *Dynamics of open quantum systems initially entangled with environment: Beyond the Kraus representation*, Phys. Rev. A **64**, 062106 (2001).

[131] T. F. Jordan, A. Shaji and E. C. G. Sudarshan, *Dynamics of initially entangled open quantum systems*, Phys. Rev. A **70**, 052110 (2004).

[132] P. Aniello, A. Kossakowski, G. Marmo, F. Ventriglia, and P. Vitale, *On Reduced Time Evolution for Initially Correlated Pure States*, Open Syst. Inf. Dyn. **17**, 21 (2010).

[133] A. G. Dijkstra and Y. Tanimura, *Non-Markovian Entanglement Dynamics in the Presence of System-Bath Coherence*, Phys. Rev. Lett. **104**, 250401 (2010).

[134] C. A. Rodriguez-Rosario, K. Modi, A. Kuah, A. Shaji, and E. C. G. Sudarshan, *Completely positive maps and classical correlations*, J. Phys. A **41**, 205301 (2008); A. Shabani and D. A. Lidar, *Vanishing Quantum Discord is Necessary and Sufficient for Completely Positive Maps*, Phys. Rev. Lett. **102**, 100402 (2009).

[135] E. M. Laine, J. Piilo, and H.-P. Breuer, *Witness for initial system-environment correlations in open-system dynamics*, EPL **92** 60010 (2010).

[136] C. A. Fuchs and J. van de Graaf, *Cryptographic distinguishability measures for quantum-mechanical states*, IEEE Trans. Inf. Th. **45**, 1216 (1999).

[137] E.-M. Laine, J. Piilo and H.-P. Breuer, *Measure for the non-Markovianity of quantum processes*, Phys. Rev. A **81**, 062115 (2010).

[138] A. Smirne, H.-P. Breuer, J. Piilo, and B. Vacchini, *Initial correlations in open-systems dynamics: The Jaynes-Cummings model*, Phys. Rev. A **82**, 062114 (2010).

[139] J. Dajka and J. Luczka, *Distance growth of quantum states due to initial system-environment correlations*, Phys. Rev. A **82**, 012341 (2010).

[140] A. R. Usha Devi, A. K. Rajagopal, and Sudha, *Open-system quantum dynamics with correlated initial states, not completely positive maps, and non-Markovianity*, Phys. Rev. A **83**, 022109 (2011).

[141] C.-F. Li, J.-S. Tang, Y.-L. Li, and G.-C. Guo, *Experimentally witnessing the initial correlation between an open quantum system and its environment*, Phys. Rev. A **83**, 064102 (2011).

List of Figures

List of Tables